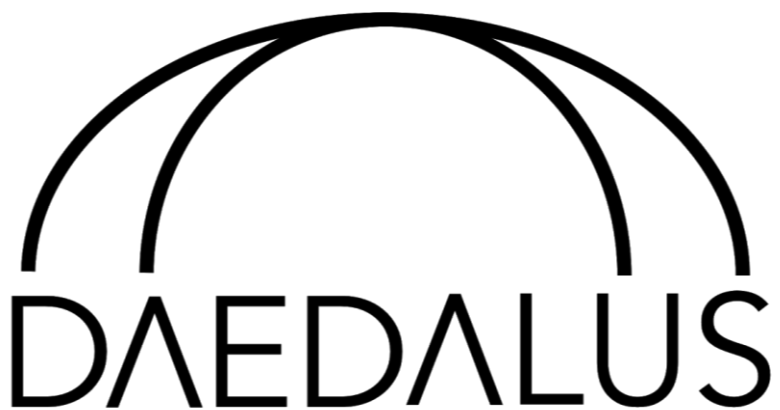


University of Pennsylvania
School of Engineering and Applied Sciences
Mechanical Engineering and Applied Mechanics Department



Final Project Report

MEAM 445/446 - MEAM Senior Design

September 2017 - April 2018

TEAM 10 - TEAM AERO

Due: May 6, 2018

PERSONEL

Team Breakdown

Full Name	Project Focus	Secondary Focus	Email Address
Rome George Arnold IV	Mechanical Manufacturing	Test Engineering	arnoldr@seas.upenn.edu
Eugenia Bejar	Project Management	Research and Development	bejare@seas.upenn.edu
Pele Collins	Mechanical Design	Computational Analysis	pelec@seas.upenn.edu
Max Herman Newberger	Test Engineering	Mechanical Manufacturing	newmax@seas.upenn.edu
Michael James Pearson	Research and Development	Project Management	mpea@seas.upenn.edu
Rosalind Fish Blais Shinkle	Computational Analysis	Mechanical Design	rshinkle@seas.upenn.edu

Faculty Advisor

Dr. Kevin T. Turner

Professor and MEAM Associate Chair for Graduate Affairs and Graduate Group Chair
Mechanical Engineering and Applied Mechanics, University of Pennsylvania
kturner@seas.upenn.edu

Technical Advisors and Sponsors

Name	Company	Position	Email	Phone
Tyler Schlenker	SpaceX	Parachute System Manager	tyler.schlenker@spacex.com	(925) 323-8578
Ricardo 'Koki' Machin	NASA	Chief Engineer, Orion CPAS	ricardo.a.machin@nasa.gov	(832) 221-1319
James 'Jim' McMichael	NASA	CCPAT Project Manager	james.h.mcmichael@nasa.gov	(832) 671-7564
Dr. Kevin T. Turner	UPenn	Professor	kturner@seas.upenn.edu	(215) 573-7485
Kyle Starr	Airborne Systems	Project Engineer I	kyle.starr@airborne-sys.com	(657) 859-3158
Robert 'Rob' Sinclair	Airborne Systems	Chief Engineer	robert.sinclair@airborne-sys.com	—
Dr. Jean Potvin	Saint Louis University	Physics Professor	jean.potvin@slu.edu	(314) 977-8424
Dr. Michael Barnhardt	NASA	Principal Investigator	michael.d.barnhardt@nasa.gov	—

ABSTRACT

Aerospace and military companies, who use parachutes for vehicle recovery, require parachute reefing - the incremental opening of a parachute canopy to limit the parachute opening forces to a predetermined value - to limit impulse the parachute and vehicle. The current method of disreefing uses reefing line cutters that employ a pyro-time train and cutter knife to sever the reefing line, allowing the parachute to open and enter the next reefing stage. Project Daedalus presents a major innovation to the parachute industry with our continuous disreefing mechanism that allows for the parachute to open gradually, rather than in discrete stages, thereby reducing the load on the parachute and capsule components while achieving full inflation in less time. Though several attempts have been made to develop such a mechanism in the past, none are practical, robust, or reliable enough for space-flight application.

After extensive analysis of the forces on NASA's Orion Capsule parachute system and numerous design iterations, Team Aero has developed a mechanism that combines a passive friction brake with a servo driven active braking system that together control the release of reefing line contained on the internal spool. Project Daedalus was tested in a rig on the MTS to simulate the forces of the reefing line in the intended configuration, which has confirmed that the mechanism achieves its goal of reducing the loads on the capsule, has the ability of handing off nominal cases, and reduces the time required for the capsule to reach steady state. Scale drop tests further demonstrated the line control of our active braking system, ensuring the desired reefing diameter over time could be achieved.

TABLE OF CONTENTS

PERSONEL	0
Team Breakdown	1
Faculty Advisor	2
Technical Advisors and Sponsors	2
ABSTRACT	3
TABLE OF CONTENTS	4
EXECUTIVE SUMMARY	9
Problem Statement	9
System Features	9
Continuously Disreefed Parachute Analysis	10
System Validation	10
System Results	11
TEAM ROLES & CONTRIBUTIONS	12
Rome George Arnold IV	12
Eugenia Bejar	12
Pele Collins	13
Max Herman Newberger	13
Michael James Pearson	13
Rosalind Fish Blais Shinkle	13
1. NEED AND BACKGROUND	14
Idea Origin and Proof of Need	14
Parachute Types	14
Parachute Reefing	17
Reefing Methods	17
Staged Skirt Reefing	18
Vent Reefing	18
Slider Reefing	19
Innovative Reefing Practices	19

Parachute Opening Load Control	21
2. OBJECTIVES	22
System Characteristics	22
Basic Characteristics	22
Reach Characteristics	22
Design Impact of Engineering Standards	23
NASA Standards	23
Safety and Life Factors	23
Mechanism Design	24
Software and Electrical Engineering	24
Mathematical Modeling of Physical Systems	24
Non-NASA Standards	25
Designing to Meet Standards	25
3. DESIGN AND REALIZATION	26
Summary	26
Physical Analysis of Continuously Disreefed Parachute Systems	27
Down Selection Process	33
Parachute Designs	33
Parachute Corset	33
Rip Stitch Parachute Expansion	34
High-Altitude Deployment System	35
Mechanical Designs	36
Eddy Brake	36
Electrorheological Fluid	37
Self-Braking Mechanism	38
Active and Passive System	39
Active Brake	40
Final System Design	42
System Analysis	42

Passive Braking Subsystem	45
Passive Brake - Capstans	45
Passive Brake - Bearings	47
Electronic Active Brake	47
Spool (System Inertia)	48
Enclosure	50
Summary	50
Design	50
Active	50
Passive (Capstans and Top Plate)	53
Top Plate	54
Capstans	55
Spool	56
Enclosure	58
Electronics and Control System	60
Electronics	60
Titanium Gear Servo	61
Optical Encoder	61
Encoder Wheel	62
Arduino Microcontroller	62
Control Systems	62
Update State Function	62
Print State Function	63
Encoder Servo Connect Function	63
Enclosure	63
Manufacturing	64
Manufacturing Summary	64
Manufacturing Subsystem Highlights	66
Active	66

Passive	68
Spool	69
Enclosure	69
4. VALIDATION AND TESTING	71
Summary	71
Pseudo-Static Testing	71
Determining Coefficient of Friction and Capstan Reduction	71
Servo Characterization Process	73
Integrated System Validation	75
Active Control Verification	75
Dynamic Simulation	77
Simulation Overview	77
Parachute Inverse Dynamics	78
Daedalus Dynamics Simulink	81
Forward Parachute Dynamics	82
Conclusion and Simulation vs Daedalus Difference	83
5. DISCUSSION	86
Summary of Achievements	86
Steps for Future Improvement	86
Component Improvements	86
Temperature Envelope	86
Passive System	87
System Volume	87
Drop Testing	88
6. BUDGET AND RESOURCES	89
REFERENCES	93
APPENDIX	94
Engineering Drawings	94
Subassembly Drawings	94

Part Machine Drawings	98
Active Brake Subassembly	98
Passive Subassembly	100
Spindle Subassembly	102
Enclosure Subassembly	104
Testing Data	Error! Bookmark not defined.
Arduino Code	111

EXECUTIVE SUMMARY

Problem Statement

Aerospace and military companies, who use parachutes for vehicle recovery, require parachute reefing - the incremental opening of a parachute canopy to limit the parachute opening forces to a predetermined value - to limit the impulse on both the parachute and the vehicle, reducing the structural mass required to survive this impulse. The current method of disreefing uses reefing line cutters that employ a pyro-time train and cutter knife to sever the reefing line, allowing the parachute to open between discrete reefed diameters, or reefing stages. A major step forward in the parachute industry would be a mechanism that performs continuous disreefing to replace reefing line cutters, as this would reduce the impulse on the system further while requiring less time to reach full inflation. Several preliminary investigations of continuous disreefing have been conducted, but none have pursued the topic with sufficient depth to create a practical solution. By conducting a thorough analysis of the physics of continuously disreefed parachutes and developing a robust prototype, we can create a practical continuous disreefer that can reduce loading on parachutes by up to 50% as well as providing a system to further investigate the empirical physics of continuously disreefed parachutes that has never been done before.

System Features

Continuous disreefing will allow for the parachute to open gradually, rather than in the 2-3 stages it is currently released in. For this continuous disreefing to occur, additional reefing line will need to be added to the skirt of the parachute and it must be released in a controlled and predictable manner. Our design includes a integrally contained spool on which the line is stored yet is as small and light as possible, given this volume requirement, to reduce impact on the overall parachute system as well as avoiding as much snatch force as possible during deployment.

The mechanism we designed must be fault tolerant to a safety factor of 2, as is standard in the aerospace industry. We built the system to be as fault proof and tolerant as possible. This included an active and passive braking system, ensuring that electronic failure will still result in a continuously disreefed parachute, albeit a suboptimal deployment.

The passive braking system consists of a system of capstans, which reduce the line tension experienced by the active braking system, as well as viscous damping in the spool bearings. These systems together reduce the work requirements of the active braking system while ensuring that passive disreefing occurs reliably should the electronics of the active brake system fail.

The active braking system utilizes data from a GPS chip and a rotary encoder on the spool to supply velocity, altitude, and line length (translated to parachute diameter) data that is processed by an onboard computing system to control a servo driven friction brake. The custom gearbox friction brake ensures that a large braking force can be applied and controlled with speed and precision without the risk of freezing fluid, which would occur with a hydraulic braking system.

These braking systems together control both the velocity and length of line let out from the spool in order to achieve a predetermined diameter profile. This diameter profile was derived through analysis of the parachute system while maintaining a constant parachute load. However, as further testing is conducted by NASA, if the the actual required diameter profile differs from the theoretical result, our device functionality will not need to be altered beyond this input curve.

Continuously Disreefed Parachute Analysis

There are three main forces acting on the parachute and capsule system: the drag force on the parachutes, the drag force on the capsule, and the force of the system's mass. The objective of continuous disreefing is to reduce the impulse experienced by the parachute and capsule system, which can be achieved by maintaining a constant drag force on the parachutes. This upwards drag force is a function of the parachute's diameter and the velocity of the overall system (The equations will be discussed in detail in the parachute analysis section). Since a constant drag force was our objective, we set the parachute term equal to the initial snatch load of a 3% reefed diameter and used a simulink model to determine the appropriate diameter and velocity profiles that would result in this constant force. This analysis was essential to designing our device, as it illuminated the shape of the diameter curve which would drive the design of our device.

System Validation

Since full scale testing was not a viable option, we conducted a series of pseudo-static tests on the various sub-components of our mechanism and developed a complex simulation that utilized the results of the pseudo-static testing to thoroughly validate the functionality of our device. The pseudo-static tests allowed us to characterize the function of various components, which was then used to give the dynamic model real, verified parameters. These parameters gave us confidence that our model could prove that our device could both withstand the expected loads and control the line as desired to achieve the diameter profile necessary for successful continuous disreefing.

Using the MTS machine, we conducted isolated capstan tests that verified a 10-times force reduction through the capstans. Additionally, we ran independent tests on the spool to determine its friction and viscous damping coefficients, both of which were small but critical parameters to understand what must be altered in our device to ensure that passive disreefing would occur reliably, should the active system fail. In order to understand the relationship between the magnitude of the braking force applied by the active braking system and the angular position of the servo motor, we ran various MTS tests in which we varied the servo position and collected load data. This allowed us to characterize the precise loading on the brake resulting from each servo position, showing the precision with which we could regulate the tension in the line. Finally, we ran a series of integrated system tests in which we controlled the descent of a 100lb mass across 1.5 meters of height. In these tests, we validated both the position and velocity control of our active braking system, ensuring that the system could detect both metrics reliably and that it could regulate the velocity of the falling mass with precision.

Using the parameters gathered through our pseudo-static tests, we developed a dynamic model that compares the drag forces and diameter profile of the parachute using our mechanism to the ideal case of continuous disreefing. The model first calculates the ideal diameter profile that would result in a constant drag force based on the initial conditions of the system. A second model then takes this ideal diameter and the experimentally obtained variables to simulate the dynamics of our mechanism, outputting a more realistic diameter profile. This diameter profile is then fed into a third model that outputs the force profile achieved through the use of our device. The results of the simulation confirm the success of our mechanism and both the diameter and force curves obtained from the dynamics of our system match the ideal cases of continuous disreefing within an error of 1% of the ideal parachute load.

System Results

Parameter	Goal	Actual
Impulse Reduction	50%	28%
Time to Full Inflation	45 seconds	17 seconds

Utilizing the system of pseudo-static testing with our integrated simulink model, we found that our system fell short of our force goals but provided serious improvement on the time to full inflation, providing a great expansion of the current NASA deployment envelope. Our stakeholders were particularly excited about this benefit, as the current deployment envelope is the most limiting factor in parachute system design.

The goal of a 50% force reduction was based on a ballpark estimate from Knacke's manual on parachute design. This estimate stems from a mathematical model that assumes the parachute would initially be reefed to a 0% diameter and opened continuously to full inflation. However, when we spoke with Tyler Schlenker at SpaceX, he explained that parachutes cannot practically be reefed beyond a 3% diameter, as a parachute at a smaller diameter would not reliably inflate. Further, as demonstrated in our analysis, the peak forces experienced by a parachute system are caused by the snatch of the exposed diameter, which thus limits the minimum parachute load to the load experienced at this 3% diameter. Therefore, our actual impulse reduction could not physically reach the theoretical 50% minimum, instead achieving the 28% shown by our model.

We were pleased to see that our system will achieve full inflation significantly faster than current staged disreefing, reducing the inflation time by nearly three times. This reduction comes from the requirement that the same amount of kinetic energy be dissipated by the drag of the parachute system regardless of the method of disreefing. Since our system holds the parachute load at a higher force than the load experienced between reefing stages, we can dissipate this energy at a significantly faster rate than staged reefing. This has huge implications for parachute recovery systems, as the safe deployment envelope is severely limited by the time to reach steady state velocity. The active controls of our system also mean that this time or force can be adjusted in various parachute failure cases to still achieve safe disreefing and landing. Current staged disreefing systems cannot adjust to handle off-nominal cases, resulting in massive force spikes when parachutes fail to inflate. Our system, however, will adjust its opening profile to hold a constant load regardless of parachute failure, simply inflating in a slightly longer period of time, though this time is still below the nominal 45 second threshold.

TEAM ROLES & CONTRIBUTIONS

Full Name	Project Focus	Secondary Focus	Email Address
Rome George Arnold IV	Mechanical Manufacturing	Test Engineering	arnoldr@seas.upenn.edu
Eugenia Bejar	Project Management	Research and Development	bejare@seas.upenn.edu
Pele Collins	Mechanical Design	Computational Analysis	pelec@seas.upenn.edu
Max Herman Newberger	Test Engineering	Mechanical Manufacturing	newmax@seas.upenn.edu
Michael James Pearson	Research and Development	Project Management	mpea@seas.upenn.edu
Rosalind Fish Blais Shinkle	Computational Analysis	Mechanical Design	rshinkle@seas.upenn.edu

Rome George Arnold IV

Rome Arnold, along with each member of the team, was heavily involved in developing and understanding of the physics of continuously disreefed parachutes. In the prototyping process, he worked with Ros Shinkle in investigating Eddy Braking for passive line control. In the final system development, he worked with Ros Shinkle to design the spool and active braking system. From there, he, along with Max Newberger and Pele Collins, focused heavily on the machining of the various system components and testing rigs. He was deeply involved in the pseudo-static testing process and testing rig manufacturing. Rome was the primary designer and content creator for all of the Powerpoint presentations.

Eugenia Bejar

Eugenia Bejar served as the team's project manager who headed the project's development and was responsible for all team assignments. Amongst Eugenia's principal roles was the management of the team's budget and ordering of all materials and components required for the manufacturing of the Daedalus. Throughout the project, Eugenia was involved in both prototyping and analysis, particularly on the rip-stitch prototype that she developed alongside Max Newberger. Along with the rest of the team member's, Eugenia was heavily involved in developing the analysis of the parachute system that allowed for the creation of our mechanism. Additionally, together with Michael Pearson, Eugenia further worked on the added mass analysis of the parachute system. Eugenia consistently completed all the team assignments required for the class and played a principal role in the creation of the team's design day demo and presentation.

Pele Collins

Pele Collins was the mechanical design and manufacturing lead of the team. Throughout both the initial prototyping phases and the final design of the system, Pele created the fundamental system designs based on the system characteristics and the analysis the team had outlined. In the first iterations of the mechanism, Pele worked with Michael Pearson to create the rudimentary friction brake design presented at the end of the Fall semester. Thereafter, he worked alongside the team members to further develop this mechanism and, upon thorough analysis of the forces at play, created the final model which the team later developed. Together with Max Newberger and Rome Arnold, Pele worked on manufacturing the various components of the system. Pele also created a Simulink model that compared the Daedalus's performance to that of the ideal case of continuous disreefing, thereby validating the mechanism's functionality.

Max Herman Newberger

Max Newberger was heavily involved in the analysis of the various components of the mechanism. Specifically, Max developed a COMSOL model to test the rip-stitch prototype he developed with Eugenia and later did extensive fluid analysis of the Daedalus to observe its behavior during parachute deployment. In the final mechanism development, Max worked alongside Pele to design and manufacture the capstans that are at the core of our friction brake component. As the team's testing lead, Max was involved in the design and manufacturing of the testing rigs and lead the pseudo-static testing process.

Michael James Pearson

Michael Pearson was initially involved in creating the initial simulation to understand the parachute dynamics and how the capsule dynamics related. During the prototyping process, he worked on looking at an entirely passive friction brake and developed a rudimentary prototype to show how the device would work. Once an active and passive system had been decided on, he worked to develop the parachute dynamics further and integrated added mass calculations into the model. Once the final prototype had been designed, Michael worked with the microcontroller to write the initial program to control the brake depending on the position of the encoder as well as creating the electronics subassembly. Along with the rest of the team, Michael aided in the testing of the mechanism and the development of the electronics subassembly.

Rosalind Fish Blais Shinkle

Rosalind Shinkle, along with the rest of the team, was very involved in understanding and modeling the physics of continuously disreefed parachutes. In the prototyping process, she worked with Rome Arnold to investigate eddy braking as a possible mode of passive line control. In the development of the final system, she worked with Rome Arnold to design the spool and active braking system, notably ideating and designing the mechanical caliper brake. She contracted with an outside manufacturer to produce the active brake housing and aided in the non-machining manufacture for the final model, including leading the carbon fiber layup. Rosalind aided in both the pseudo-static and line control testing procedures.

1. NEED AND BACKGROUND

Idea Origin and Proof of Need

The idea for this project was brought to us by Tyler Schlenker, the manager of the Parachute Recovery System team for the Dragon Spacecraft at SpaceX. According to Tyler a “major step forward in the parachute industry would be a mechanism that performs continuous disreef [sic] to replace reefing line cutters.” This view is echoed by Theo W Knacke in his in-depth reference book *Parachute Recovery Systems*. In the section about reefing parachutes, he states that, “Many attempts have been made to develop a reefing system where the opening of the parachute canopy is governed by a preselected force-time diagram. This approach has been called *continuous disreefing* in the literature ... However, none of these attempts has, so far, resulted in a practical solution” [1].

To further affirm the need for this system, we reached out to members of the CPAS team (Orion’s parachute system) at NASA as well as engineers at Airborne Systems. Ricardo Machin, Chief Technical engineer for CPAS, said in correspondence that “continuous reefing is a sort of grail within the world of parachutes.” When asked about why such systems do not exist yet, he commented that “part of the issue, with folks not publishing, is that the work is most often tied to business opportunities; to publish is to lose advantage (as it were); makes academia a unique place to come from.” Also, due to the high risk and need of empirical testing of parachute reefing systems, they are somewhat limited to using what has worked in the past. His colleague, James McMichael, echoed this position.

Rob Sinclair and Kyle Starr, both Engineers at Airborne Systems, the company that makes the vast majority of parachutes for manned spaceflight in the U.S. as well as those for numerous military programs, both expressed the need for this mechanism. They have provided us with clear design requirements and were a resource regarding parachute system integration throughout the course of the project.

Parachute Types

Fundamentally, parachutes increase air resistance to greatly reduce an object’s velocity. Parachutes are typically made of woven nylon fabric, sometimes reinforced with silicone coatings to provide longevity and consistency of performance. The woven fabric is held together with radial and diagonal seams, with suspension lines sewn directly into the radial seams. The area between any two radial seams is known as the “gore.” Often, the parachutes are constructed of multiple layers of air-permeable nylon weaves rated to specific tensile strengths, and seams rated to specific tear strength. These factors, along with size, are varied based on the use requirements of the parachute. There are many types of parachutes with unique combinations and variations providing different advantages and use cases. The four most common categories are round, ram-air, ribbon chutes, and drogue chutes.

Commonly, parachutes are deployed using smaller chutes, mainly pilot or drogue chutes. The small chute can help correct the orientation of a falling craft before the main chute is deployed to ensure tangling does not occur. Further, the minimal drag of the drogue chute can provide a small drag force to slow the craft down before deploying the main chute, without imparting a large impulse on the rigging system. Occasionally, the drogue chutes are also used to aid in the deployment of the main chute to ensure it can fully inflate away from the aircraft.

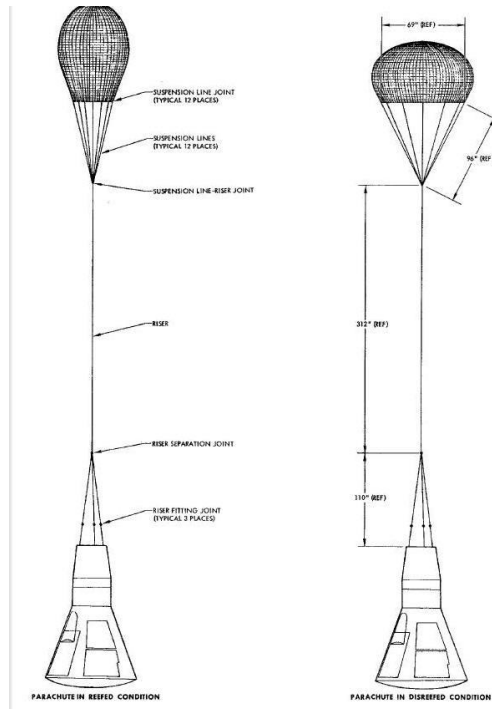


Figure 1.1: Pilot Chutes [2]

Round parachutes are pure drag chutes, providing no lift, and use a hole in the center to control airflow and allow for a stable descent. Forward speed can be achieved using small slits in the rear of the canopy. Round chutes are used for static-line jumps and payload drops, as they require minimal control. They can also be deployed in bundles, as done in the Apollo missions, which allows for lower chance of failure and aids in construction and packaging of the chutes.

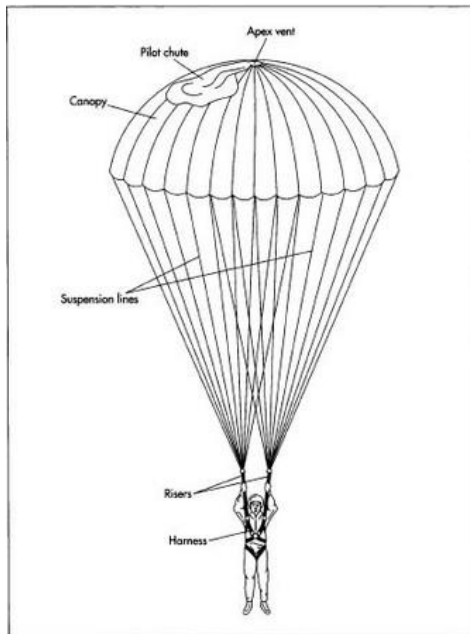


Figure 1.2: Round Parachute [3]

Ram-air parachutes, on the other hand, have a rectangular shape that can provide lift and are highly maneuverable. These are most commonly employed in personal operations, like skydiving,

and certain high-precision military operations. The lift provided by the chute allows the rate of descent to be varied, while the forward momentum and specialized rigging allows the chute to be turned and directed as needed. However, the high maneuverability makes these chutes less useful for spacecraft recovery operations, as small variations in loading could cause the chute to turn and the craft to land in less predictable locations.

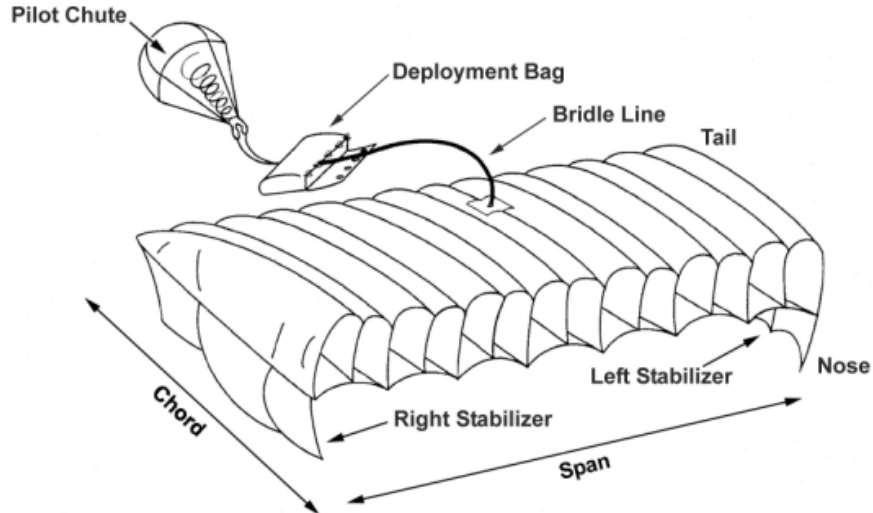


Figure 1.3: Ram-air Parachute [4]

Ribbon parachutes are a variation on round chutes designed for supersonic deployment, where a traditional parachute would burst. Ribbon parachutes use a ring-shaped geometry with a large central hole in the apex to reduce pressure in the chute. Under high-load conditions, ribbon parachutes are most effective. They are constructed with multiple overlapping rings of material, producing significant drag without building large pressure within the canopy. For the sake of this project, any references to parachutes will refer to ribbon parachute types unless otherwise specified, as these are the most commonly used in space recovery operations.

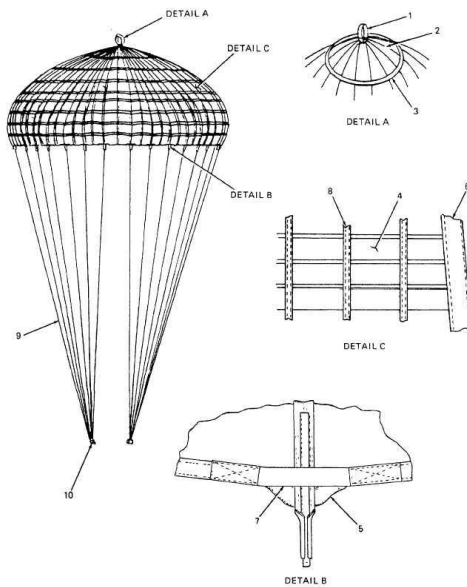


Figure 1.4: Ribbon Parachute [5]

Parachute Reefing

A common problem in parachute deployment is known as wake recontact. When a parachute produces rapid decelerations on a payload, the previously generated wake of air will overrun the inflated parachute, causing the parachute to temporarily collapse and reducing the drag force produced. In order to eliminate this phenomenon and reduce extreme impulses on the parachute system and payload, parachute reefing was developed.

“Parachute reefing permits the incremental opening of a parachute canopy or restrains the parachute canopy from full inflation or over inflation” [1]. Reefing therefore achieves several functions in a parachute system:

1. Limits the parachute opening forces to a predetermined value through successive steps of parachute opening, called reefing steps, at predetermined time intervals.
2. Reefing the parachute to a low drag area permits a more accurate drop from high altitude. Low-impact velocity is then obtained by disreefing the parachute shortly before ground impact.
3. Allows deployment of aircraft landing deceleration parachutes during approach for landing approach control. Disreefing the parachute at touchdown provides a powerful landing brake.
4. Increases parachute stability by a slight amount of fixed reefing.
5. Provides an over-inflation control line (OC line) that lets the parachute open fully but prevents overinflation. The OC line decreases the parachute opening force by limiting the force overshoot at final parachute inflation.

Therefore, it is clear that reefing mechanisms are greatly required in parachutes primarily because, if the parachutes were allowed to fully inflate immediately upon deployment, the high velocity of the vehicle in combination with the high drag force of a fully inflated parachute can be disastrous. It would result in extremely high shock forces on both the canopy and all the components in the parachute system. Reefing is used to limit this shock load so that any interacting components can be made smaller and lighter. Particularly in an industry like aerospace, mass saving is a critical component of any part design. Having lower limit loads allows one to reduce the size of the component that would need to survive that limit load.

Reefing a parachute begins with the analytical determination of the various drag-area stages and the required timing steps. The analysis is best accomplished in computer simulations. These programs thus determine the number of reefing stages, the timing of the stages, and the velocity, as well as the altitude, trajectory increments based on maximum allowable parachute force, parachute force balance in the reefing stages, minimum recovery altitude, and other related requirements. We will use our computer simulation in order to determine the load levels that our device could expect to encounter during operation.

Reefing Methods

Parachute reefing was first developed and employed in Germany in 1941, for use on the Ju 52 aircraft during landing. The ribbon parachutes of the aircraft were deployed to slow the aircraft, reefed using a system of lines attached to the attachment points of the suspension lines. The chute was then disreefed upon touchdown by pilot command, firing a cutting mechanism that

would release the lines [6]. This was later replaced by skirt reefing, which is still the main method employed today. However, a few other methods, including vent reefing and slider reefing, have been used in some modern designs in specific applications.

Staged Skirt Reefing

Staged skirt reefing is the most commonly employed reefing method in round parachutes, typically used in space travel and military operations. Reefing rings are attached to the canopy skirt at the connection point of each suspension line. The reefing line, a continuous line that restricts the opening of the canopy, is guided through the reefing rings and a plurality of reefing-line cutters. Each cutter contains a pyro-time train and a cutter knife that is initiated at canopy deployment by pull cords attached to the suspension lines or to the canopy. After a preselected time, the pyro-charge in the cutter fires, and the knife severs the reefing line, allowing the parachute canopy to open fully or enter the next reefing stage. A diagram showing a basic, single-stage setup is shown below in Figure 1.5. Often, multiple reefing lines with multiple cutters are employed to ensure reliability in case of failure. For example, the Apollo spacecraft employed two cutters per line and two reefing lines per reefing stage to ensure not only that the lines would be cut, but also that if one line were cut prematurely, the second line would not allow the reefing stage to open before intended [6]. This serves as evidence of the need for sufficient redundancy in any reefing system.

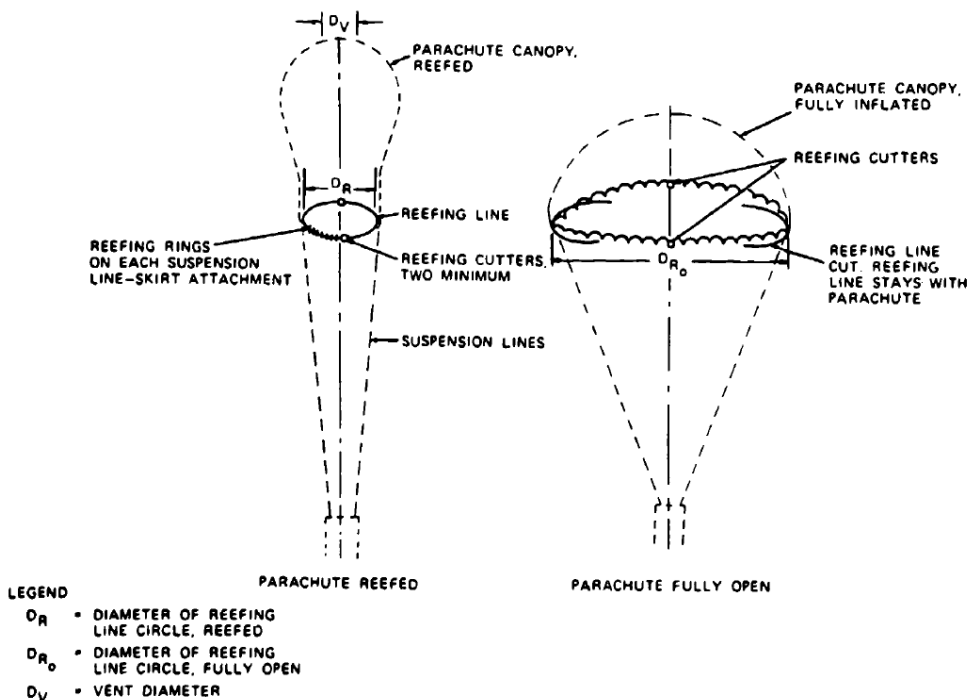


Figure 1.5: Diagram of single stage, skirt reefing setup [1]

Vent Reefing

In vent reefing systems, the parachute is held in an inverted state by lines attached to the vent of the canopy (at the peak of the parachute), which reduce the effective drag of the chute. In multiple stages, the lines holding the canopy in an inverted state are cut, thus incrementally disreefing the parachute until complete inflation. This system is used less frequently, as the

counteracted pulling forces often cause extreme forces in the suspension lines. Figure 1.6 illustrates a basic vent reefing configuration.

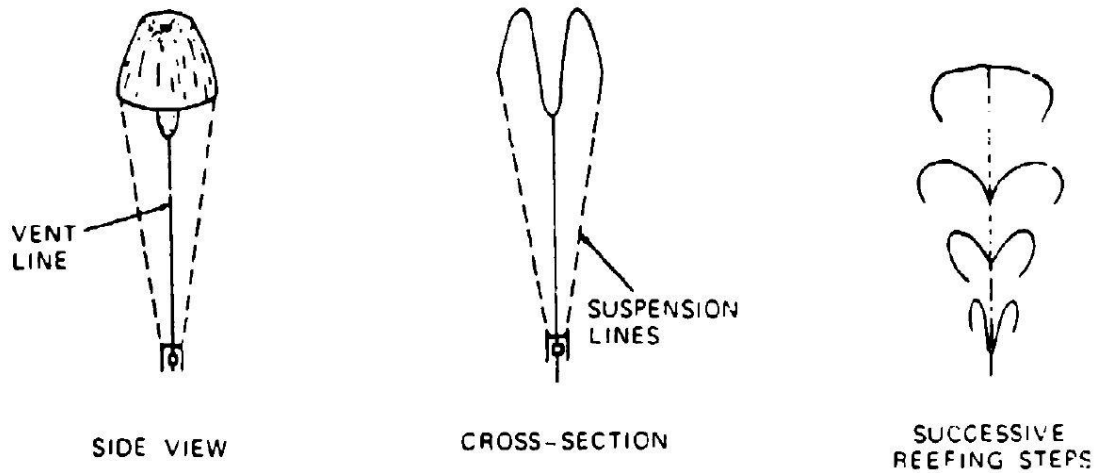


Figure 1.6: Vent Disreefing [1]

Slider Reefing

Slider reefing mechanisms are most typically deployed with ram-air parachutes, though some systems have been developed and patented for round chutes. The first slider reefer was patented by German inventor Oswald Schade in 1953, designed in tandem with a personal-use sport parachute [7]. Since then, sliders have been iterated and developed, including a modern mesh-slider, the style of which is used in nearly all ram-air parachutes [8]. A slider for larger, round chutes, designed to take larger payloads than those of previous slider reefing systems has also been developed [9]. Effectively, slider reefing systems restrain the opening of the parachute by holding the suspension lines to a specific geometry and slowly disreefing the parachute as the loading in the lines pushes the slider down the lines. While this system does create some level of continuous disreefing, they are unable to create the continuous disreefing required in the extreme loading situations experienced by spaceflight and aircraft recovery systems. An illustration of slider function is depicted in Figure 1.7.

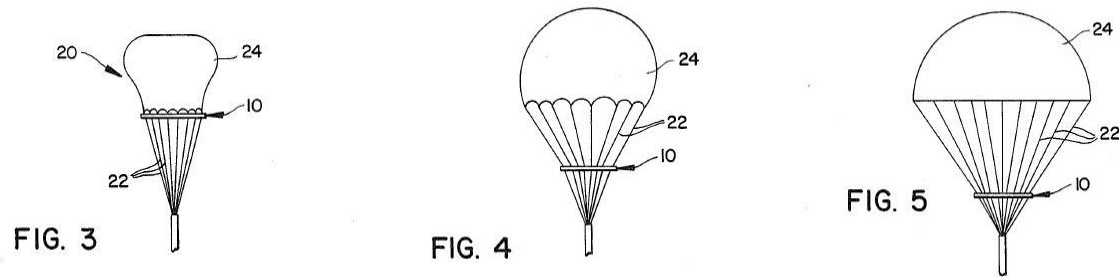


Figure 1.7: Slider reefing mechanism [9]

Innovative Reefing Practices

A handful of patents exist around the notion of using the chute itself or drogue chute to reef the

main chute, the most relevant being patent number US 3,540,684 (1970) and patent number US 3,945,592 (1976). Both systems are designed around ram-air chutes, using folded systems to allow the drag force to slowly unfurl the chutes. The 1970 patent utilizes a number of different drogue chute configurations and a complex rope system to slowly unfurl the ram-air chute.

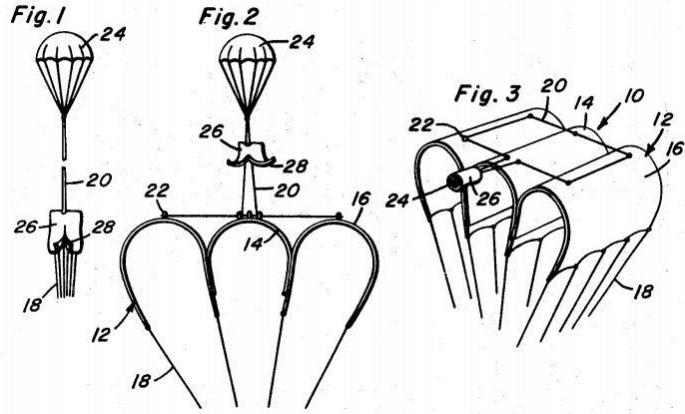


Figure 1.8: Drogue disreefing system [10]

This type of system, however, would not be applicable to the round parachutes used on spacecraft due to the need to fold the main chute in a very uniform way to have it subsequently unfurl.

The 1976 patent provides an interesting method of opening and reefing the ram-air chute using a plurality of small holes, figure 1.9, that allow the ram-air chute to inflate and have a more controlled reefing deployment. Effectively, the holes allow airflow to help the chute inflate (a requirement of ram-air chutes), while lines from the user are attached to reefing lines within the chute allowing it to open more slowly.

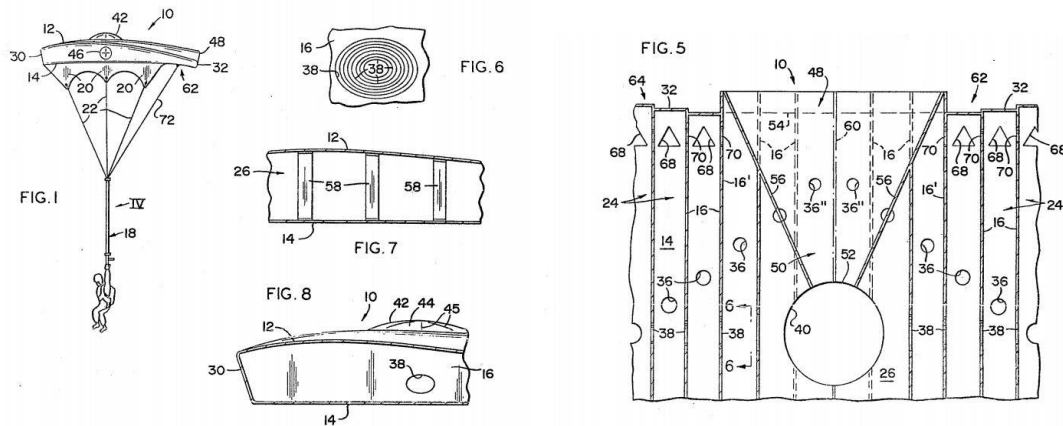


Figure 1.9: Airflow disreefing system [11]

This system is also specialized to ram-air systems, but it could serve as an inspiration for an integrated approach to the disreefing of the parachute.

Overall, these integrated continuous disreefing methods are interesting and will serve as inspiration for our ideation. However, they alone will not be sufficient for large scale aircraft situations, as they apply only to drogue chutes and would likely not work well under the extreme

magnitude of forces experienced in spacecraft recovery.

Parachute Opening Load Control

The effects of reefing on the parachute opening load are presented in the simplified figure below. Parachute opening load (force) versus time curves are shown for three different kinds of parachute deployment methods. The upper force-time curve is typical of a parachute deployed with no reefing. The center force-time curve is typical of a parachute with two reefing stages and a final full open stage. The lower solid line is typical of what the force-time curve would be if a continuous disreefing system were used. The lower dashed line is the level at which the parachute force is equal to the system weight. This is the parachute force level during equilibrium descent conditions. Obviously, a parachute system designed to withstand an unreefed deployment must be much stronger and therefore heavier than a parachute system with reefing capability, which in turn has to be stronger than a system designed to withstand continuous disreefing.

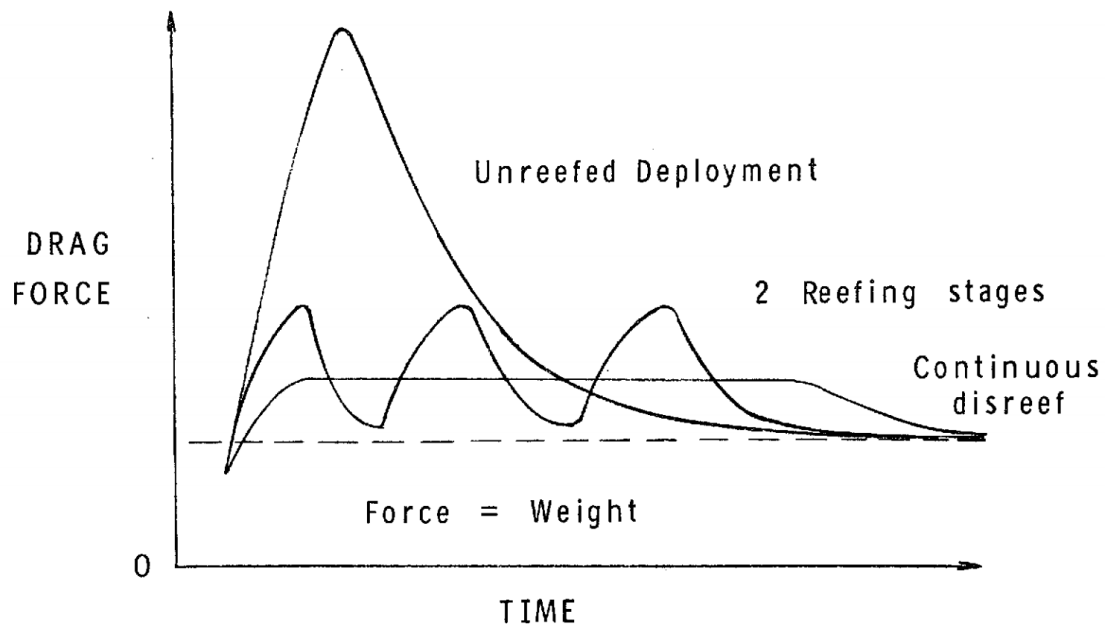


Figure 1.10: Parachute Opening Load Control [12]

2. OBJECTIVES

Our objectives for this project were obtained by speaking to our stakeholders at NASA, SpaceX, and Airborne Systems, who manufacture and package the parachute systems for many space and military applications. From these conversations, we were able to better understand the parameters of the system we were designing and the environments it had to endure. As we developed our device, we continually checked in with these stakeholders to ensure that our device would meet their needs, often discovering new characteristics to which our device would be designed. Thus, we obtained both system and reach characteristics as well as an idea of the standards that we had to meet.

System Characteristics

Basic Characteristics

Characteristic	Description	Quantitative Range
Endure high forces	Must be strong enough to handle extremely high forces	600 lbf anticipated maximum reefing line tension
Reduce time to full inflation	Must reduce or maintain the current time for the parachutes to fully inflate	Current full inflation time for nominal reefed deployment is 45 seconds
Low weight / volume	Must be compatible with existing systems	Current solutions used are a total of 1.25lbf and only a few inches in diameter
Reduction in overall system weight	Must reduce overall weight	Overall, parachute systems weigh around 315 lbf
Allow variable disreefing rates	Our system must be able to disreef line at variable rates depending on load	Controlled line release at rates between 12 in/s and 24 in/s

Reach Characteristics

Characteristic	Description	Quantitative Range
Reusable	Our system, if expensive, should be reusable to minimize cost	Reefing line cutters for commercial planes cost ~\$1200 per cutter
Off-nominal functionality	Our system should adapt to off-nominal cases, such as failure of a single parachute	Current disreefers are not adaptive, instead over designed for off-nominal cases
Endure large temperature range	Our system will see a large range of temperatures and must be fully functional in all	Must be fully functional between -45°F to 200°F

Work if active system fails	Our system should allow the payload to land safely even in active brake failure	Passive system should reduce the load enough to open up the parachute slowly enough to allow a safe landing
Adaptable to different systems	Our system should be able to be used on different companies' modules or with varying reefing line size or material	Varied parachute diameters would result in different reefing line lengths and different diameter profiles
Withstand high temperatures for long periods	Our system should meet all edge cases particularly with respect to temperature	Some systems experience 300°F temperatures for up to 48 hours

Design Impact of Engineering Standards

As our project focused on the parachute system of the NASA Orion Capsule, we were required to meet NASA's engineering standards. As a result, there were many separate specifications that shaped our design, detailed below. The standards are separated into sections for clarity and to distinguish between the various types of standards Daedalus had to satisfy.

NASA Standards

Safety and Life Factors

When considering life-safety critical systems (as parachute systems are), it is essential that Daedalus met all desired safety and life factors. First of all, when making material decisions, all components had to meet the safety factors for Metallic Structures. Thus, every metal component was designed to meet a 1.4x Ultimate Design Factor [13]. This mandates that the ultimate stress of the material in the component is at least 1.4 times the stresses expected in operation. Any fasteners or joints also fall under NASA design standards. Like the metal structures, any safety critical joints must have an ultimate strength safety factor of 1.4 and meet a joint separation safety factor of 1.4 [13].

In addition to safety factors for loads, there are also safety factors for fatigue and creep. Though we were unable to test the full life cycle of our product, we still designed with these standards in mind. Specifically, "for NASA spaceflight structures made of well-characterized materials and with sufficient load cycle data that accounts for all in-service environments, a minimum service life factor of 4.0 shall be applied to the service life for fatigue and creep-life assessments" [13]. Therefore, if we were able to test for the full life of our product, it should be able to survive at least four drop tests to allow it to meet the outlined standards. In our pseudo-static testing (described in detail in a later section), we performed dozens of cyclic tests on our device, giving us confidence that it would meet this lifecycle requirement. However, given that Daedalus will likely be a single-use device (as is the case for all parachute components), this standard serves only to provide confidence in the reliability of the system.

Mechanism Design

For general mechanical design, the standards were similar to the safety and life factors, but NASA has very specific standards for each type of mechanical mechanism. For our rotating disc brake, there is a standards section which outlines safety factors and tests [14]. The standards specify that all tests should either be conducted in the operational environment or an environmental correction factor should be applied if testing in non-operational conditions. Along with this section on Rotating Machinery, there is also a section denoting the method for determining Rotating Machinery Fatigue which, if we had more time and resources, we would meet by testing all of our rotating components to their limit to ensure appropriate standards are met. Further explanation of our stress analysis of the rotary system is detailed in the next section.

All fasteners and joints also have a section which outlines similar standards [14]. These standards set out a fitting factor of 1.15 which should be applied to the limit and ultimate load conditions. Furthermore, as our design contains frictional braking, we must also abide by the standards for “Loads due to Friction” [14]. Our analysis and design follow all standards concerning friction.

Software and Electrical Engineering

Since our system integrates an active control mechanism, we had to consider all NASA standards for electrical systems. An example is the NASA standard for “Electrical Soldered Connections” [15]. This standard outlines all processes and the methods to implement soldered connections, as well as testing methods to ensure every part is completed to the correct specification. Unfortunately, within these specifications there exist tests and conditions that we were unable to meet due to budget constraints and inability to access to specific machinery / conditions. An example is the ‘Sodium chloride (NaCl) equivalent ionic contamination test’ which we could not perform as our cleanliness standards cannot meet those specified.

Outside of the physical electrical parts of our design, there are also many standards for software systems [16]. Although the whole of the standard: “NASA Software Engineering Requirements” is applicable to the software produced for our mechanism, there is a particularly pertinent section named “Safety Critical Software”. As our mechanism deals with safety critical systems, we designed our electronic system to meet this criterion. Some standards in this section are difficult to meet with our current design, but modifications could be made to appropriately meet them including meeting 3.7.2.a: “Safety-critical software is initialized, at first start and at restarts, to a known safe state.” This standard is primarily concerned with computational systems utilized beyond Earth’s atmosphere, as radiation hitting computers in space can corrupt data quite easily. To meet this standard, multiple microcontrollers are often connected in parallel to aid in an effective restart and boot into safe state, syncing the data across all three to ensure reliable function. While our device would only be in operation within the Earth’s atmosphere, we likely would redesign the future computational system to meet this standard, as the proper function of our device is mission critical.

Mathematical Modeling of Physical Systems

On top of meeting all physically tested standards, there are also standards, set out by NASA, for mathematical models. These standards, named “Math Models,” set out how to verify all mathematical models, by test and the appropriate factors that should be included, as well as how test and model data should correlate and the percentage errors that are acceptable [14]. For example, all stress and strain data obtained by physical test should be within 10% of the mathematical model values for the mathematical model to be verified.

Furthermore, throughout the aforementioned standards some statistical models were mentioned including NASA's famous P95/50 model. This standard states that NASA expects 95% probability of no exceedance with a 50% confidence level, resulting in a very low tolerance. Thus, every component of our mechanism had to be manufactured with utmost precision to ensure it matches the precision in our model. A more precise measure is also used in some standards specifying a "3-sigma" tolerance, meaning a probability of 99.87% of no exceedance, often paired with a 50% confidence.

Non-NASA Standards

Beyond space industry, the Federal Aviation Administration (FAA) does layout some guidelines for commercial space transportation, particularly reentry capsules. These rules are under FAA Part 431 subsection 25, they are:

- In its Reusable Landing Vehicle (RLV) mission license application, an applicant must:
- (d) Identify proposed launch and reentry flight profile(s), including -
 - (1) Launch and reentry site(s), including planned contingency abort locations, if any;
 - (2) Flight trajectories, reentry trajectories, associated ground tracks, and instantaneous impact points for nominal operations, and contingency abort profiles, if any;
 - (3) Sequence of planned events or maneuvers during the mission; and for an orbital mission, the range of intermediate and final orbits of the vehicle and upper stages, if any, and their estimated orbital life times.

Therefore, as the parachute controls the flight trajectory of the reentering capsule and our device controls the parachute, our device must be able to give an initial expected trajectory for any given landing scenario to comply with the standards set out by the FAA. This did not affect the mechanical design of our device, but it will factor into the flight control systems and future parachute analysis.

These rules also require that any high-altitude operation have well defined sites for launch and reentry, and that reentry must be planned fully. For someone to use our system they would need to alert the FAA how and where their payload will land. This requires our system to be consistent enough so that this information could be given to the FAA.

Designing to Meet Standards

In general, we made as much effort as possible to design our device to the above standards and the commonly known constraints of spaceflight systems. Some standards, particularly those pertaining to electronic systems, were considered but disregarded, as the budget impact of meeting those standards were beyond our means. The Daedalus disreefing device was designed to stand as a first prototype in a relatively unexplored field, so we focused instead on functional design for these types of components. In mechanical design cases, we intentionally exceeded NASA standards, designing our components to meet a 2x safety factor, as is the commonplace practice at NASA. We also focused on designing our device to avoid the use of any fluids, as we were unable to budget for any space-grade dry lubricants but did not want to skew our results by using any fluid lubricants.

3. DESIGN AND REALIZATION

Summary

The Daedalus can be broken down into two primary subsystems: the passive braking system and the active braking system.

The purely mechanical passive braking subsystem serves to decrease the tension in the reefing line that the active braking system has to combat and to ensure safe deployment should the active system fail. This subsystem consists of capstans, which are friction brakes that will reduce the tension in the reefing line tenfold, and viscous dampers mounted about the shaft of the spool, which would ensure that line velocity does not become too large.

The active braking system is designed to refine the deployment profile, responding to sensors to optimize the time to full inflation against the force that the capsule experiences. Sensors feed into a microcontroller, which calculates position and velocity of the craft, the position and velocity of the line, and subsequently determines the deviation from the ideal diameter profile. The microcontroller sends commands to a servo, which turns the primary gear of the mechanical caliper brake, applying more or less force to the brake disc to match the ideal diameter as closely as possible.

The Daedalus's dual system means that the mechanism is robust, still functioning in the event of electronic failure; precise, offering finely-tuned disreefing and leading to a safer, softer landing; and reliable, adjusting automatically to off-nominal landing conditions to ensure safe parachute deployment is still achieved.

The sections below layout how Daedalus has achieved these goals, beginning with an analysis of the physics that guided the systems development and constrain its impact. We then step through the down selection process that brought us to our final design space before explaining the details of the device. This opens with an overall analysis of the device and its subsystems before discussing the actual component design and manufacturing.

Physical Analysis of Continuously Disreefed Parachute Systems

Constants and Variables

Summary of variables:

Time Dep. Variable	Description
F_s	Force in suspension lines felt by capsule (N)
F_p	Parachute force per chute (N)
F_c	Drag force from the capsule (N)
D	Reefing line diameter (m)
\dot{D}	Velocity of reefing line diameter (m/s)
\ddot{D}	Acceleration of reefing line diameter (m/s ²)
v_y	Velocity of the capsule (m/s)

Summary of constants:

Constant	Description	Value
C_c	Drag coefficient of capsule	1.3
C_p	Drag coefficient of parachute	0.95
M	Mass of capsule (kg)	7802
ρ	Density of air at sea-level (kg/m ³)	1.225
n	Number of parachutes	3
g	Acceleration due to gravity (m/s ²)	9.81
A_c	Capsule area used for drag calculations (m ²)	19.63
A_p	Fully inflated parachute area used for drag calculations (m ²)	982
D_{max}	Maximum diameter of the reefing line (m)	35.36
m	Mass of the rope (kg)	TBD
$v_{y,term}$	Terminal velocity of the system (m/s)	6.65
Z_{term}	Constant force at terminal velocity (N)	75820

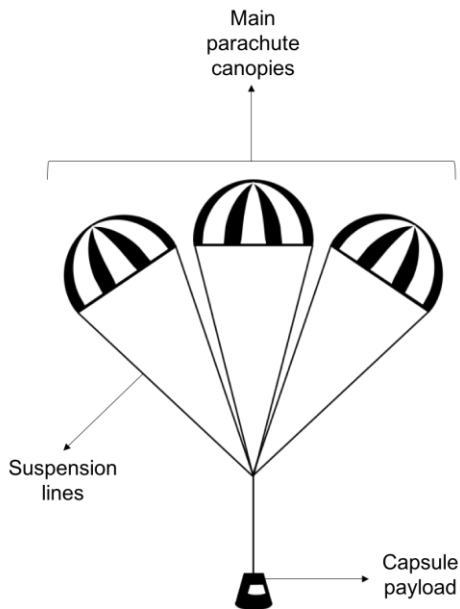


Figure 3.1: Parachute System

To begin the analysis, we performed a force balance on the entire system. Seen below, figure 1, is the force balance Free Body Diagram (FBD).

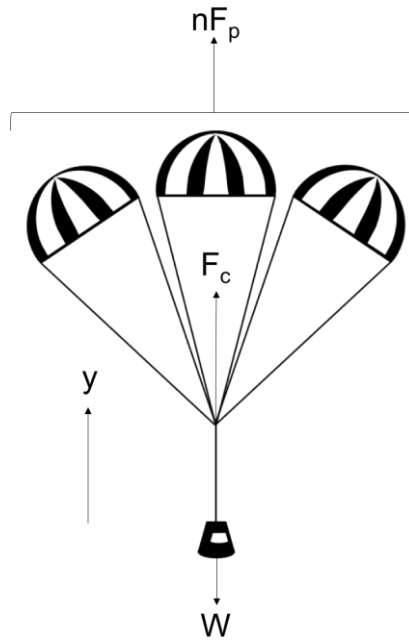


Figure 3.2: Parachute forces

This gives rise to the following equation:

$$nF_p + F_c - W = F_{net} = Ma_y \quad (1)$$

where M is the mass of the system, n is the number of parachutes, F_p is the parachute force, F_c is the capsule drag, W is the weight of the entire system, a_y is the acceleration and F_{net} is the total net force.

Using drag equations, we can make the following equivalencies:

$$nF_p = \frac{\pi}{8}\rho nv_y^2 C_p D(t)^2 \quad (2)$$

$$F_c = \frac{1}{2}\rho v_y^2 C_c A_c \quad (3)$$

Where ρ is air density, v_y is the y-velocity of the system, C_p is the drag coefficient of the parachutes, $D(t)$ is the time-dependent diameter profile of the parachute, C_c is the drag coefficient of the capsule, and A_c is the drag area of the capsule.

Which, as a result, gives the equation:

$$\frac{\pi}{8}\rho nv_y^2 C_p D(t)^2 + \frac{1}{2}\rho v_y^2 C_c A_c - Mg = Mv_y \quad (4)$$

Where v_y is the acceleration of the system and g is acceleration due to gravity. This equation defines the kinematics of the system as a whole. Next, we created another FBD looking solely at the parachutes and the suspension lines, detailed below:

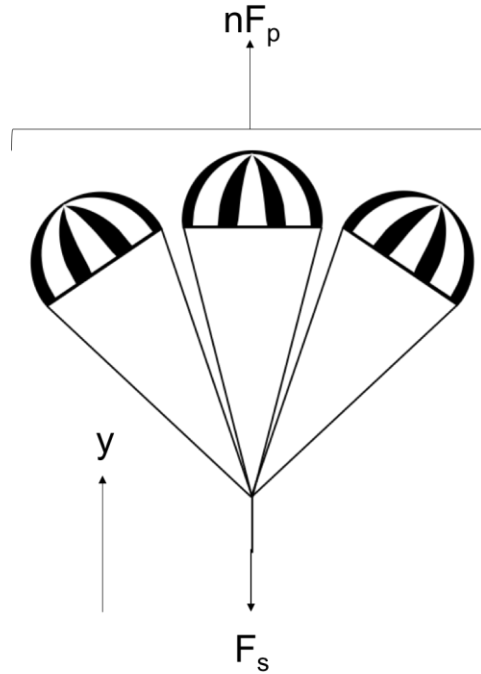


Figure 3.3: Parachute forces without capsule

This produced the following equation:

$$F_s = nF_p \quad (5)$$

where F_s is the force in the suspension lines. Meaning that to keep the force in the suspension lines constant, it is imperative to keep the force from the parachutes constant. Next, we named a constant, Z , which is the constant force the suspension line should feel throughout the disreefing process based on the drag produced by the parachutes.

$$Z = \frac{\pi}{8} \rho v_y^2 C_p D(t)^2 \quad (6)$$

Plugging Z into equation 4 we obtain:

$$Z + \frac{1}{2} \rho v_y^2 C_c A_c - Mg = Mv_y \quad (7)$$

Rearranging we see:

$$\ddot{v}_y - av_y^2 + b = 0 \quad (8)$$

Where $a = \frac{1}{2} C_c A_c \frac{\rho}{M}$ and $b = g - \frac{Z}{M}$.

Solving this differential equation, we obtain the following solution:

$$v_y(t) = -\sqrt{\frac{b}{a}} \tanh \left[\sqrt{ab}(C_1 + t) \right] \quad (9)$$

Where C_1 is a constant found using boundary conditions (initial deployment velocity, v_y). We obtained the value for Z based on the first force spike seen in the force vs. time graph given to us by NASA. This peak is known as the 'snatch force' and occurs as the parachute system is ejected from the capsule. Therefore, this was the minimum force that we could set our constant value of Z to. Therefore, from this, the following plots show the dynamics of the overall system as a function of time, using the $Z = \text{snatch force} = 88,000 \text{ N} = 20,000 \text{ lbf}$.

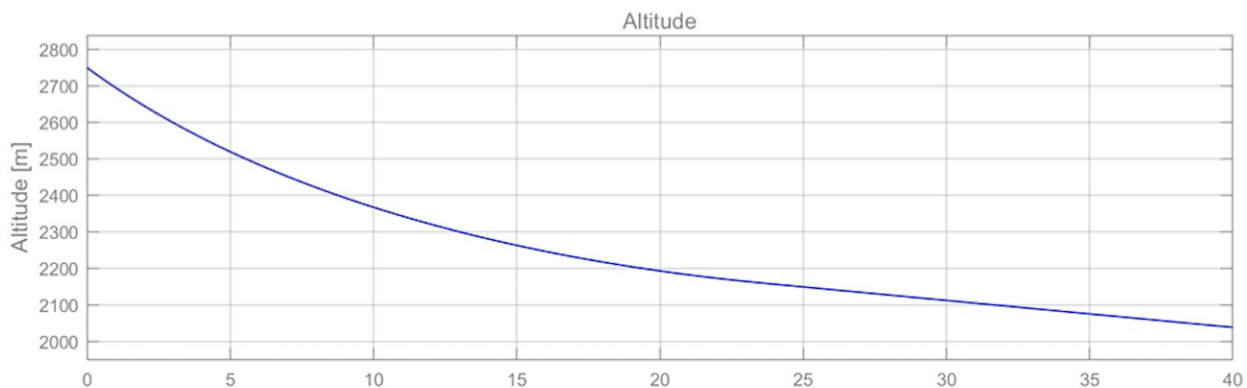


Figure 3.4: Altitude vs. time graph

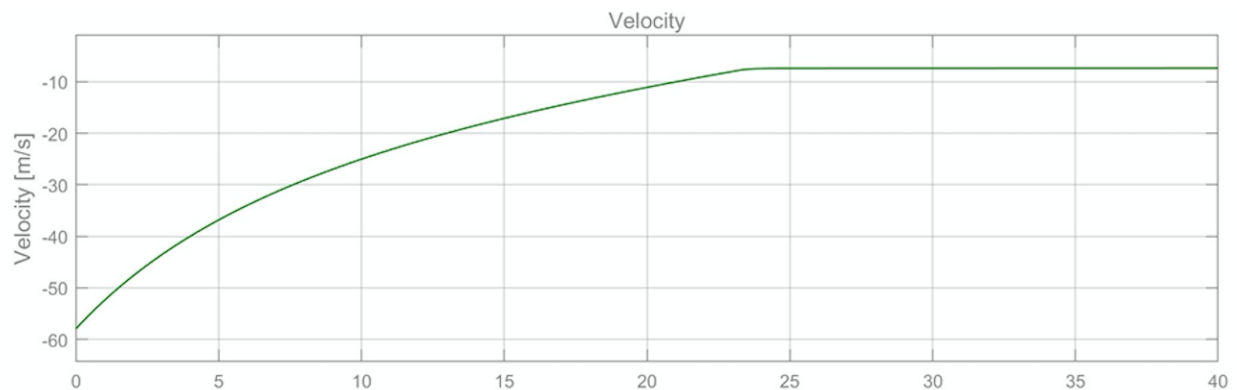


Figure 3.5: Velocity vs. time graph

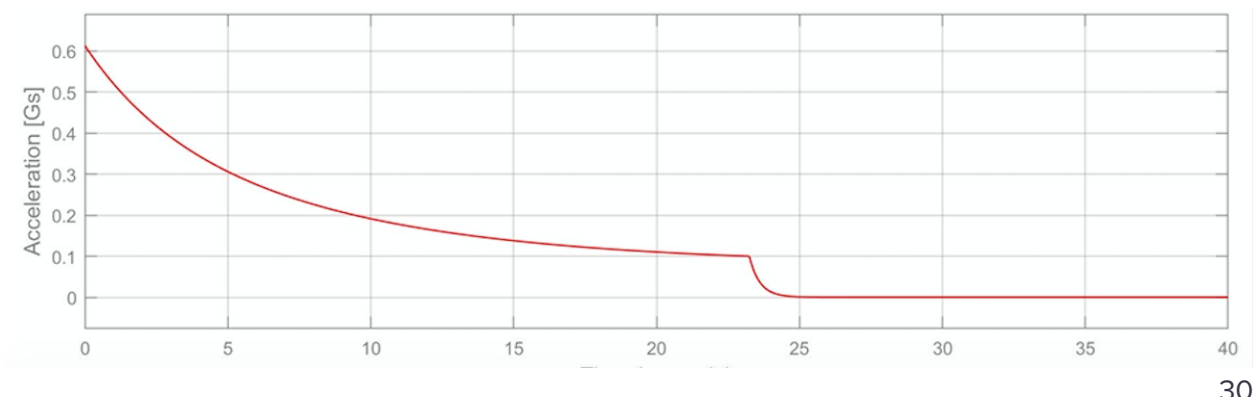


Figure 3.6: Acceleration vs. time graph

Knowing the velocity as a function of time, we can now solve for $D(t)$ the reefing line diameter, using the equation:

$$D(t) = \sqrt{\frac{8Z}{\rho\pi n C_p}} \frac{1}{v_y(t)} \quad (10)$$

Plotting these using MATLAB:

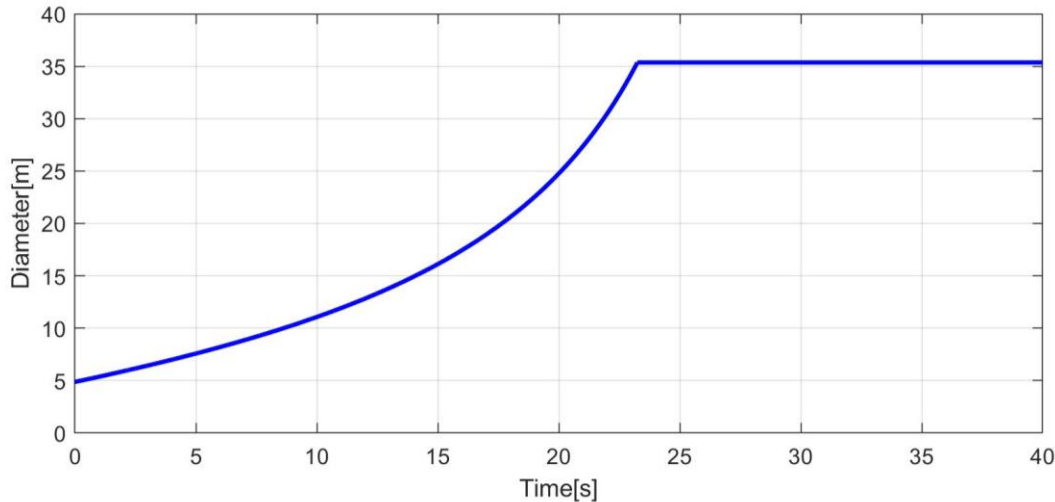


Figure 3.7: Diameter vs. time graph

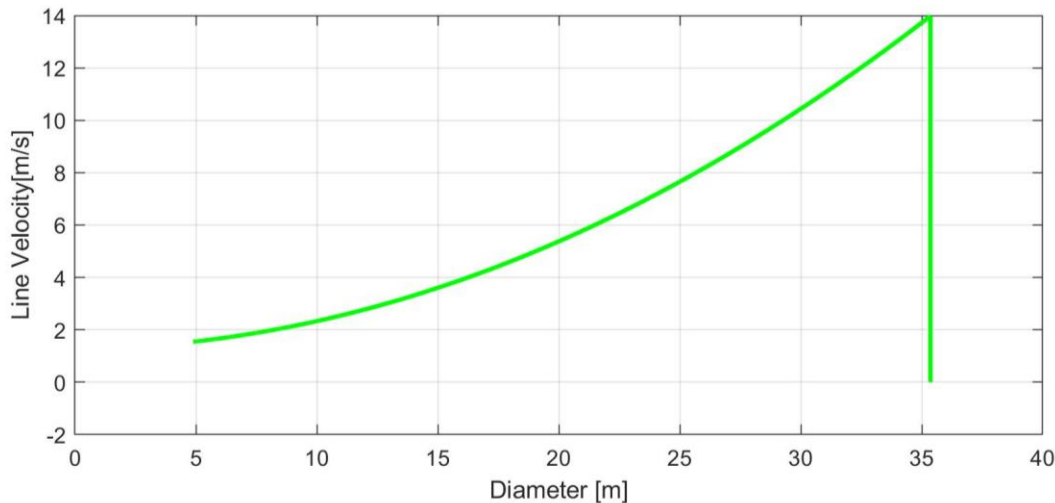


Figure 3.8: Diameter vs. time graph

Added Mass Considerations

As discussed earlier, the parachute force is controlled to be constant, setting it to a value of Z , where:

$$Z = \frac{\pi}{8} \rho n v_y^2 C_p D(t)^2$$

Rearranging this to solve for the velocity as a function of time:

$$v_y(t) = \sqrt{\frac{8Z}{\rho \pi n C_p}} \frac{1}{D(t)} \quad (11)$$

Taking the time derivative of $v_y(t)$, we can obtain an equation which will be useful later:

$$\frac{dv_y(t)}{dt} = \dot{D}(t) \cdot \frac{1}{D(t)^2} \sqrt{\frac{8Z}{\rho \pi n C_p}} \quad (12)$$

Next, we integrate the idea of added mass. Many papers have attempted to characterize the added mass of a parachute, but all differ in their conclusions. Added mass pertains to the enclosed mass of the air inside of the inflated parachute and how it affects flight dynamics. Added mass is a function of time and thus as the diameter of the parachute changes, so does the added mass. Many papers agree on basic dynamic equations and these have been taken and adapted to our system. First, by using equation 6, we included the added mass terms to obtain:

$$\frac{dm_e}{dt} \cdot v_y(t) + Z + \frac{1}{2} \rho v_y^2 C_c A_c - (m_e + M)g = (m_e + M)v_y \quad (13)$$

Where m_e is the enclosed mass of air inside the parachute.

If we use the simplification found in many research papers that the parachute at all times is a hemisphere, meaning that the enclosed mass is:

$$m_e = \frac{\pi}{12} \rho D(t)^3 \quad (14)$$

We are able to get equation 13 solely as a function of $D(t)$:

$$\frac{1}{M + m_e} \frac{dm_e}{dt} \cdot v_y + \frac{Z}{M + m_e} + \frac{1}{2(M + m_e)} \rho v_y^2 C_c A_c - \frac{\dot{D}(t)}{D(t)^2} \sqrt{\frac{8Z}{\rho \pi n C_p}} = g \quad (15)$$

Where $\frac{dm_e}{dt} = \frac{\pi}{4} \rho D(t)^2 \dot{D}(t)$

Despite being able to isolate a variable, $D(t)$, we found this equation to be analytically unsolvable. This was found to be the case by many other researchers and, as a result, added mass calculations are performed in other ways. For example, many of the papers that we used for data and mathematical help used drop tests videos to calculate inflation. From here, using force, diameter etc. data and their equations without added mass terms, they were able to correlate the error in their values with the inflation from videos. Sadly, without drop test footage and corresponding data, it is difficult to solve this problem. We have resorted to simplifying our model to incorporate as much as we can.

Down Selection Process

We created and analysed many system designs before deciding on our final method of continuous disreefing. Our designs ranged from passive systems which changed the design of the parachute to active systems which accurately controlled the growth of the reefing line. Below is a discussion of our designs, each with advantages and disadvantages. For each of the methods we decided against, we have given a detailed description as to why it was not chosen.

Parachute Designs

There may be a better potential for success by changing the design of the parachute. The goal is to change the design of the parachute to one that opens continuously, while upholding the performance that parachutes currently give.

Parachute Corset

The idea consists of a traditional ribbon parachute, cut on four 'sides' as shown in the diagram below.

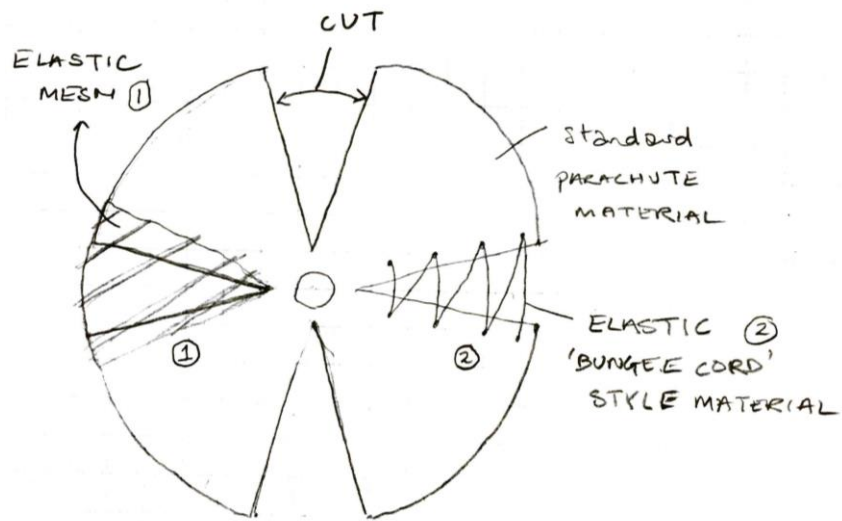


Figure 3.9: Parachute Corset Design

Two sides would be 'stitched' together with elastic cord or an elastic mesh. This would allow the parachute to open progressively as the radial force on the parachute increases and the elastic stretches to accommodate. Side ① shows the elastic mesh covering the cut, allowing the parachute to expand as applied forces increase. Side ② shows elastic 'bungee cords' connecting the cut in the parachute, which would then extend and allow the parachute to open.

Advantages

- Passive system with no moving parts, decreasing the chance of catastrophic failure
- Simple analysis, allowing for various iterations and longer time for material analysis and selection

Disadvantages

- May affect current parachute performance and flight dynamics

- Potential for an unwanted oscillating system as force fluctuates with speed and parachute diameter
- Lack of experience in material design and parachute fabrication

Rip Stitch Parachute Expansion

This design works using the principle of rip stitches. A rip stitch is a stitch that breaks/comes undone under a specific force. Using this idea, our design consists of a standard parachute with concertina flaps, held in place by rip stitches. The rip stitches break as the parachute force is greater than the stitch force, allowing the design to unfurl and increase in diameter. Below, in the diagram, the starting radius and end radius of the design can be seen. The rip stitches holding the parachute flaps together would be progressively weaker as the inflation force decreases over time and would be appropriately spaced to ensure a specific disreefing rate.

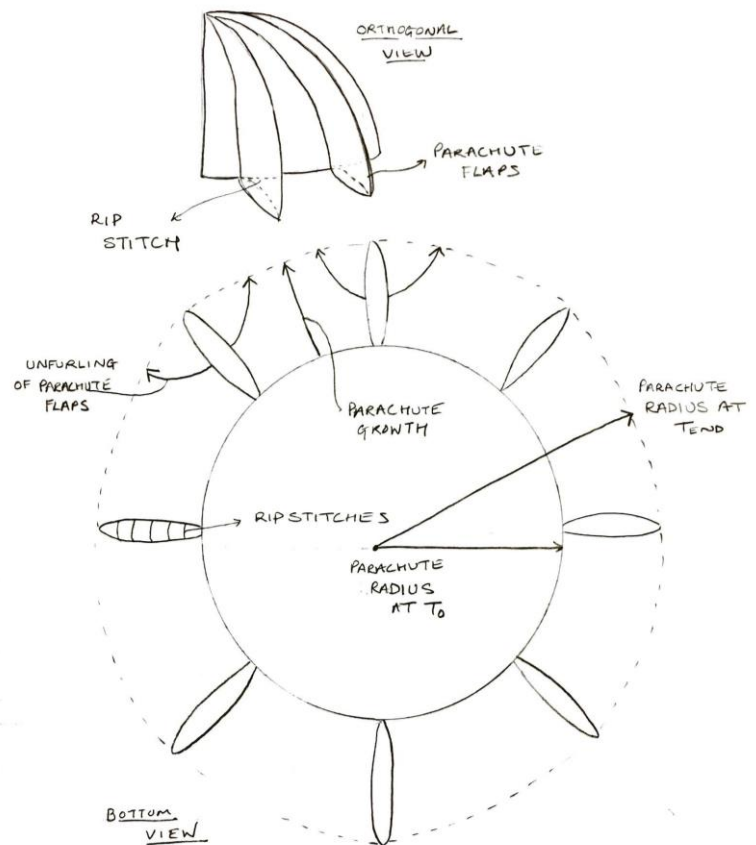


Figure 3.10: Rip Stitch Parachute Design

Advantages

- Passive, no mechanical moving parts
- Can vary the speed of inflation easily by varying the strength of the rip stitches and the distances between them

Disadvantages

- Outward flaps may cause unwanted aerodynamic effects on the parachute
- If the rip stitches do not break simultaneously, the parachute will inflate asymmetrically, causing unwanted lateral movement of the payload and potential failure

High-Altitude Deployment System

This design would rely on the gradient of air density across the upper atmosphere to provide a variable force on a fully deployed parachute system to reduce the deployment impulses on the vessel and parachute system. The key complication in employing this type of system is ensuring adequate deployment and inflation of the chute in the absence of significant atmosphere. Two potential solutions to this are depicted below, the first being a sealed internal section of the parachute that can be filled with gas to maintain shape, and the second being a wireframe to maintain inflation of the parachute much like the frame of an umbrella.

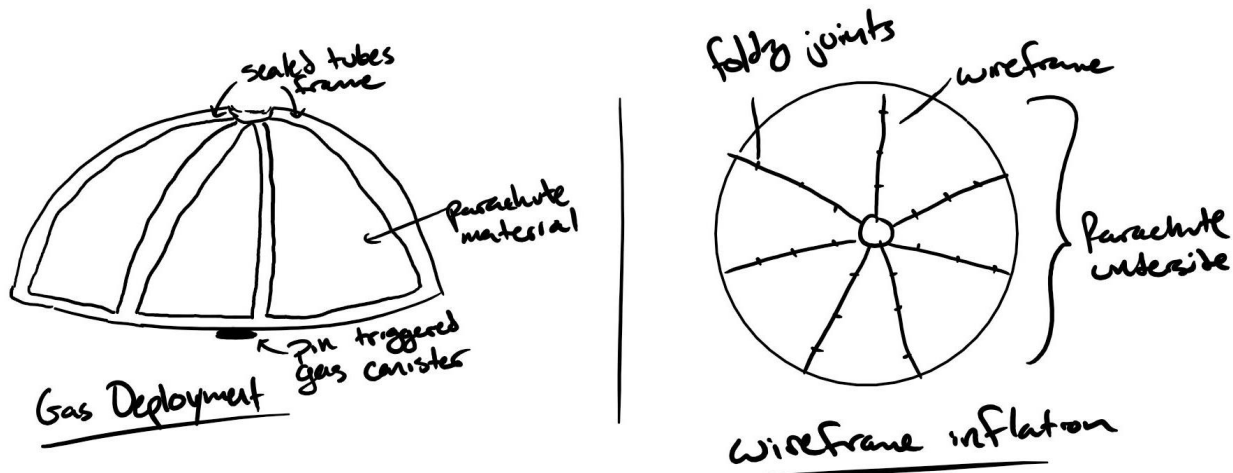


Figure 3.11: High Altitude Deployment Solutions

Advantages

- Requires the least modification of current parachute systems of any proposed design
- Utilizes natural and relatively consistent/predictable phenomena to provide gradient force on the parachute system

Disadvantages

- According to conversations with NASA parachute experts, current parachutes are deployed at lower altitudes to allow the vessel to be slowed naturally by friction with the atmosphere prior to parachute deployment
- Prior deceleration is necessary as parachutes behave erratically at supersonic speeds and trans-sonic travel, making this type of system difficult to analyze

As a result of our conversations with NASA and preliminary system-level analysis, we have chosen not to pursue this particular solution for a few reasons. The first is concerns leveled by our NASA contacts that little data and precedent exists for deploying parachutes at high altitudes while traveling at supersonic speeds. Particularly, when the apparatus enters trans-sonic territory, the parachutes can behave unpredictably, which is concerning for our project. Further, we feel that testing under these conditions will be extremely difficult for our team given our resources. Without being able to adequately test an apparatus under the prescribed conditions, we feel that regardless of the possibility for an optimal solution, we cannot pursue this type of solution.

Mechanical Designs

Eddy Brake

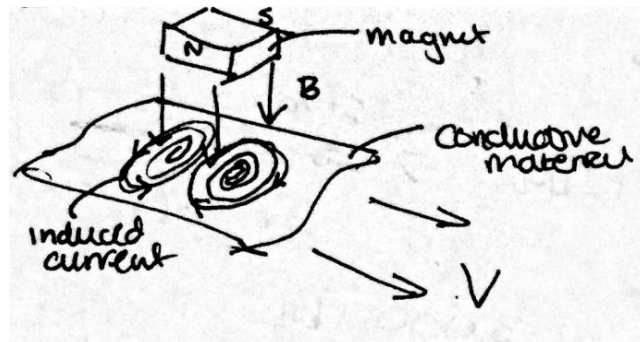


Figure 3.12: Traditional linear eddy brake system

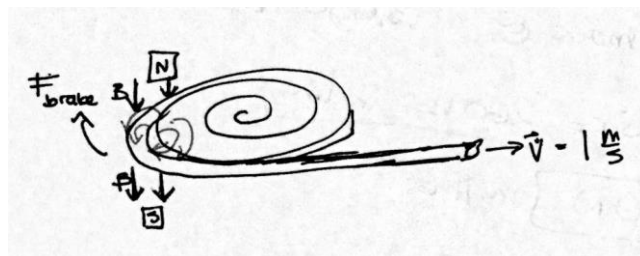


Figure 3.13: Proposed disc-type eddy brake system for unwinding parachute line

An eddy brake is a magnetic braking method that is commonly used in trains and roller coasters. The concept comes from Lorentz's law, which defines the force acting on a particle that passes through a magnetic field. When a conducting material is passed through a magnetic field, the change in magnetic field generates a current inside the moving material, and this current causes a force that resists the movement of magnetic field or, in the case of an eddy brake, the conductive material. One key detail is that resistive force in an eddy brake is proportional to the strength of the magnetic field and the velocity of the material. Figure 8 shows a sketch of a traditional linear eddy brake, and figure 9 shows the disc-type adaptation for a line being released.

Advantages:

- Purely magnetic system, therefore no mechanical wear
- Resistive force proportional to velocity
- Use of permanent magnet means high-integrity, purely mechanical system; optional use of electromagnets means ability to change reefing speed

Disadvantages:

- All power dissipated as heat energy
- Limited by the velocity at which line is being released
- Extremely complex analysis

We decided not to pursue this idea as our calculations showed that it was not feasible. As all of the kinetic energy of the capsule would be turned into heat energy by the eddy brake, we found that we could not build a structure that could handle that degree of heat transfer. As a rough

calculation we found that a capsule slowed from 56 m/s to 5 m/s would raise the temperature of titanium (which we would aim to use) by around 1900K in the short inflation period.

Electrorheological Fluid

Electrorheological fluids are suspensions of fine, non-conducting, electrically active particles in an electrically insulating fluid, which can change apparent viscosity on orders of up to 100,000 in response to electric fields. The material can change from a fluid to the consistency of a gel on the order of milliseconds. ER fluids have been applied to hydraulic valves and clutch and brake systems, with potential use in flexible electronics.

Advantages

- ER fluids are power amplifiers, meaning the mechanical power they can exert is significantly greater than the electrical input power required
- Could be used in tandem with other solutions to create more friction

Disadvantages

- Since Electrorheological fluids are suspensions so simple, ER fluids tend to settle over time. However, this can be mitigated by matching the densities of the solid and liquid components
- Increased viscosity in shear modes is relatively limited in ER fluids
- Requires *active* supply of electric field

We decided not to pursue this idea as there were too many hurdles to overcome for it to be applicable. First, we required an active electric field which would mean batteries or some way of generating electricity in the device. Next, characterizing them looked to be difficult as well as ensuring that they remained in an acceptable state while in the vacuum of space.

Self-Braking Mechanism

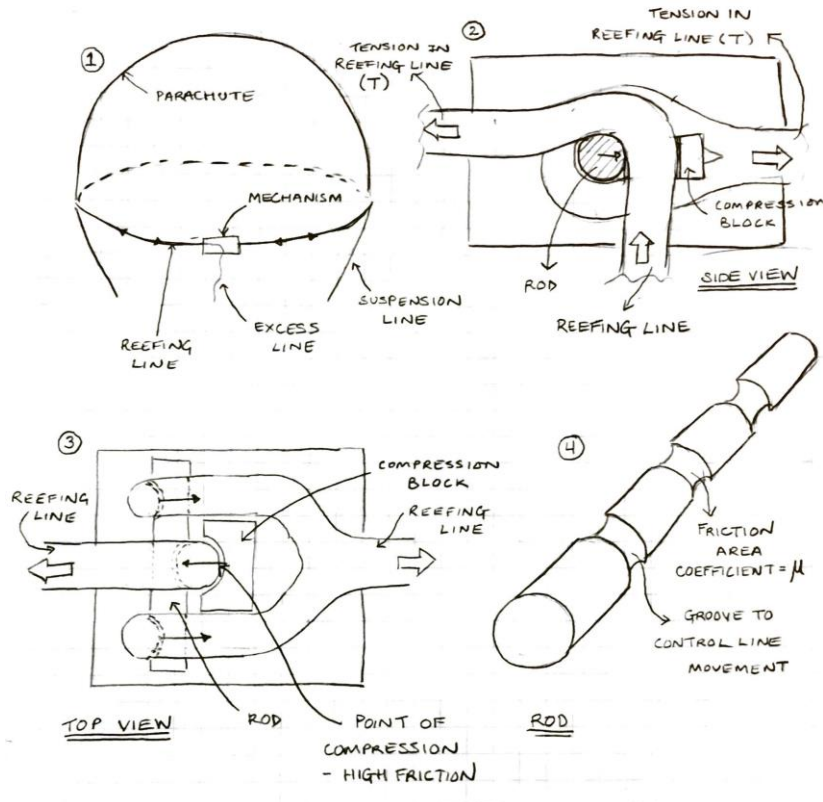


Figure 3.14: Self-Braking Mechanism Design

This idea was motivated by considering the various system requirements presented by the stakeholders. In general, the mechanism would be most effective if it let out reefing line at a non-constant rate. Ideally, it would first let out the line slowly--when the forces would be higher--and then faster--when the forces are lower. However, the tension in the reefing line decreases as the parachute inflates. Therefore, a passive system that applies a constant friction force would allow the reefing line to be pulled out at an equally decreasing rate that is proportional to the tension. We have produced a prototype for such a mechanism to provide proof of concept and tested it to confirm that such a system would be effective in gradually releasing the reefing line. Appendix A includes still frames of a test done on this prototype.

Advantages

- Self-regulating, external feedback is not required
- Force magnitude vs. velocity profile is correct and no alterations need to be made
- Can be put in series with other identical mechanisms to reduce force on each individual mechanism

Disadvantages

- Friction forces produce large amounts of heat which may affect the system in an unwanted manner

- Problems occurring with reefing line would be accentuated as the mechanism forces are based solely on the reefing lines functionality

We decided not to pursue this idea as talks with NASA and our own research found that an entirely passive system would be incredibly difficult to design without knowing the tension in the reefing line exactly. Furthermore, it did not give enough flexibility in off-nominal conditions.

Active and Passive System

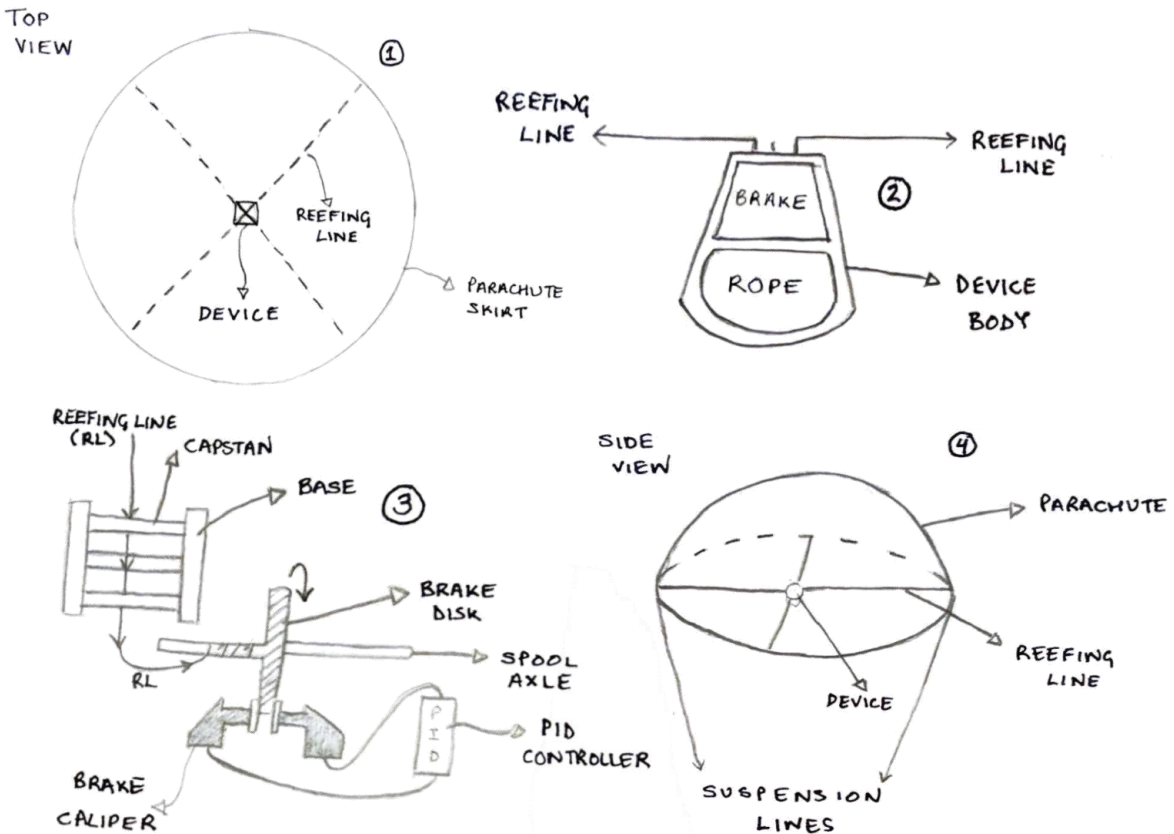


Figure 3.15: Active & Passive Mechanism Design

This idea integrated both passive and active systems to improve reliability and ability to adapt to new situations. By mounting a device in the center of the parachute, held up by the tension in the reefing line, this device would cause perfectly symmetrical inflation as well avoiding the high accelerations seen on the skirt of the parachute. The idea consists of reducing the tension in the reefing line by passing the line through a series of capstans and then controlling the movement of the reefing line using an active brake. This active brake would be controlled by a microcontroller which takes in environmental data (velocity, altitude) to produce a diameter profile which would reduce the force felt by the capsule. Although being bigger than the reefing line cutter, this has the advantage of reduced force as well as being able to adapt well to off nominal cases such as late deployment.

Advantages

- Can very accurately control the growth of the reefing line
- Does not require knowledge of the reefing line tension
- Reduction in possibility of asymmetrical inflation

- Easily adapts to any situation, especially sub-optimal deployment

Disadvantages

- Contains electronics which have the potential to fail
- Mounting in the center of the parachute may have unwanted aerodynamic effects

As a result of this ideation, we decided to go with our active and passive integrated system. This system by combining both active and passive systems gave huge flexibility as well as reducing the reliance on the tension in the reefing line as our design reduces the tension as a percentage rather than a nominal value. Furthermore, by tuning the passive system to reduce the tension in the reefing line by a large percentage, the device has the possibility to work successfully in off-nominal cases where higher forces may be seen (e.g. late deployment, failure of a single chute).

Active Brake

Once we made the decision to use an active system, we began to explore the space of ready-made electronic brakes.

Hydraulic caliper brakes were an obvious first choice - they are popular because of their favorable force transfer and used commonly used in high-force braking systems, such as automobiles. However, as our mechanism is designed for use on aerospace capsules, it can't rely on hydraulics because, during spaceflight, the hydraulic fluid can become compromised.

We were drawn to trailer brakes for their strength and ease-of-use. Trailer brakes are magnetically actuated friction-based drum brakes that mount into the wheel hub of a trailer as it is being towed behind a truck. Installation is simple - notably, the electronic wiring is straightforward. With further research, we found that none of the drum brakes on the market were small enough to fit our system. We also found that these drum brakes often fail by locking, which would be a catastrophic failure for our system - if the parachute spool becomes locked and the parachute isn't allowed to open, the craft won't slow down enough before landing.

We considered U-brakes, the brakes that are mounted about bicycle wheels and actuated by a wire attached to the handle bars. These brakes seemed to have little force advantages, particularly in that in order to brake at a constant force, the user must hold a constant force.

Our system's needs were not served by existing brakes on the market. So, the team developed a design for what we dubbed the 'mechanical caliper brake,' the first servo-powered mechanical power brake of its kind. The caliper-style disc brake uses gears to turn a threaded rod to drive the brake pads closer to the brake disc. The brake has the mechanical advantage of a large moment arm, since the brake force is applied at the outermost part of the disc and the reefing line is never wrapped further than this on the spool. Most significantly, the threads hold the brake pads in place, so the servo only needs to apply force to turn the threads (this contrasts with the U brake, wherein the power source would have to hold the line in tension constantly). The down selection to the mechanical caliper brake can is shown in the table below.

Table 3.1: Downselection table showing mechanical caliper brake as best choice

	Reliability	Current Draw	Doesn't Require a Holding Force	Usable in space?
Drum Brake	Red	Red	Red	Green
Hydraulic Caliper Brake	Green	Red	Red	Red
U Brake	Green	Green	Red	Green
Mechanical Caliper Brake	Green	Green	Green	Green

Final System Design

System Analysis

Constants and Variables

Summary of variables:

Time Dep. Var	Description
$\alpha = \dot{\omega}$	Reefing Line Spindle Angular Acceleration [rad/s ²]
ω	Reefing Line Spindle Angular Velocity [rad/s]
θ	Reefing Line Angular Rotation [rad]
F_b	Braking Normal Force [N]
D_{so}	Spool Outer Diameter [m]
I_{sp}	Spool Rotational Inertia [kgm ²]
I_T	Total Rotational Inertia [kgm ²]
T_s	Servo Torque [Nm]

Summary of Known and Experimentally Determined Constants:

Constant	Description	Value
T_{RL}	Nominal Reefing Line Tension [N]	2669
T_{red}	Capstan Reduced Reefing Line Tension [N]	
μ_c	Capstan Friction Coefficient [-]	0.242
ϕ	Capstan Wrap Angle [rad]	9.515
R_{br}	Brake Mounting Radius [m]	0.1016
μ_{br}	Brake Coefficient of Friction [-]	0.3
K	Nut Factor [-]	0.15
M_{be}	Bearing Frictional Moment [Nm]	0.0860
d_{be}	Bearing Viscous Damping Coefficient	
D_{th}	Threaded Diameter [m]	0.0064
D_{si}	Spool Internal Diameter [m]	0.0190
L_s	Spool Length [m]	0.1778
ρ_{RL}	Reefing Line Density [kg/m ³]	760
I_{sh}	Shaft Rotational Inertia [kgm ²]	4.14E-04
I_d	Disk Rotational Inertia [kgm ²]	9.14E-04

The overall Daedalus system is made up of several interacting subsystems. Each of the components in these subsystems work together in order to achieve the overall goal of continuously disreefing parachutes during capsule re-entry. Below you can see a simplified diagram with the main components listed (Figure 3.18). The main subsystems described in this section will be referred to as the passive system (capstans and bearing), active system (brake) and the spindle (brake disc, needle bearing, spindle shaft and spool of reefing line). The physics of each of these mechanisms is discussed in further depth. The dynamics of the mechanism is driven by the moment balance exhibited below (Figure 3.19).

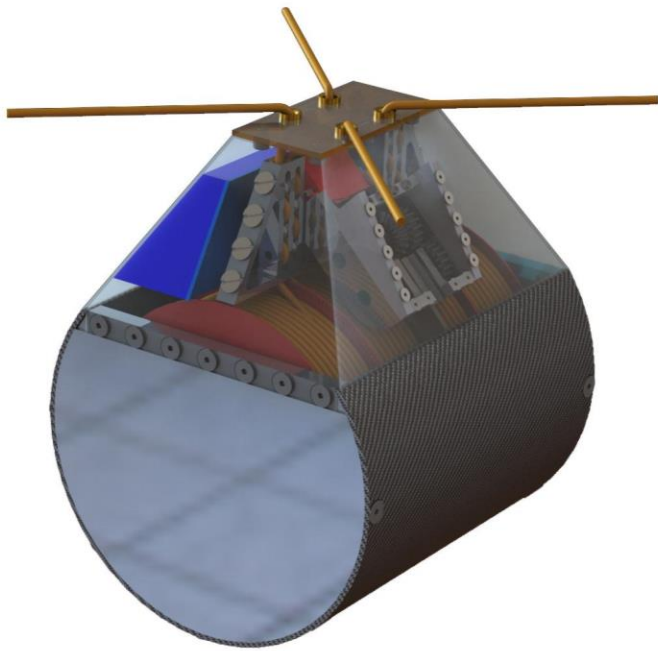


Figure 3.16: Assembly Iso View Render

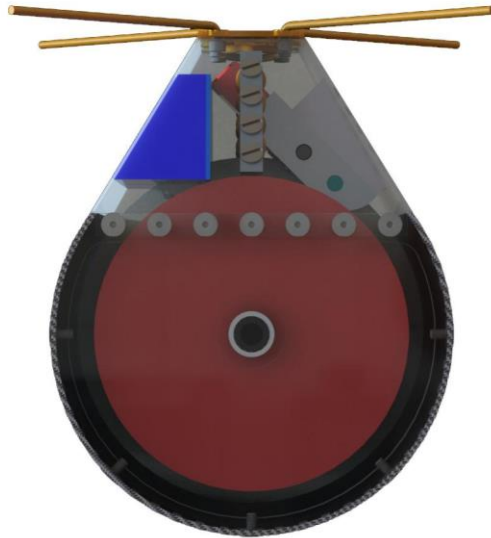


Figure 3.17: Assembly Side View Render with Clear Wall for clarity

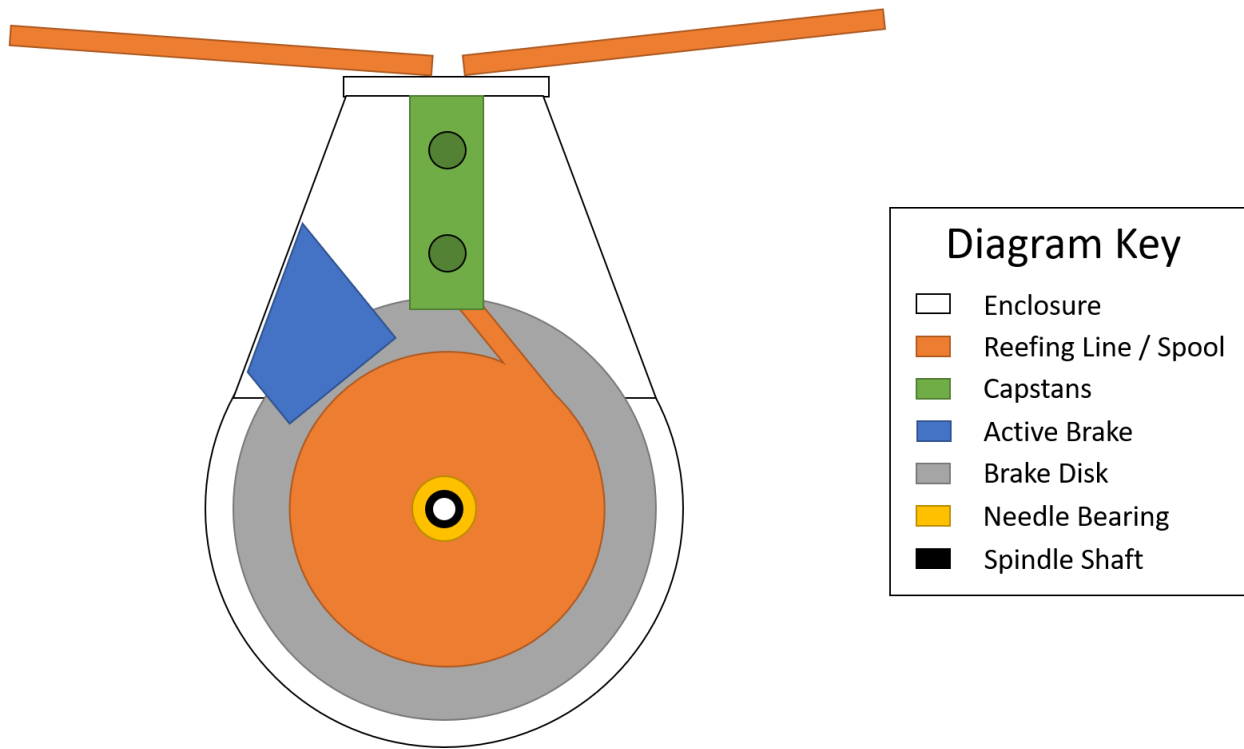


Figure 3.18: Simplified Diagram of System Components

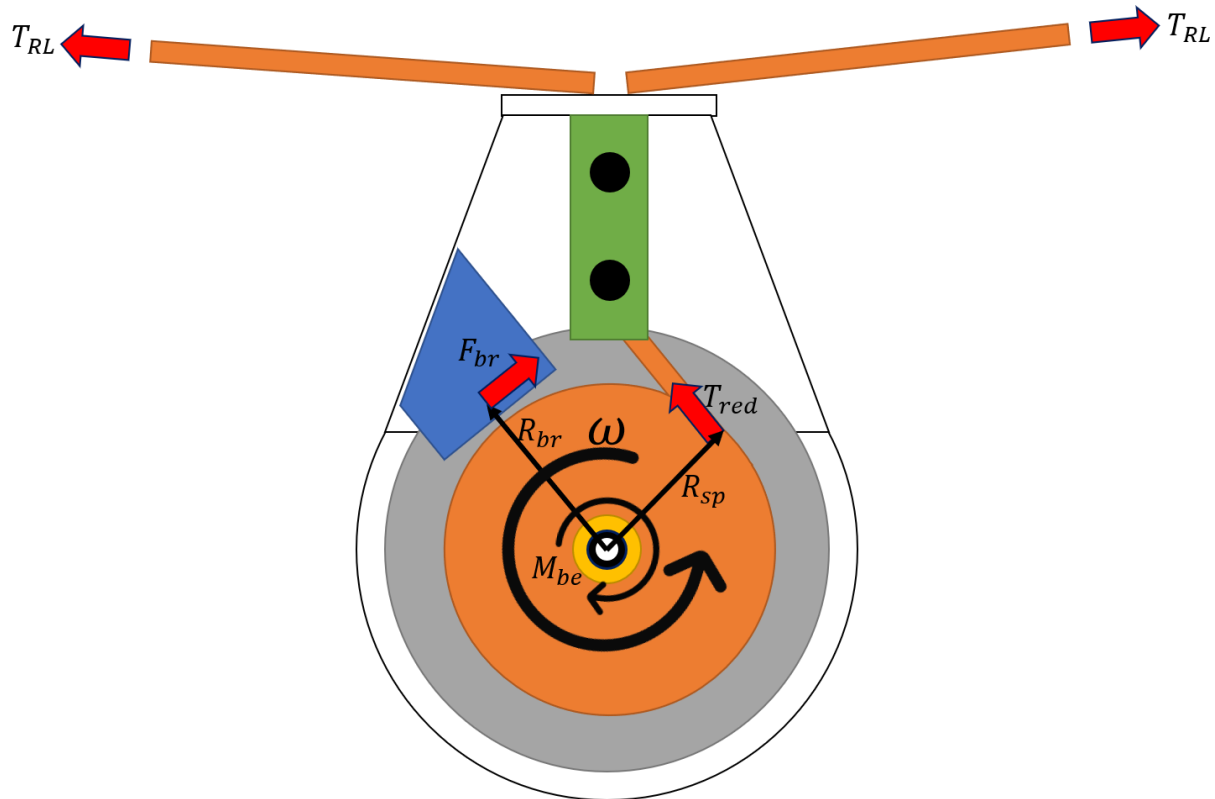


Figure 3.19: Simplified moment balance with forces acting on system

Passive Braking Subsystem

This gives rise to the following Moment Balance equation, where I_T is the mass moment of the system, and α is the acceleration, D_{so} is the diameter of the outer spool, T_{RL} is the tension in the reefing line, μ is the coefficient of friction between the rope and the capstan, ϕ is the wrap angle, T_s is the servo torque, M_{be} is the bearing frictional moment, K is the nut factor, D_{th} is the threaded diameter, μ_{br} is the brake coefficient of friction, R_{br} is the brake mounting radius, ω is the reefing line spindle angular velocity, and d_{be} is the bearing damping coefficient.

$$\Sigma M = I_T \alpha = \frac{T_{RL} D_{so}}{e^{\mu\phi} 2} - \frac{T_s}{KD_{th}} \mu_{br} R_{br} - M_{be} sgn(\omega) - d_{be} \omega \quad (16)$$

$$\Sigma M = I_T \alpha = \frac{T_{RL} D_{so}}{e^{\mu\phi} 2} - F_{br} \mu_{br} R_{br} - d_{be} \omega - M_{be} \quad (17)$$

This section will further dissect this equation and explain the individual components.

Passive Brake - Capstans

Capstans are useful mechanical devices and their friction behavior is relatively well understood. In its most simple form the capstan equation can be stated as:

$$T_{Load} = T_{Hold} e^{\mu\phi} \quad (18)$$

where μ is the coefficient of friction between the capstan surface and the rope and ϕ is the capstan wrap-angle as shown below.

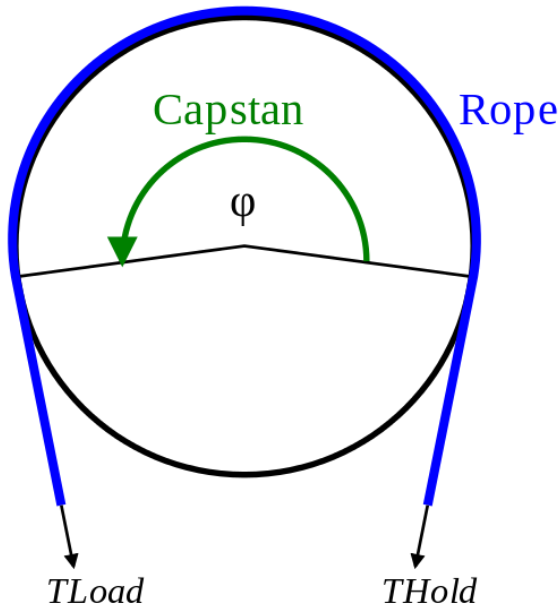


Figure 3.20: Basic Capstan Characteristics

The capstans are the principal components of our passive braking system. The two main capstans are composed of press-fit aluminum rods into triangular aluminum blocks. The reefing line wraps around these rods to obtain the desired effect. Additionally, there are capstan-type interactions at the entrance and exit of the capstans as well as on the brass guides in the top plate. These surfaces are all curved so as to better simulate a typical capstan and increase the

force reduction effect by adding wrap angles. These numerous angles were all factored into our calculations. Below, the image depicts a Solidworks sample of our capstans with the angles measurement around the aluminum rods displayed.

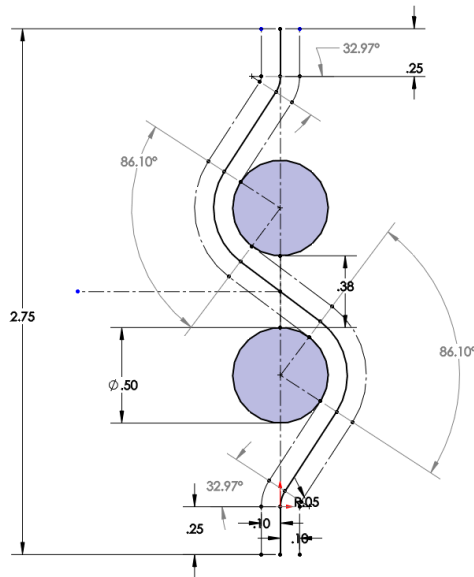


Figure 3.21: Aluminum rods wrap angles

The coefficient of friction (μ) between the Kevlar reefing line and aluminum, was determined experimentally through a series of tests described further on. In these experiments, we calculated an average μ value of approximately 0.24. Accounting for measurement inaccuracies of the machine used for testing, we estimated the true value to lie between 0.22 and 0.26. Since our goal force reduction between T_{Hold} and T_{Load} was 87.5 percent (a ratio of 8:1), we calculated the necessary wrap angle to be 493 degrees.

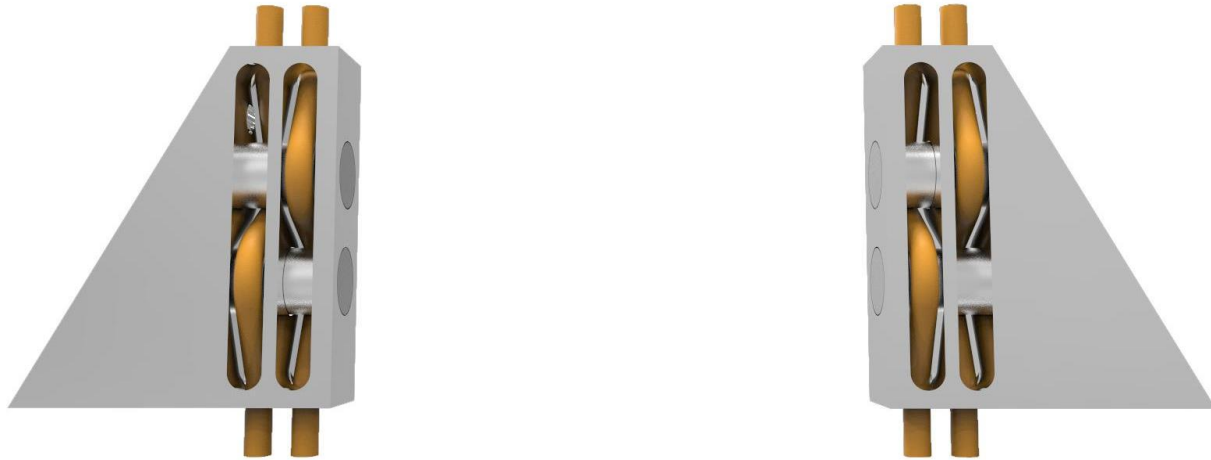


Figure 3.22: Capstan Renders

Through further empirical testing of our capstan assembly, we determined that our force reduction was approximately 10 times, which falls within our original confidence interval. With our specific set-up in mind, our capstan equation can be written as:

$$T_{RL} = e^{\mu\phi} T_{Red} \quad (19)$$

Or more usefully:

$$T_{red} = \frac{T_{RL}}{e^{\mu\phi}} \quad (20)$$

This reduced tension is applied along the reefing line to the spool at its current outer radius ($R_{sp} = \frac{D_{so}}{2}$). Thus, the moment applied the spool can be written as:

$$M_{capstan} = \frac{T_{RL}}{e^{\mu\phi}} \frac{D_{so}}{2} \quad (21)$$

Passive Brake - Bearings

The second component of our passive braking system is the needle roller bearings. The primary function of the gears is to hold the spindle shaft concentrically as it unwinds and releases reefing line to the parachute. However, it performs a small, but non-negligible function as it adds to the passive braking of the mechanism.

Bearing friction is not constant and depends on certain tribological phenomena that occur in the lubricant between the rolling elements, raceways, and cages. In our case we assume that these can be modeled by two primary forces on the system: a constant frictional moment that acts in the opposing direction to the current rotation ($M_{be} sgn(\omega)$) and a damping force dependant on the angular velocity of the rotating shaft. The frictional moment is independent of any other variables in the system. We determined an approximate value for this friction moment experimentally. The damping force is not a constant value. The bearing applies damping to the shaft rotation proportional to and opposite in direction of the rotational speed of the shaft ($d_{be}\omega$). Without a sensitive torque sensor, it was not possible to obtain this value experimentally, so we estimated it based on values of similar bearings. In summary, the moment applied by the bearings can be represented in our overall equation:

$$M_{bearing} = M_{be} sgn(\omega) + d_{be}\omega \quad (22)$$

Electronic Active Brake

Our active brake system uses a high torque servo and gear train to thread rods, applying a normal force to a brake pad that engages with the rotating brake disc.

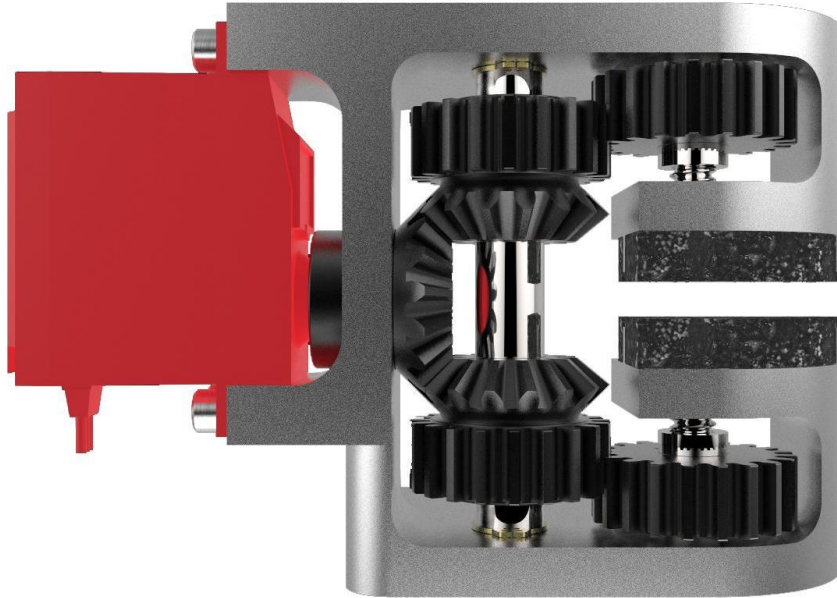


Figure 3.23: Active Brake Assembly Render

Once the position is commanded, the servo moves to this position with an applied torque. This torque is transferred through the gear train at a constant ratio to the threaded the rod. The rod is threaded, and its resulting normal force can be calculated. The bolt preload equation states:

$$T = PKD \quad (23)$$

where T is torque, P is the normal force, K is the nut factor (a dimensionless friction coefficient) and D is the diameter of the bolt. We can rearrange this to find the normal braking force:

$$F_{br} = \frac{T_s}{KD_{th}} \quad (24)$$

This is critical because the servo torque is a limiting parameter (dependent on the servo model). Therefore, there is a maximum normal force that our friction brake can apply. Given the system parameters (listed above), this maximum braking normal force is approximately 1000 lbf.

The normal force is applied through a brake pad to the brake disc. Experimentally, we determined that the coefficient of friction between these two surfaces (μ_{br}) is approximately 0.3.

This braking force is applied at a constant radius that is determined by the design of our mechanism. In summary, the brake applies a moment to our system dened as below:

$$M_{brake} = F_{br} \mu_{br} R_{br} = \frac{T_s}{KD_{th}} \mu_{br} R_{br} \quad (25)$$

Spool (System Inertia)

The moment of inertia of a rigid body, otherwise known as the angular mass or rotational inertia, is a tensor that determines the torque needed for a desired angular acceleration about a

rotational axis. It depends on the body's mass distribution and the axis chosen, with larger moments requiring more torque to change the body's rotation.

Every moving part in our system has a mass moment of inertia associated with it. The 3 moving components in this case are the shaft, brake disc, and the reefing-line spool and the total inertia is the sum of these 3. The values for the shaft and brake disc are constant and were extracted directly from SolidWorks. However, the rope spool does not have a constant value. This is because, as the reefing line is let out, the amount of rope remaining on the spool decreases. We can approximate the spool as a thick-walled cylindrical body as shown in the image below. The moment of inertia of this shape can be written as:

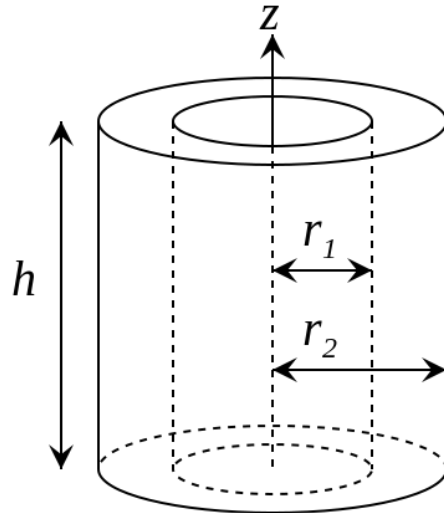


Figure 3.24: Hollow Cylinder Basic Parameter Definitions

The moment of inertia of this shape can be written as:

$$I_z = \frac{1}{2}m(r_2^2 + r_1^2) \quad (26)$$

We can also calculate the mass of this shape quite simply:

$$m = \rho V = \rho h \pi (r_2^2 - r_1^2) \quad (27)$$

And therefore, the total moment of inertia can be written as:

$$I_z = \frac{1}{2}\rho h \pi (r_2^4 - r_1^4) \quad (28)$$

In our case $\rho = \rho_{rope}$ and r_2 is the only value that is non-constant.

$$r_2 = \frac{D_{so}}{2} \quad (29)$$

Through our calculations, we determined exactly how the outer spool radius changes as a function of line-let-out, which we then accounted for in the simulation.

In summary, the total inertia of our system can be defined as:

$$I_T = I_{sp} + I_{sh} + I_d \quad (30)$$

Enclosure

Our enclosure itself did not have an effect on the overall moment and force balance of the system however it still required basic force analysis to make sure it could withstand the overall forces on the system.

Summary

Our overall system is defined by the balance of moments in our system. Namely:

$$\Sigma M = I_T \alpha = M_{capstan} - M_{bearing} - M_{brake} \quad (31)$$

Or written out fully:

$$\Sigma M = I_T \alpha = \frac{T_{RL} D_{so}}{e^{\mu\phi} 2} - \frac{T_s}{KD_{th}} \mu_{br} R_{br} - M_{be} sgn(\omega) - d_{be} \omega \quad (16)$$

Design

Active

Our active brake system uses a high torque servo and gear train to thread rods, applying a normal force to a brake pad that engages with the rotating brake disc. The speed at which the reefing line is let out of the mechanism is determined by the speed at which the spool rotates, which is controlled by how much normal force is applied to the brake disc by the brake.

The brake is actuated by a high torque servo. By using a series of miter and straight gears, we were able to use a single motor to apply linear force on both sides of the brake pad uniformly. The servo turns a series of gears, as indicated in the figure below. The servo shaft interfaces with the principal bevel gear (1). This principal gear interfaces with two coaxial bevel gears (2) which have been modified and mounted to spur gears. The spur gears, turning at the rate of the secondary bevel gears, turn a secondary set of spur gears (3), which are fixed to a threaded rod. As the gears turn, the rod moves through the threaded mount of the caliper brake housing, pushing the brake pads (4) into contact with the disc, thus increasing the brake force, or pulling them out of contact with the brake pad, releasing the brake.

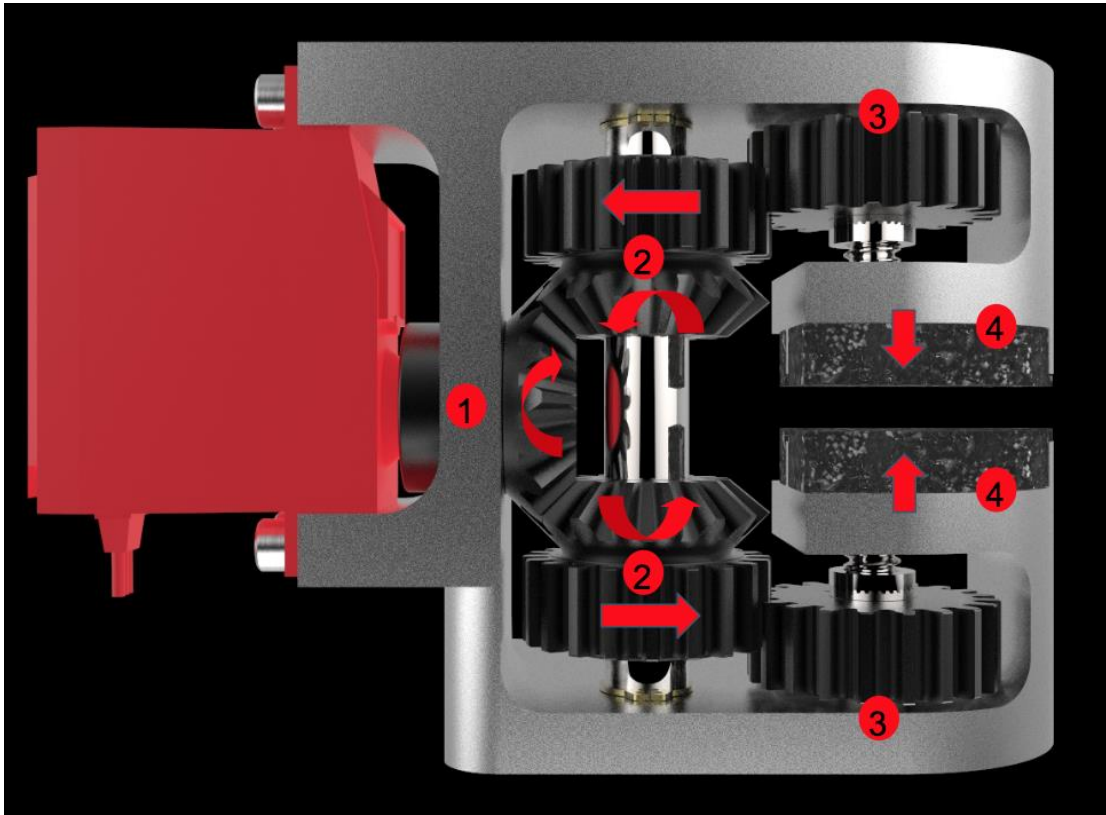


Figure 3.25: Gearbox Render

The servo is controlled by the microcontroller, which calculates whether more or less braking force is needed to drive the system toward the ideal (explained in the upcoming sections) and commands the corresponding servo position. Once the position is commanded, the servo moves to this position with an applied torque. As discussed above, this torque is transferred through the gear train at a constant ratio to the threaded rod. The threaded rod then applies a normal force on the brake disc through the brake pads. Experimentally, we determined that the coefficient of friction between these two surfaces (μ_{br}) is approximately 0.3. Figure 3.26 shows the brake pad design. They were designed to slide into the brake housing but also to minimize the lateral travel during use. We wanted the pads to have maximum possible contact with the brake disc without interfering with the rope on the spool. The brake pad material is standard clutch lining, purchased from McMaster and milled into the appropriate shape. This braking force is applied at a constant radius that is determined by the design of our mechanism.

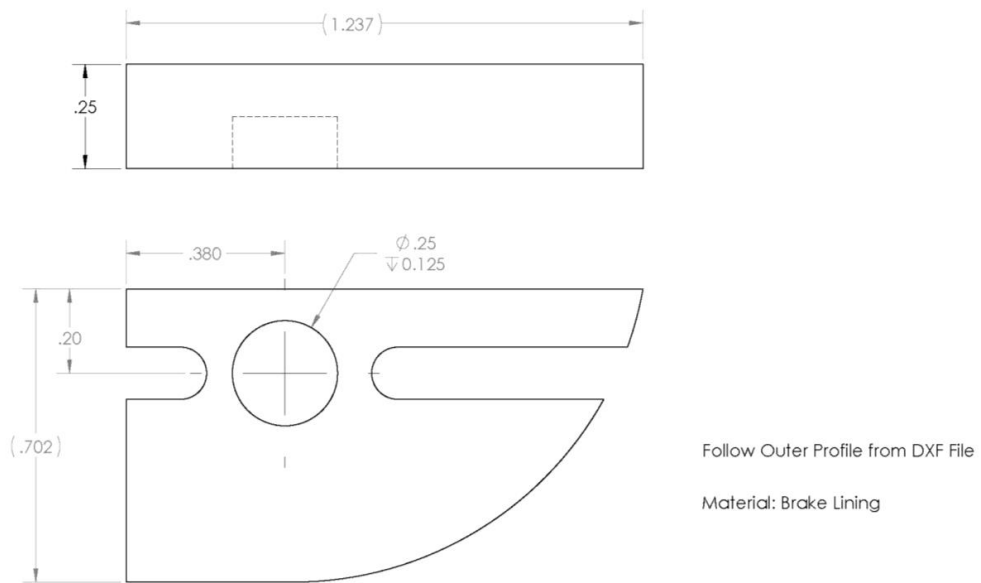


Figure 3.26: Brake Pad Design

The housing of the active brake was the primary design feat. It was intended to minimize the size of the whole active braking system, while still applying the necessary torque and precision that the system calls for. The brake housing is mounted directly to the outermost wall of the mechanism.

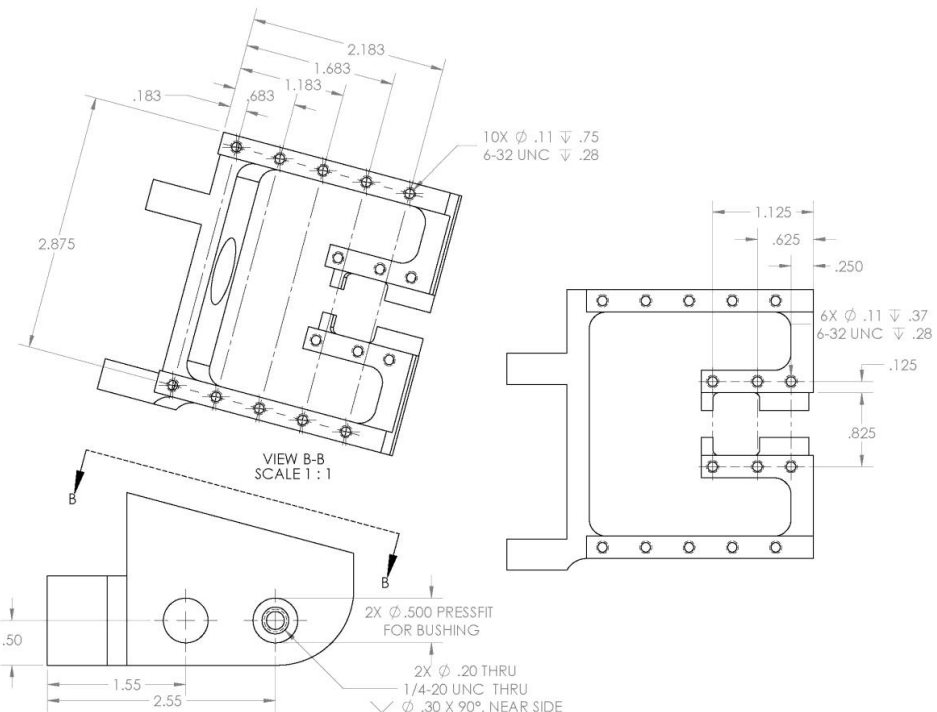


Figure 3.27: Active Brake Housing

The design required that we modify gears to fit our needs. We wanted to minimize the size of the whole brake housing, but the spur and bevel gears are manufactured with a mounting piece on the back side of the gear, about 0.5" long. The box was designed such that we cut off these

back-end pieces. Additionally, we needed the miter and bevel gears (number 2 in Figure 3.25) to turn together, so the gears were welded together. Finally, in order to make the secondary spur gears (number 3 in Figure 3.25) turn the threaded shaft, we used a keyed shaft and keyed gears to ensure perfect torque transfer.

Below is the design for the threaded shaft (excluding the key), which served to mount the secondary spur gears and apply pressure to the brake disc through the brake pads.

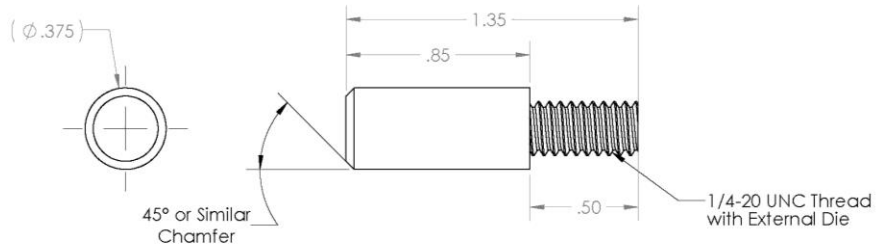


Figure 3.28: Threaded Shaft Design

The coaxial bevel gears were mounted to a shared shaft with a slip fit and was designed to be held in place with retaining rings, since the two gears would turn in opposite direction. However, during the assembly process, it became clear that retaining rings would not work as the tool needed to place the retaining rings required too much clearance, so aluminum spacers were machined to fit the same purpose.

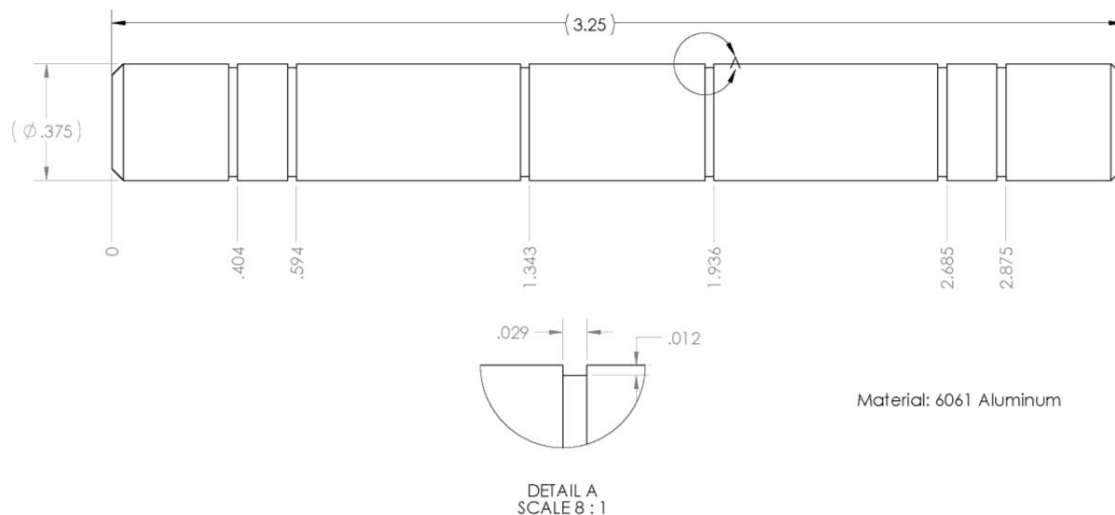


Figure 3.29: Coaxial Bevel Gear Shaft

Although the render doesn't show this, the two sides of the brake that house the brake pads are attached by a 0.25" aluminum sheet in the mechanism to prevent the housing from bowing outward and allowing the wheel to slip through the brake.

Passive (Capstans and Top Plate)

When designing the capstan system and top plate we went through several iterations of design. We had several design challenges that were clear from the beginning:

- Keep the wrap angle as constant as possible during the disreefing process
- Wrap angle should be consistent for all four of the reefing lines
- Ropes are kept separate to eliminate chances of tangling during operation
- Limit any sharp corners in the design as these can damage and fray the rope
- Make overall design as compact and lightweight as possible
- Symmetric design about the main planes of the entire device

Given this list of requirements, careful consideration was given to the arrangement of the capstans in the overall system design.

Top Plate

The top plate that feeds out the rope to the skirt of the parachute was designed to conform with sub-system requirements. The top plate distributes the rope from our device in a square configuration, as this ensures that there are no moments on the top of our structure causing it to twist during operation. The simplified version of our ultimate top plate design can be seen below in figure 3.30.

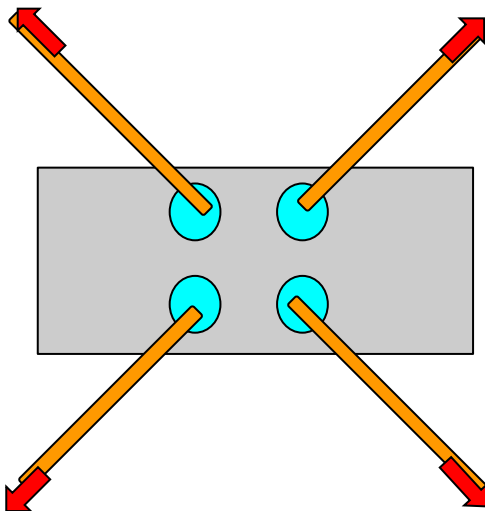


Figure 3.30: Simplified Final Top Plate Design (TOP VIEW)

This design was chosen over several other iterations, including putting the top holes in a single line (which would have made the transition from the spool and capstans far easier but would have introduced unwanted moments on the overall system) and a single hole (which could have possibly led to the ropes fraying each other and/or getting tangled).

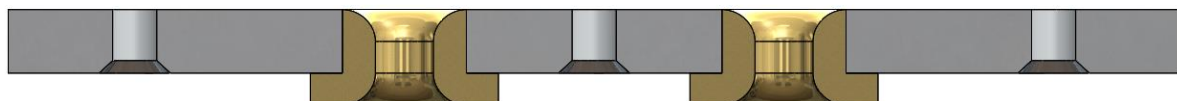


Figure 3.31: Cross section of Top Plate Assembly

The final top plate design incorporated brass inserts that were press-fit into the aluminum base plate. We chose to make these inserts out of brass due to its ease of machinability and higher strength, as these inserts are the actual parts that would experience the shear forces from the rope. The top plate was designed to be made of aluminum because it is lightweight and readily available. It also included several threaded holes to facilitate attaching the plate to the enclosure frame.

Capstans

Subsequently, we finalized the design and positioning of the capstans in the larger assembly so that they would be in between the spool and the top plate to reduce the tension force experienced by the spool.

Several design iteration were worked through including having single bars run across the length of the device for the rope to run around. For the final design, rather than having the rope wrap around a single bar multiple times to create this capstan friction, we developed our capstans so that the rope would wrap around multiple bars in series. This ensured that there was less of an overall lateral force on the bars from the ropes, having the net force cancel out entirely.

Given the overall layout of the various components in our system, we found it best to have two separate capstan sections for each half of the spool to comply with our previously listed requirements. The first iteration of our capstans was designed out of a single piece of machined aluminum. It consisted of complex geometry but was contoured to the entire rope along its entire length. However, the rope turned out to be slightly larger than the quoted diameter, making it impossible to feed through the capstan as designed, forcing us to redesign and remanufacture this subsystem.

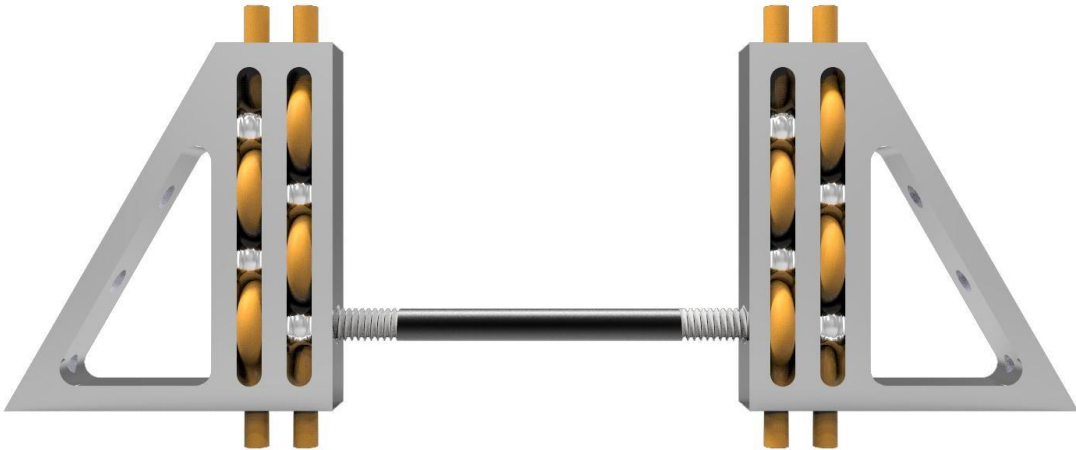
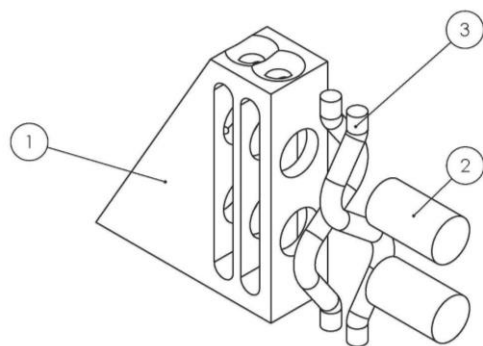


Figure 3.32: Original Capstan Assembly Design

In the subsequent iteration, we simplified the capstan design so that it could be made of a mounting block and press-fit aluminum rods. This provided ease of machinability while providing the same function as our previous iteration.



Figure 3.33: Updated Capstan Assembly Design

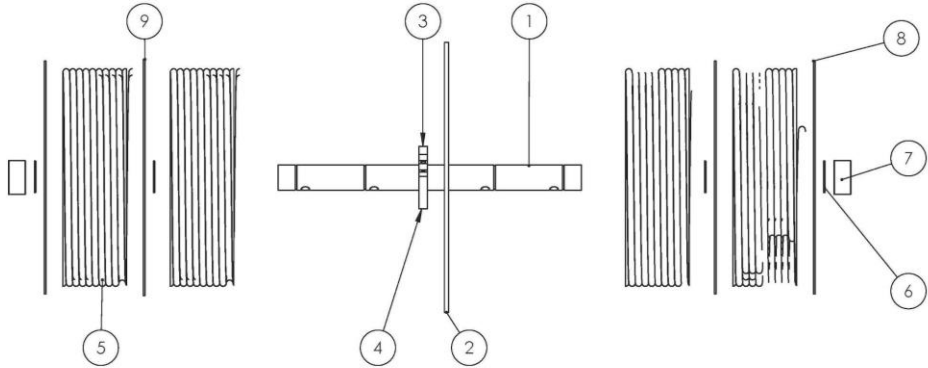


ITEM NO.	DWG NO.	DESCRIPTION	QTY.
1	2.2	Capstan Mounting Block	1
2	2.3	Capstan Rod	2
3	NA	Dummy Rope	2

Figure 3.34: Final Capstan Design

Spool

In designing the spool system, the primary size constraint came from the amount of rope that the spool must hold. Given a nominal diameter of $3/16"$ and a length of 600 ft, we used an excel spreadsheet to determine the length and radius of a cylinder containing that volume of rope. Playing with the two parameters reached a length of eight inches and a radius of four inches, as this would create the most symmetrical volume possible. This resulted in the configuration shown in figure 3.35 below.



ITEM NO.	DWG NO.	DESCRIPTION	QTY.
1	3.1	Spindle Shaft	1
2	3.2	Brake Disk	1
3	3.3	Disc Mounting A	1
4	3.4	Disc Mounting B	1
5	NA	Rope Spool	4
6	NA	Retaining Ring (91590A128_grv)	4
7	NA	Needle Roller Bearing (5905K26)	2
8	NA	Spacer	3
9	NA	Spacer - Encoder Mod	1

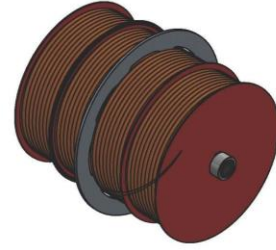


Figure 3.35: Spindle Subassembly

A Spindle shaft outer diameter of $\frac{3}{4}$ " was chosen to match available needle-roller bearings. The core of the rod was partially hollowed by a $\frac{1}{2}$ " drill to remove mass, since a hollow rod of $\frac{1}{8}$ " thickness was shown to be capable of withstanding the expected loading torque. The entire rod could not be made hollow as part of the shaft had to be keyed to mate with the brake disc coupler. This shaft was designed with four through holes into which rope would be fed to ensure perfect torque transfer between the shaft and the coiled rope, along with ease of assembly. Further, four retaining ring slots were added that would be used to aid in locating the ABS spacers. We chose ABS for the spacers as they needed to be as thin as possible while not failing under the large expected RPMs, which ABS satisfied with a tensile yield stress of 1000 psi. Further, one of the ABS spacers could be cut with slits to be utilized as an integrated encoder wheel, meeting the size specifications of our off-the-shelf encoder.

The next major component in the spindle assembly was the brake disc itself. We designed using $\frac{1}{8}$ " aluminum sheet as this would reduce mass and is the most commonly used thickness for commercial brake discs. The brake disc was custom designed based from a Shimano bike brake design, as no commercial brakes were designed for the eight-inch diameter required of our braking system. The brake disc had multiple internal geometries removed in order to reduce weight and inertia of the disc. The brake disc was designed to be loaded in only one direction, as the spindle will never rotate in the opposite direction, so these thin arms would only ever be loaded in tension. FEA analysis was conducted to ensure that these arms would not fail under expected loading.

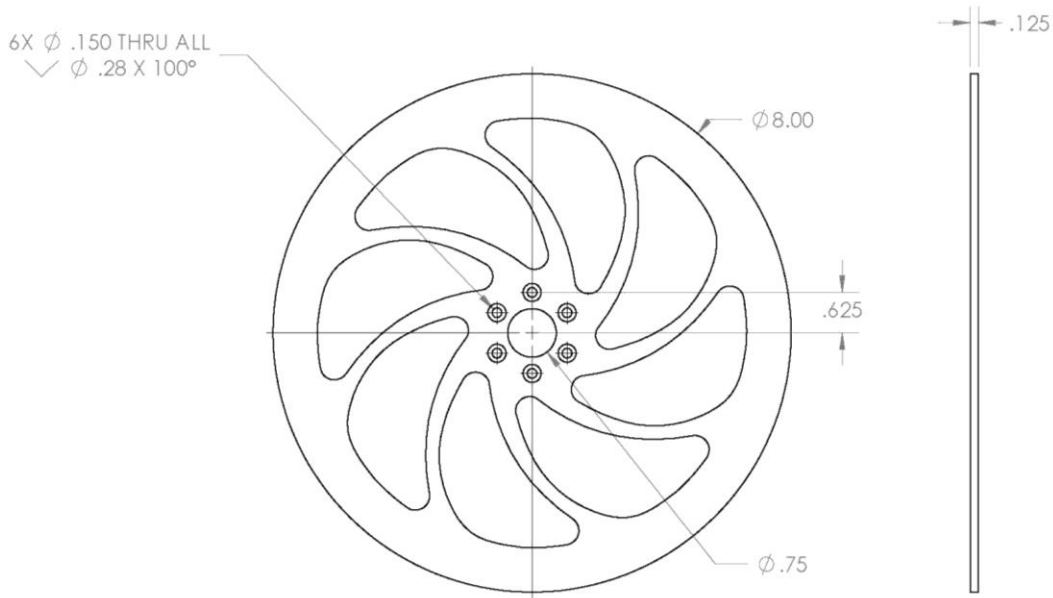


Figure 3.36: Brake Disc

In order to ensure perfect torque transfer between the disc and the shaft, a two-part hub was designed to interface with the D-slot on the Spindle Shaft. This hub mounts to the brake disc using a traditional hex bolt pattern at a radius of $\frac{5}{8}$ ". The hub is designed in two parts to allow for ease of assembly and to allow fasteners to tighten the hub edges around the edge of the D-slot to reduce any potential play in the cut. A D-slot was used rather than a pin or set screw in order to reduce the required thickness of the hub, as every inch was needed to contain the rope. The manufacturing of the hub will be discussed in the below section.

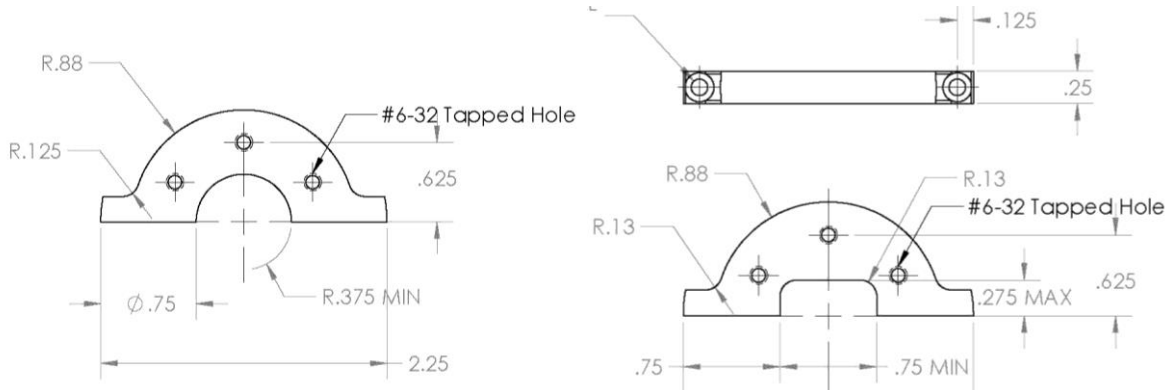


Figure 3.37: Brake disc Hub

Enclosure

The enclosure design had to meet several criteria as laid out by the overall design requirements. These criteria are as follows:

- Design should be as compact and lightweight as possible
- Design should be symmetrical across major device planes to ensure no uneven moments and forces

- Design should be aerodynamic in profile facing the oncoming air to limit any chance that the device might have been turned over during operation
- Design must be able to withstand all reaction forces from internal system mechanics

Considering the geometry of the spool and its volume, which could not be further reduced, we developed the overall shape of the mechanism's enclosure around this configuration.

Additionally, this enclosure had to attach to the top plate we had developed that would provide for the optimal force reduction through the capstans. Thus, our final enclosure design is as follows:

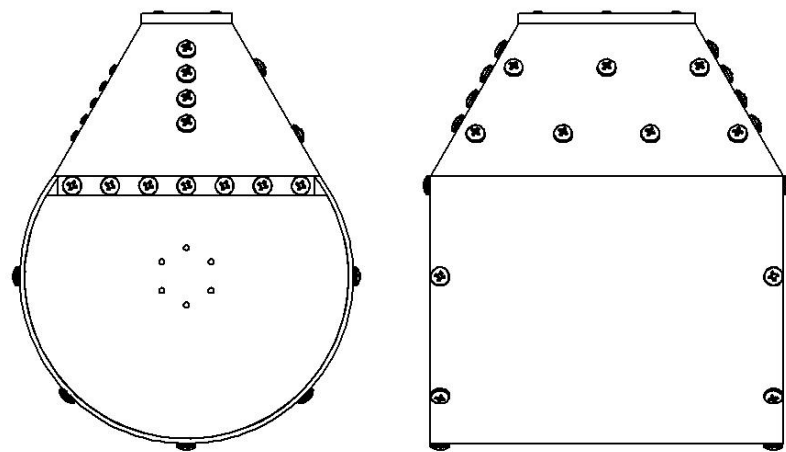


Figure 3.38: Side and Front View of Final Enclosure Profiles

The enclosure was designed out of several connecting parts. The two side walls were designed so that they could have the spool bearings press-fit into place. Because this is where the majority of the force would be seen (constant upwards force), these were machined out of solid pieces of aluminum and its inside faces hollowed out in order to save mass where stress would be lower.

Connecting to these two side walls was the top enclosure piece. This was designed in the pyramid style shape in order to ensure that it would retain the symmetrical requirement and also provide flat surfaces in order for us to mount the active and passive braking systems. This top enclosure piece also attaches to the top plate with threaded bolts. It was designed to survive the reaction forces from these mounted components.

The last piece of the enclosure subassembly is the round shell connecting the round surfaces of the side wall. While this piece is not under much physical stress, it is required to keep the side walls concentric as well as close the volume of our spool. Additionally, it provides the required aerodynamic shape. This part is attached to the walls with threaded screws.

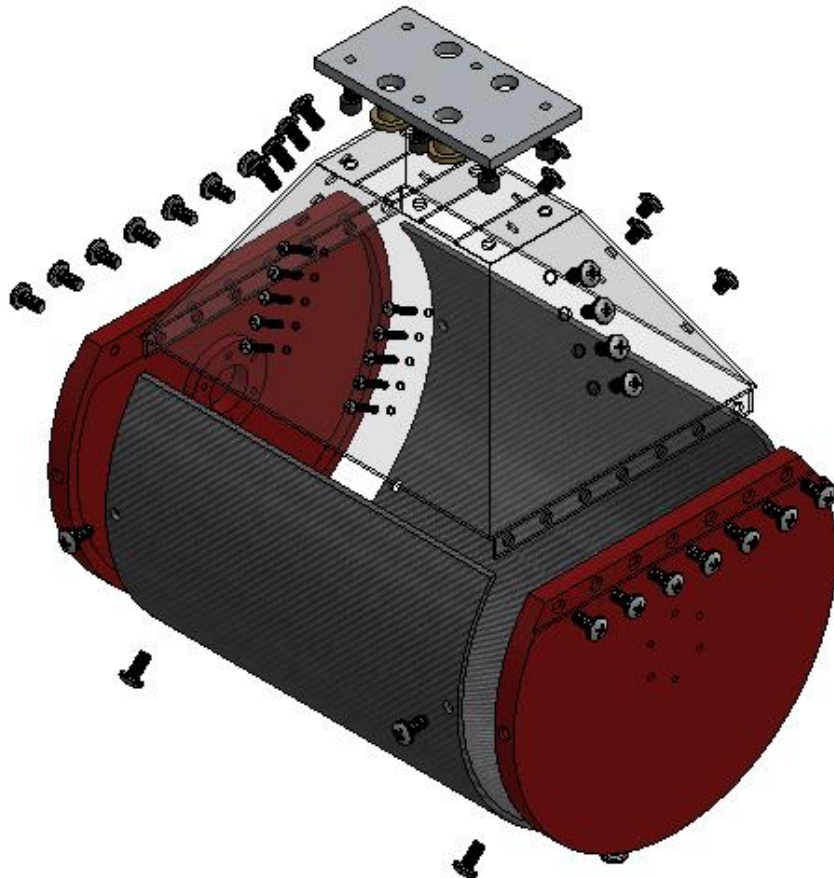


Figure 3.39: Enclosure Exploded View

Electronics and Control System

In order to achieve success, it was imperative to ensure total control of the reefing line, which was managed through the use of precision electronics. The electronics were designed to allow precision control of the gear box and thus the rate of deployment of the reefing line. Overall, our system comprises of a quadrature optical encoder, a high torque servo, and a microcontroller. Below is a list of the exact components that were used:

- **Servo Motor:** HS-7980TH Mega Torque HV Coreless Titanium Gear Servo
- **Microcontroller:** Arduino UNO
- **Optical Encoder:** Broadcom AEDT-9810-Z00 Optical Encoder

Electronics

The electronics system was designed to be lightweight and compact. The simple connections between the components made the assembly straightforward and debugging issues simple. Below is a diagram of the connections between the components:

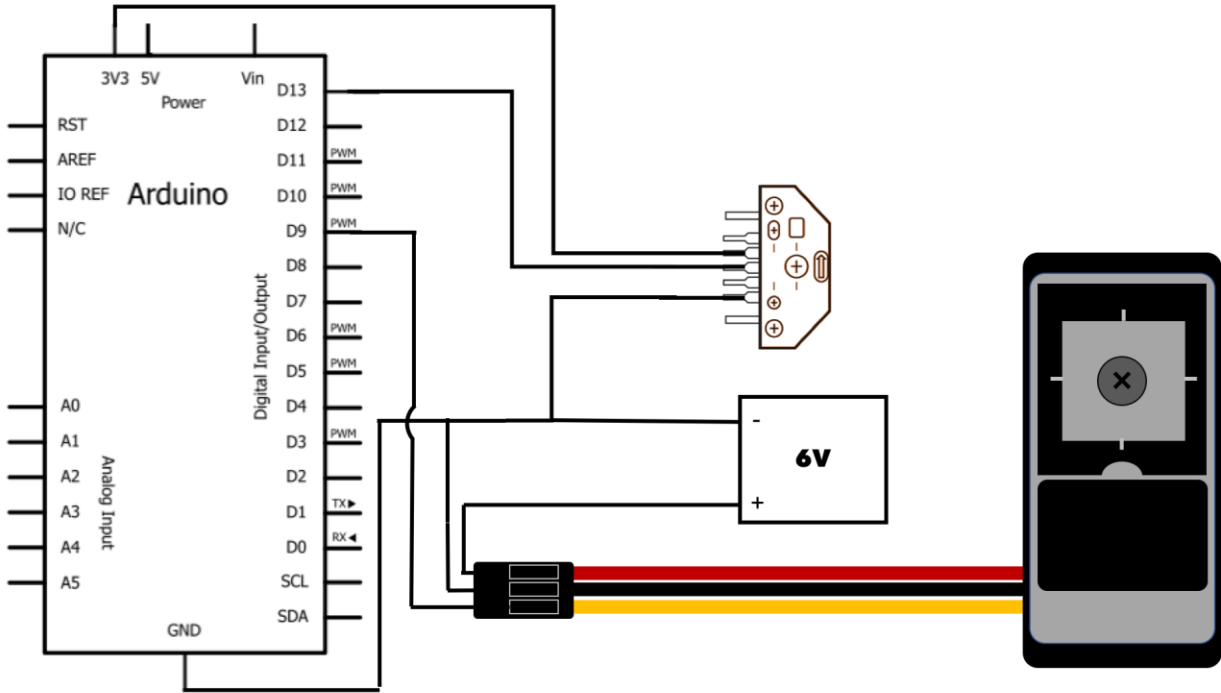


Figure 3.40: Circuit Diagram showing Arduino, Encoder, Servo, and Power Supply

A lot of research was put into choosing the components and ensuring their interface was easy and hassle free. The following is a discussion of the reasons why we chose the components shown above.

Titanium Gear Servo

We chose the HiTec titanium gear servo because its specification met our needs. It has very high torque (46 kg/cm) and was compact enough to fit into our system. Furthermore, the relatively low voltage (6V) required allowed us to stay away from using any additional electronics to ensure the safety of our components. With 180 degrees of travel, we had plenty of linear travel, since the brake pads would be nearly in constant contact, so a 360-degree servo would have been excessive. The servo interfaces with the gearbox using a 24-tooth connector.

Optical Encoder

The AEDT-Z00 optical encoder was chosen because of its high count per revolution rate (5000 CPR). This high-count rate allowed us to run our spindle at high RPMs while still being able to accurately track the angle of the encoder wheel. Furthermore, the two-channel output of the encoder gave us great flexibility when testing the mechanism as we could check counts whilst deploying and respooling the reefing line. In addition, similar to the servo, its low voltage requirement allowed us to keep low power requirements for all of our components. We decided to use an optical encoder over a resolver, as our research into resolvers showed that they were bulky and often difficult to implement properly without specific expertise. Although optical encoders were susceptible to foreign matter interference, we designed our housing to ensure that our encoder was shielded to reduce this. Furthermore, inductive encoders or resolvers were both found to be incredibly expensive in order to achieve the high resolution required.

Encoder Wheel

We decided to make our own encoder wheel as there did not exist an encoder wheel that met both the Counts Per Revolution (CPR) requirement and the size requirement. As we intended to have a large encoder wheel, since space was limited and thus the encoder had to be eight inches in diameter to be exposed beyond the rope, we designed our own and cut it from ABS. The encoder wheel would allow 200 CPR and mounted easily to our spool for convenient access by our encoder. We laser cut this encoder wheel as it offered great precision and ease for prototyping.

Arduino Microcontroller

We chose the Arduino UNO microcontroller for a few reasons. First of all, it had a familiar IDE and computer interface meaning that writing the control system program was simple and easy to debug. Secondly, it had all the required inputs and outputs, especially 3.3V and PWM outputs, which allowed us to power the encoder and control the servo. Furthermore, its small size fit well into our electronics enclosure and allowed us to keep the mechanism small. Additional to these advantages, the Arduino IDE has a built in Servo library which used to easily control the servo. This proved to be invaluable, saving us the time we would have spent writing our own Servo related functions to control the position. A servo can be controlled by importing the servo library using `#include <Servo.h>` and then creating a Servo object. This servo can be interacted with in the same way as any object as the Arduino variant of C++ is Object Oriented.

During our tests, the Arduino was connected to a laptop and the Servo was connected to a 6V power supply. However, adequate considerations were made to allow both the Arduino and Servo to be powered by a battery that would sit inside of the electronics enclosure. This battery would likely be a LiPo battery, which would have both high capacity and high discharge rate to allow the Servo to operate at maximum torque for an extended period of time.

Control Systems

The overall goal of our control system was to allow the device to deploy reefing line at a given velocity regardless of the reefing line tension. Knowing this as our goal, the control systems focused on the rotational speed of the spool spindle, which allowed us to track the length of reefing line deployed as well as the rate of deployment. Through an Arduino program, we were able to successfully track the length of line deployed as well as controlling its rate of deployment.

Our control system code can be split into a series of discrete functions that act together to achieve our final goal.

Update State Function

This function tracked and calculated all of the fundamental variables over time. It calculated rotational velocity and acceleration from angular position over time and, as a result, was able to calculate the velocity of the reefing line and the length of line deployed. This function ran constantly over the course of the function to ensure accurate variable tracking.

The code in the appendix gets the encoder position from the encoder and translates this to the number of revolutions of the spool using the number of encoder markings on the encoder wheel. Then using the radius of the spool, the number of revolutions is converted to the length of line deployed. By tracking this, at each time step the velocity of the line is calculated. From these two values, it then calculates the velocity error and thus recognizes how to change the system to meet the velocity goal.

Print State Function

This function allowed us to debug code and log data. This function connected to an external application (*gobetwino*) to store the data within a log file for later use. Being able to track the state of our device was incredibly useful and allowed us to obtain very accurate data. Without this, our data source would have included some element of human error - undesirable when attempting to track quickly changing variables. This data was then used to analyse the effectiveness of our system and to understand important key metrics of our system including the latency of the servo motor.

Encoder Servo Connect Function

This function allowed us to use the encoder data to control the servo. Overall, using this function, we were able to run tests which showed the precise control we could obtain using the device. By setting velocity goals, we were able run this function as a PID feedback controller to allow reefing line to deploy at any given speed. Using this function, we were able to run tests quickly and effectively as any changes were easy to make and configurations could quickly be updated. Gains of the PID controller were found experimentally by running tests and varying system parameters to ensure accurate function.

Using this function, we were able to run two types of tests. One test was to change the velocity of a constant mass. The other was to keep the velocity constant of a variable mass. The type of test was controlled by the Boolean variables *v_test* and *m_test*.

Enclosure

The entire of the electronics was placed in a 3-D printed enclosure. This allowed the electronics to be mounted to the enclosure and then mounted to the external steel housing. The enclosure was designed to be as unobtrusive as possible and thus was made to be as small as possible. Below is a photo of our enclosure.

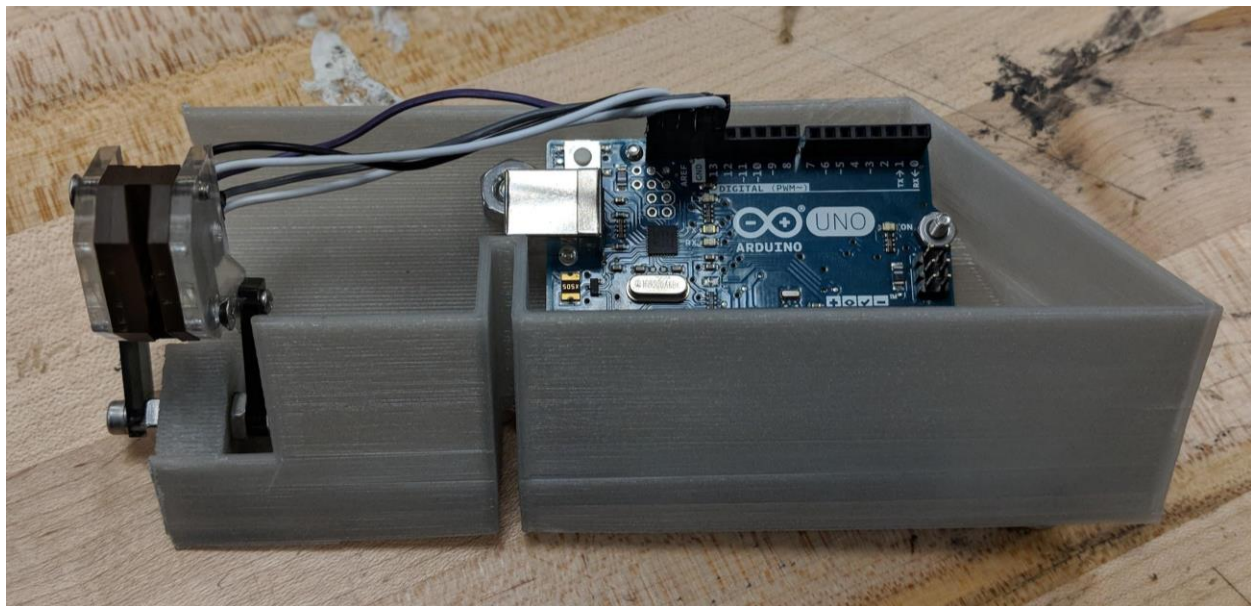


Figure 3.41: Electronics Enclosure

Manufacturing



Figure 3.42: Picture of Final Product

Manufacturing Summary

Overall, the manufacturing of our device was done entirely in-house with the exception of two outsourced parts - the steel top plate and the gearbox brake housing - which could not be constructed in-house due to limited machining capabilities. The table below summarizes the machining processes conducted for each component of our system.

Table 3.2 - Manufacturing Summary

Subsystem	Part Description	Qty.	Dwg No.	Raw Material / stock	Manufacture Process
Active Brake	Brake Housing	1	1.1	Aluminum Block	- CNC machined (outsourced) - Post Process on Mill
	Gears	5	N/A	Gears from McMaster Carr	- Cut with bandsaw - Welded together
	Long Gear Shaft	1	1.2	3/8" diameter aluminum rod	- Cut with Bandsaw - Process on Lathe
	Threaded Gear	2	1.3	3/8" diameter	- Cut with Bandsaw

	Shaft			aluminum rod	- Process on Lathe - External thread die
	Spacers	3	N/A	½" diameter aluminum rod	- Cut with Bandsaw - Process on Lathe
	Brake Pads	2	1.4	Brake Lining	- CNC Mill
	Stiffness Plate	1	1.5	0.5" Aluminum Plate	- CNC Mill
Passive Brake	Capstan (V1)	2	2.1	Aluminum Block	- 3 Axis Mini Mill - CNC Mill
	Capstan Block (V2)	2	2.2	Aluminum Block	- Bandsaw - CNC Mill
	Capstan Rods	4	2.3	½" diameter aluminum rod	- Cut with Bandsaw - Process on Lathe
Spool	Shaft	1	3.1	¾" diameter aluminum rod	- Cut with Bandsaw - Process on Lathe
	Brake Disc	1	3.2	⅛ aluminum sheet	- CNC Mill
	Separator Plates	4	N/A	0.050" Delrin Sheet	- Laser Cut
	Mounts for Brake Disc	2	3.3	0.5" Aluminum block	- CNC Mill
Enclosure	Side Walls	2	4.1	9" Diameter aluminum Disc	- CNC Mill
	Top Shell	1	4.2	0.050" Sheet Metal	- Laser Cut / Bent/ Welded (outsourced) - CNC Mill
	Top Plate	1	4.3	0.25" aluminum stock	- CNC Mill
	Rope Exit Guides	4	4.4	0.75" Diameter brass rod	- Lathe
	Round Bottom Shell	1	N/A	Carbon Fiber Sheet	- Carbon Fiber Layup
Other	Mounting Fixture	1	N/A	¼" Aluminum Stock	- CNC mill

Manufacturing Subsystem Highlights

Much of the manufacturing process required fairly straightforward, though time consuming, CNC mill, lathe, and drill press operations. However, each subsystem of the overall device presented one or two components that presented interesting manufacturing challenges, which are highlighted below.

Active

While the design of the active brake is discussed in detail above, the housing is worth highlighting again from a manufacturing perspective. The part underwent numerous redesigns, but the most interesting was the decision to integrate the angled mounting portion with the rectangular body of the brake. Initially, when we were intending to manufacture this entire part in-house, we had designed a separate brake gearbox to hold the gears and then an angled mount to interface with the sidewall of the top piece. However, when we decided to outsource the part, we realized we could integrate these two parts into one in a way that would improve function, reduce weight, and reduce part count, which increases reliability. Integrating these parts meant that we would have to do post-process machining, since we had to drill and tap the mounting holes in house, because this saved about \$200 on the part order.

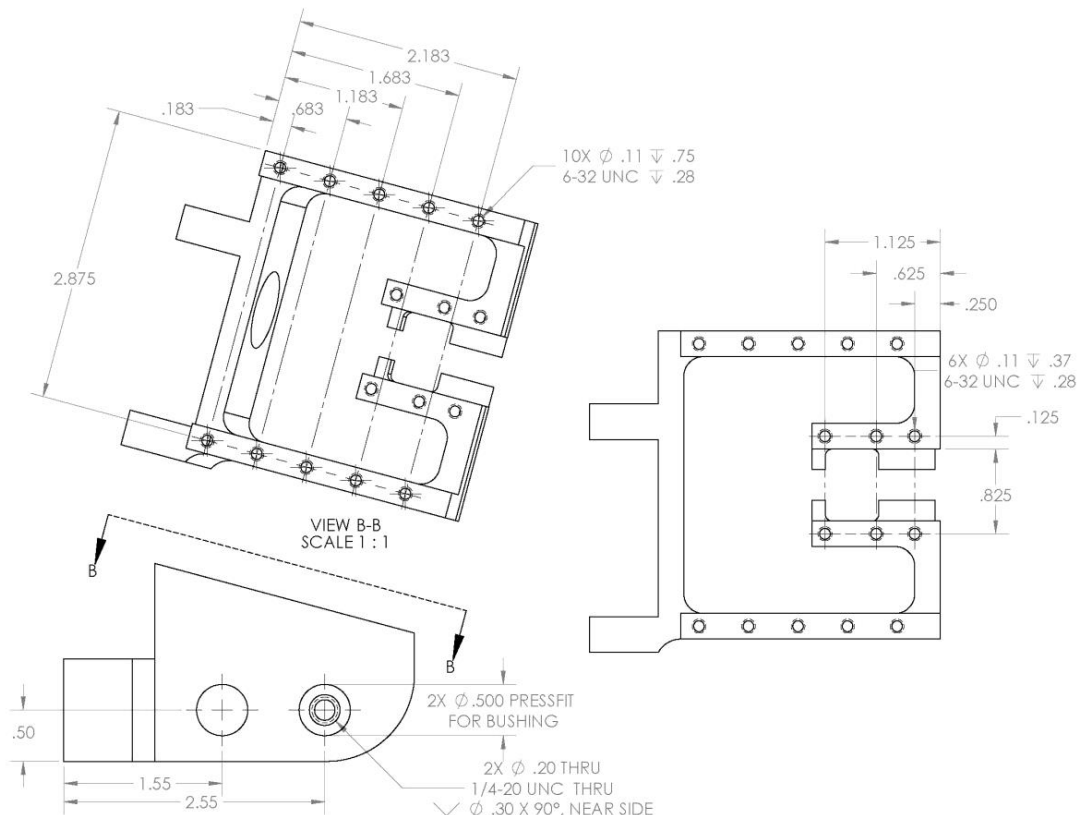


Figure 3.43: Final Part Drawing for Active Brake Housing with Integrated Mount

When these parts had been integrated and outsourced, we still had to complete a number of drilling operations to get the part ready for assembly. First, each of the outer holes for gear-shaft mounting had to be drilled and reamed for the bearing press fits. Once these holes had been cut, a drill and tap were reintroduced to tap the 1/4-20 internal threads that would be used for the threaded rods, used by the gears to translate torque into linear force. Finally, the ten mounting

holes were drilled and threaded using an angled block to ensure the brake would be mounted flush to the top plate sidewall.

The clutch lining was milled into shape and tested to confirm its friction properties. While it was advertised to have a coefficient of friction 0.5, our testing indicated that it in fact had a coefficient of friction of 0.3. This unfortunate shortcoming means that our mechanical caliper brake only supports loads up to 1.6 times our maximum expected load. While this is still a comfortable safety factor, it does not meet the goal that we developed with NASA of a 2.0 safety factor.

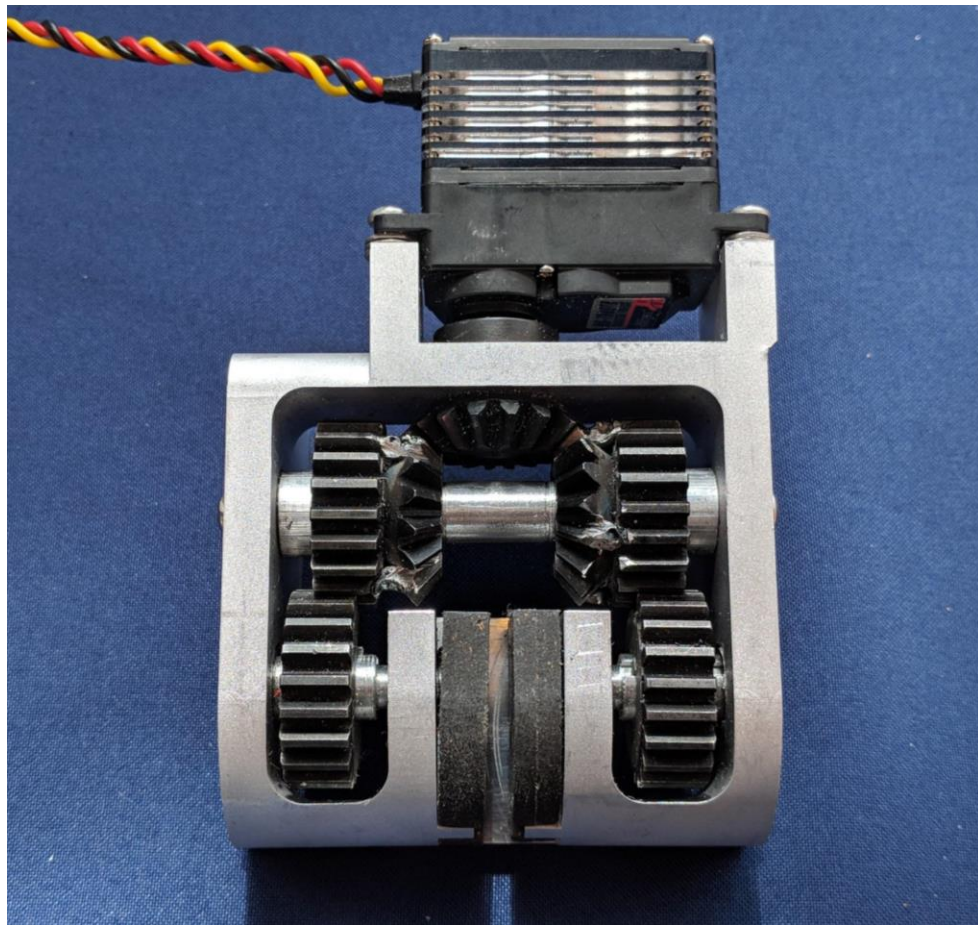


Figure 3.44: Assembled Gearbox

Assembly for this part was quite complex, as the part was designed to be as compact as possible. The order of operations was strict, as the unit was otherwise impossible to assemble. First, the bottom end of the assembly was stretched apart with pliers to create enough clearance to insert the brake pads (as they were slightly thicker than quoted by our supplier), after which the stiffness plate was screwed into the backside of the brake pad assembly. Once the brake pads were in place and the support plate added, the uncut miter gear had to be attached to the servo linkage using a pin, then this assembly was inserted into the gearbox. Next, the keyed straight gears were each held in place, with the steel key glued into their slot, as the keyed threaded rods were inserted through the bushings. The gear and key slid onto the keyed shaft, which was then threaded until the rods were fully contained in the bushings. Next, the two miter/straight combination gears were then held in place as the mounting rod was inserted through the bushings and the gears. Once these were mounted, the outer spacing rings were inserted one at

a time by pushing the mounting rod back and forth to create clearance. Finally, the mounting rod was anchored in place using the 6-32 threaded holes and washers, ensuring it would stay properly located. While this assembly process was complex, it worked reliably with sufficient tolerance to assemble and disassemble the gearbox as needed to make calibration adjustments.

Passive

The capstan machining operation was complete on a manual mill. To start, a block of aluminum was squared and shortened to size. Once all sides were faced, and each dimension set, the press-fit holes were added. These two holes were an inch deep and had very small tolerances as the capstan rods needed a secure fit. After center drilling a #7 drill was used to drill a 1-inch deep guiding hole. Next a 31/64th drill bit was used to get the hole ready for reaming. A .495" reamer was used to create a tight press-fit for the capstan rods. To conclude, a .505" reamer drilled down ~.125 inches. This ensured that the rods were able to partially sink into the block before being pressed. In the second major operation the slots were added. This involved taking a 1/4 inch end mill and running along the length slot. This operation took use of the mill's power jog feature which allows the mill to run a set distance at a set speed. This made the operation easier on the operator, saved time, and resulted in a cleaner internal finish. As the slots go through the entire thickness of the part, many passes were needed. Each pass would begin by plunging with the end mill roughly 50 - 70 thousandths of an inch, and then moving over the length of the slot. Using the zero set with a vice, the top and bottom operations were completed next. This included drilling 2 1/4 inch holes on the top and bottom of the capstan. This completes the channel that room would later slide through. In order to allow the rope to pass in and out of the capstans a radial cutting tool was used to round off the exit and entrances.



Figure 3.45: Manufacturing the Capstans

The capstans were designed with manufacturing in mind. This was helpful when dealing with the triangular shape of the finished product. To make this operation easier a 30-degree angle was chosen. To machine this profile, the part was placed in a 30-degree angle block. From this point a face mill was used to flatten the edge of the triangle. After each pass the face mill was lowered 50 thousandths of an inch. The operation was complete when a sharp edge formed along the bottom of the capstan. Finally, holes were drilled along the angled side of part. These were 1/4-20 thread screws half an inch deep.

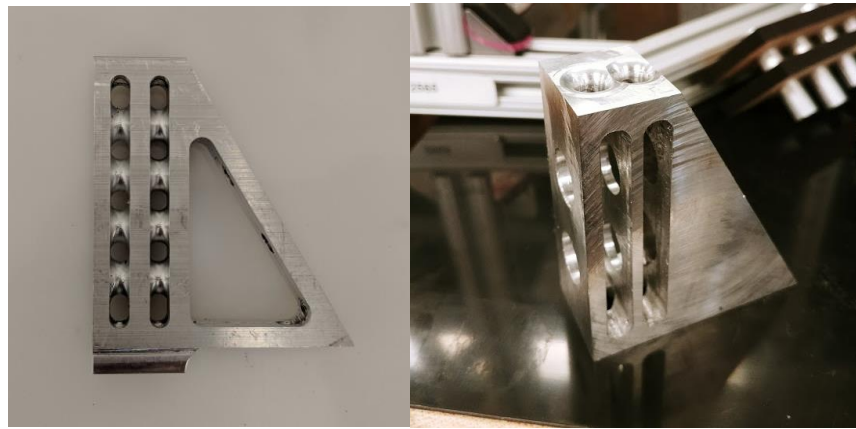


Figure 3.46 & 3.47: Completed Capstan Post Machining (v1 left, v2 right)

Spool

In manufacturing the brake disc hub, the primary concerns were ensuring that the D-slot would properly interfere with the D-slot on the shaft while the hex bolt pattern is engaged. Rather than attempting to create two separate parts which could introduce variability into the hole alignment, the A and B sides of the hub were created from a single aluminum block that was later sliced into two pieces, ensuring that all holes would be perfectly aligned as they were cut in the same instance.

First, a generic block of aluminum of the required thickness was mounted and had the hex bolt pattern drilled. This was then used to mount the block to a corresponding mounting block, which was used to CNC mill the external and internal geometries using a $\frac{1}{4}$ " end-mill. The internal profile of the D-slot was designed specifically to match the radius of this tool. From here, the hub was mounted vertically in a drill press to have the two threaded mounting holes added. Once all of these holes had been cut, the hub was separated into A and B sides in the vertical bandsaw, ensuring all components would assemble without complication.

Enclosure

The round shell of the Daedalus enclosure was made from 3 layers of carbon fiber. Carbon fiber met our size and shape needs and since we were able to lay it up ourselves, we could tailor it to fit our design. Since this round shell was not load bearing, as the steel top piece was designed to carry all loads, carbon fiber provided a very lightweight but robust solution for this geometry.



Figure 3.48: 3D Printed Mold Bending and Wrinkling Under Vacuum Pressure

We initially tried to 3D print our mold, but this crippled under the vacuum pressure and produced an uneven, rough surface finish. We then found a PVC pipe that approximately fit the size of our enclosure. We laid up a shell part using the PVC as a negative mold, which also yielded a rough result, although the shape was much more even. Finally, we used the PVC as a positive mold and the carbon fiber fit the shape of the design, all while being aesthetically pleasing.

4. VALIDATION AND TESTING

Summary

To test parachute systems, aerospace companies will perform drop tests. This typically includes dropping a realistic stand-in for the actual payload with a fully function parachute system from a airplane. This allows organizations like NASA, and SpaceX to replicate reentry conditions as closely as possible. These tests are extremely expensive and are only conducted after each individual parachute component is validated. Given that a test at this scale would be outside the scope of this project, a different approach to validation was taken. Even if one of the stakeholders had offered to conduct an actual drop test, the individual components had not been tested. To start the testing process subsystems were separated and examined. This served the purpose of characterizing physical constants, as well as ensuring that subsystems could survive at the necessary loads. For the majority of the tests the MTS machine in B2 was used. This machine would output the force needed to pull the reefing line out at a specified rate. This data was then used to calculate the relevant constants.

Once all necessary subsystem tests were run, two integrated system validations were conducted. These provide the clearest evidence of Daedalus's success. To demonstrate control of the active brake the system was tested in real time. Finally, a dynamic simulation was built. This set of three concurrent simulations took the physical constant calculated in earlier tests as inputs and output a realistic parachute diameter and force profile.

Pseudo-Static Testing

Determining Coefficient of Friction and Capstan Reduction

To correctly model our system, the realistic coefficients of friction were needed. These affect the amount of force the capstans can reduce, as well as the effectiveness of the disc brake. The MTS machine was used to calculate both, as it can output the force required to move a known mass.

Without looking at the capstan equation itself, the coefficient of friction was determined by simply hanging mass off each Kevlar rope in our system. This isolated the capstans from the rest of the system and allowed for the passive brake to be tested. Once the increase in force was calculated by the MTS machine, the coefficient of friction could be calculated.

$$T_{Load} = T_{Hold} e^{\mu\varphi} \quad (18)$$

In the case of this test, T_{Hold} represents the original force that the known mass applies. T_{Load} is the force that the MTS machine must apply to lift that mass. The μ represents the friction term. Since the φ (wrap angle) is known, the μ can be calculated. Three sets of weights were used to make sure the results were consistent. In each subsequent test additional mass was added to each rope. As the test began the MTS started to pull on the rope as the device stayed still. Once the rope was taught the device itself begins to lift-up until it became even with the pulleys. At this point the rope would start to move through the capstans. The MTS would output load required to move as a function of distance travelled.



Figure 4.1: Capstan test rig with hanging weights to act as a known force

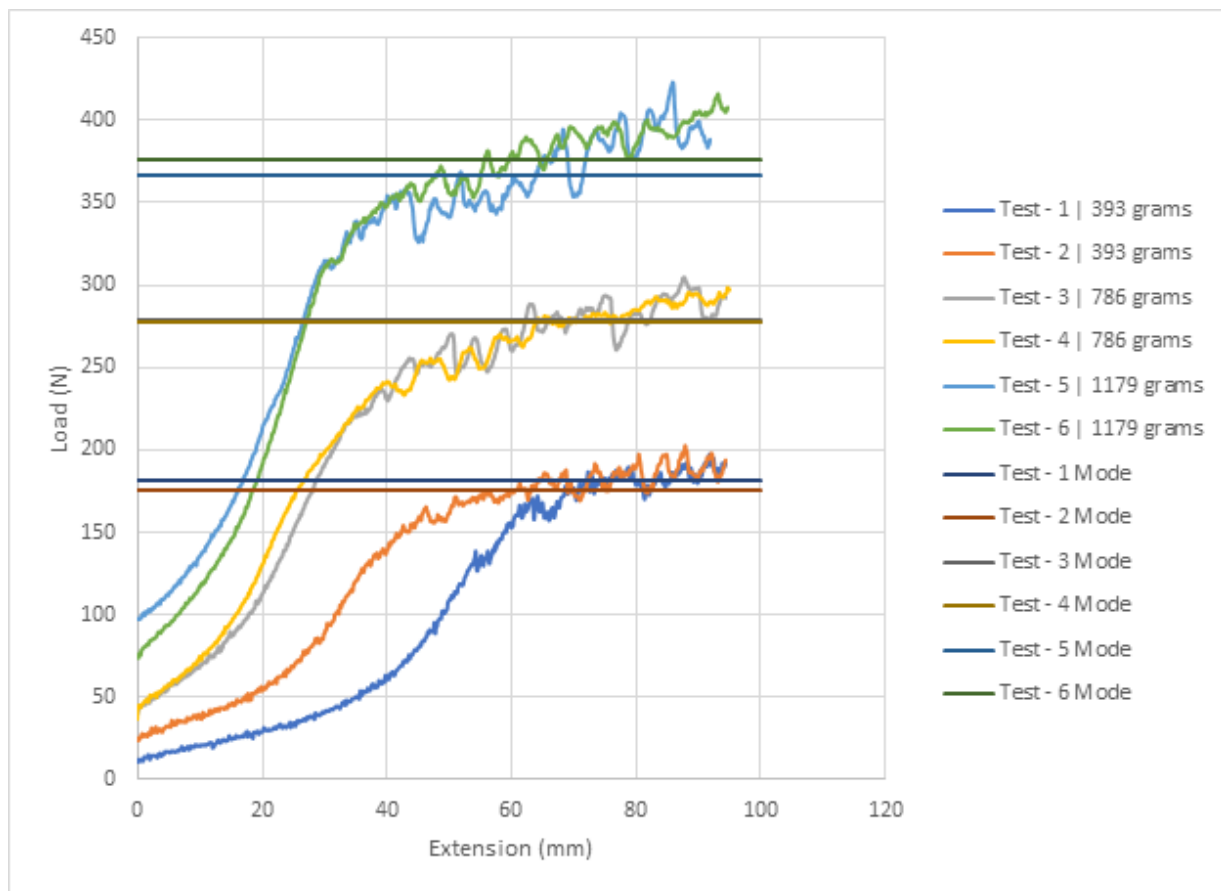


Figure 4.2: Graph of Extension vs. Load

	Test 1	Test 2	Test 3	
<i>Mass per Line</i>	393 grams	786 grams	1179 grams	
<i>Total Mass</i>	1572 grams	3144 grams	4716 grams	
<i>Weight</i>	15.42 N	30.84 N	46.26 N	
<i>Load</i>	178.55 N	278.27 N	370.87 N	Averages
<i>Percent Difference</i>	91.36%	88.92%	87.53%	89.27%
<i>Exponential Term</i>	2.449	2.200	2.081	2.243
<i>Reduction Factor</i>	11.578	9.022	8.016	9.539

Using the results, the “Exponential Term” was calculated. This is equal to $\mu\phi$. Since ϕ is known to be 500 degrees or 8.73 radians the coefficient can be calculated to be .257. With a coefficient of .257 our capstans reduced the force the active system needed to fight by a factor of 9.5. This combination of a coefficient of .257 and a reduction factor of 9.5 was within the bounds set before testing.

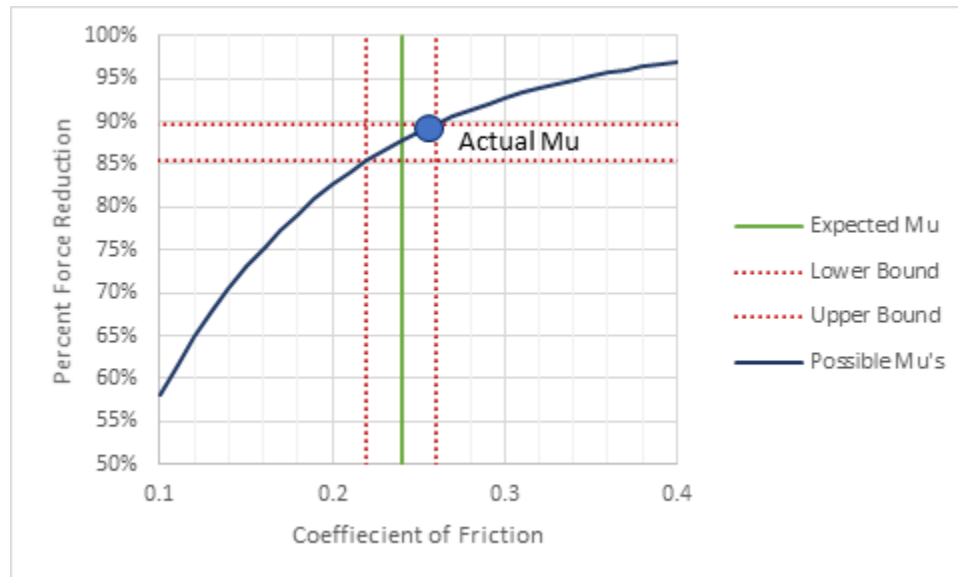


Figure 4.3: Graph of Force Reduction vs. Coefficient of Friction

These tests validated that the passive brake system could withstand high forces while also characterizing the force reduction.

Servo Characterization Process

To isolate determine the braking ability of the active system, the device was hung in the testing rig upside-down. This allowed the rope to bypass the passive system, giving a more accurate

characterization of the servo. Tests were run where the rope was pulled at a constant speed and the force needed was outputted.

One major challenge from this test was making was isolating the servo. If the rope was allowed to run through the capstans before then the MTS would read a force much higher than necessary. Daedalus was placed on its side and the bottom carbon fiber was removed. In order to ensure that the ropes could exit the device without fraying a guiding plate was attached to the device.



Figure 4.4: Servo Test Setup

The purpose of this test was to understand how incrementally stepping the servo motor would affect the force needed to move at a constant speed. As expected up until the point of contact the servo did not change the force needed. As more contact was created between the brake pads and the brake disc more force was needed. This relationship between a single degree step of the servo to an increase in force was characterized. Unfortunately, there were only a few degrees of rotation between no braking force, and full braking. At full braking the 80-20 support rig, that was bolted to the MTS frame, began to bend. This meant that the less force was needed to pull on the 80-20 than was needed to rotate the spool. This information was useful as it set a good lower limit on the servo position control.

While not all test data was useful, a clear trend could be see between the angle position of the servo and the force required to pull on the system. The graph below illustrates the force required a serval servo positions. As the servo is stepped up, the force increased. These results were used when programming the Arduino as the team knew around what position to start the device to quickly be able to apply a strong braking force.

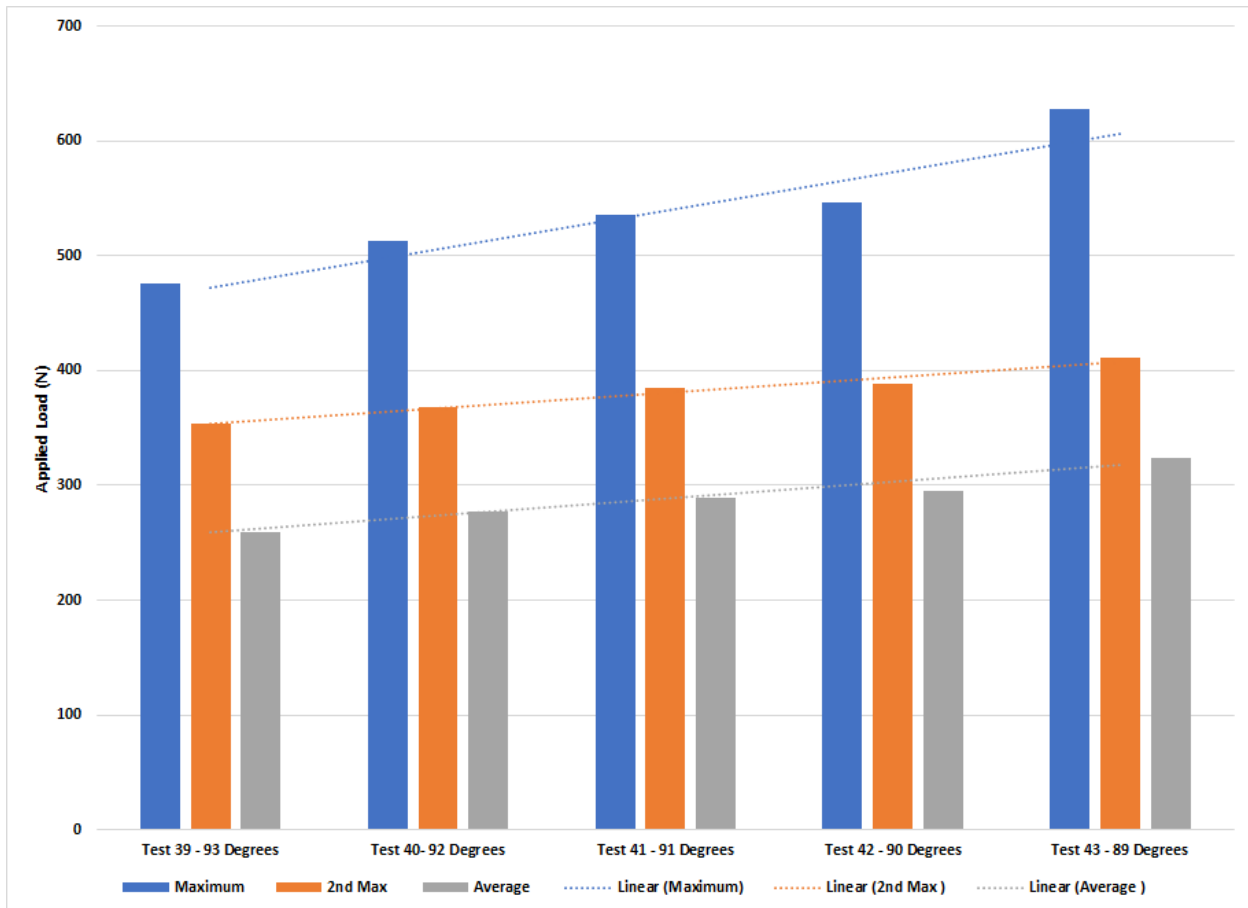


Figure 4.5: Bar Chart showing Applied Load variance with Servo Degree

Integrated System Validation

Active Control Verification

Testing the full dynamics of our system, a 100lbs mass was dropped 1.5 meters. The controlled descent was governed by the passive and active brake. Several different tests were run, but each had some threshold velocity that the onboard microcontroller was monitoring. At this velocity, the computer would engage the servo motor and stop the mass from falling.

A combination of an Arduino Uno and an optical encoder were used to control the free fall of mass. The encoder was constantly calculating the velocity of the spool, which was used to calculate the speed that the mass was falling. This information was processed by the Arduino which would instruct the servo how to move. Since servo's respond to position control, the Arduino would rotate the servo by a set number of degrees for each movement. At every instance the Arduino would decide if the system should be “braking” or “opening.”



Figure 4.6: Payload Test

The device was braced against a staircase and allowed to hang upside down. The reefing line cord hung down towards the ground and was attached to a mass. The rope was then spooled up 1.5 meters off the ground. The first test that was run was to see if the mass could be stopped midair. Once this was proven to be possible, more difficult tests were attempted. Here a threshold velocity was set which required the system and mass to always beneath this mark. When the mass accelerated down, the brake would kick in and momentarily stop the device. This worked for several different thresholds. The goal of the final test was to achieve a seamless profile, meaning that the mass wouldn't stop on its descent. This was achieved by setting two different velocity thresholds and having the mass fall first at the fast profile then at the slower one, before returning to the fast one. This was believed to be a solid validation of our mechanics, as there is no reason hundreds of thresholds at different time steps couldn't be implemented.



Figure 4.7: Brake and Gearbox Setup Mid Test

Daedalus used several different dynamic tests to prove the functionality of the system. Through the different tests the servo control was mastered, and the active brake was validated.

Dynamic Simulation

As stated, it is beyond the scope of this course and our budget to perform a full-scale test of the Daedalus device in the way that is standard of parachute teams. This would entail installing the Daedalus in full-scale parachute, attaching this to a dummy mass (for example, a mass the size and weight of NASA's Orion capsule), and repeatedly dropping the mass and parachute out of a plane or helicopter above a region cleared for high-mass drop tests.

Because this verification was not available to us, we developed a simulation of the drop test in order to validate the integrated function of the system accounting for the tested properties of the subsystems and the known physical limitations of the various components of the system. The simulation, built using MATLAB's Simulink program, approximated the physics of not only our mechanism, but of the entire system in which it acts as accurately as we could.

We derived the relevant equations and fed them into the model, which was constantly updated with variables and constants as they became available through research and experimentation. The basic analysis of the mechanism and the parachute system are each covered separately in above sections, which can be referred to in conjunction with this document if more detail is required about specific aspects of the dynamics.

Simulation Overview

Our simulation consists of three distinct subsystems. The first is the forward parachute dynamics, where the system is given initial conditions for the parachute deployment and our ideal parachute diameter is derived.

This ideal parachute diameter is used as input into the second subsystem, simulating the dynamics of our physical mechanism and the control system in place. This results in a diameter that may differ from our ideal case due to physical limitations.

The ideal and actual diameters are then fed forward into a similar parachute physics model in order to determine the resulting parachute forces obtained. These will be slightly different due to the differing diameter profiles.

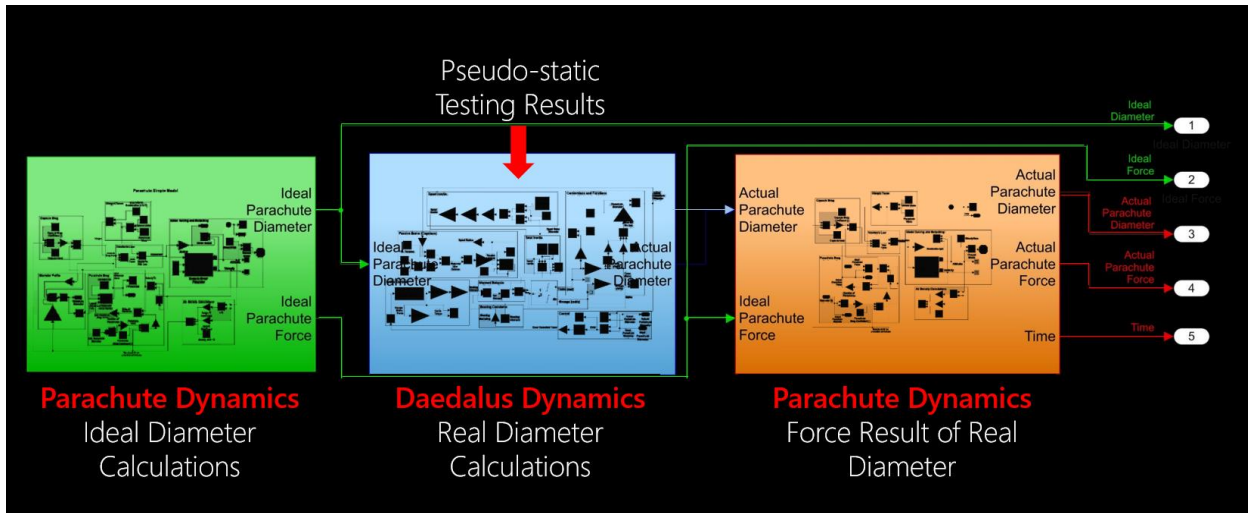


Figure 4.8: Overall simulink Models Integration and information Flow

Parachute Inverse Dynamics

The main purpose of the first section is to simulate all of the physics of a parachute deployment system given a set of initial conditions (altitude, velocity, parachute starting diameter). Typical values for the altitude and velocity during parachute deployment were input into the model. Upon direction from our contacts at SpaceX, we selected 3 percent opening as our starting parachute diameter since this is the smallest value at which the parachute can still inflate.

The physics of the parachute system are discussed more specifically in the parachute analysis section above, but the overall simulink flow of the parachute analysis is seen below.

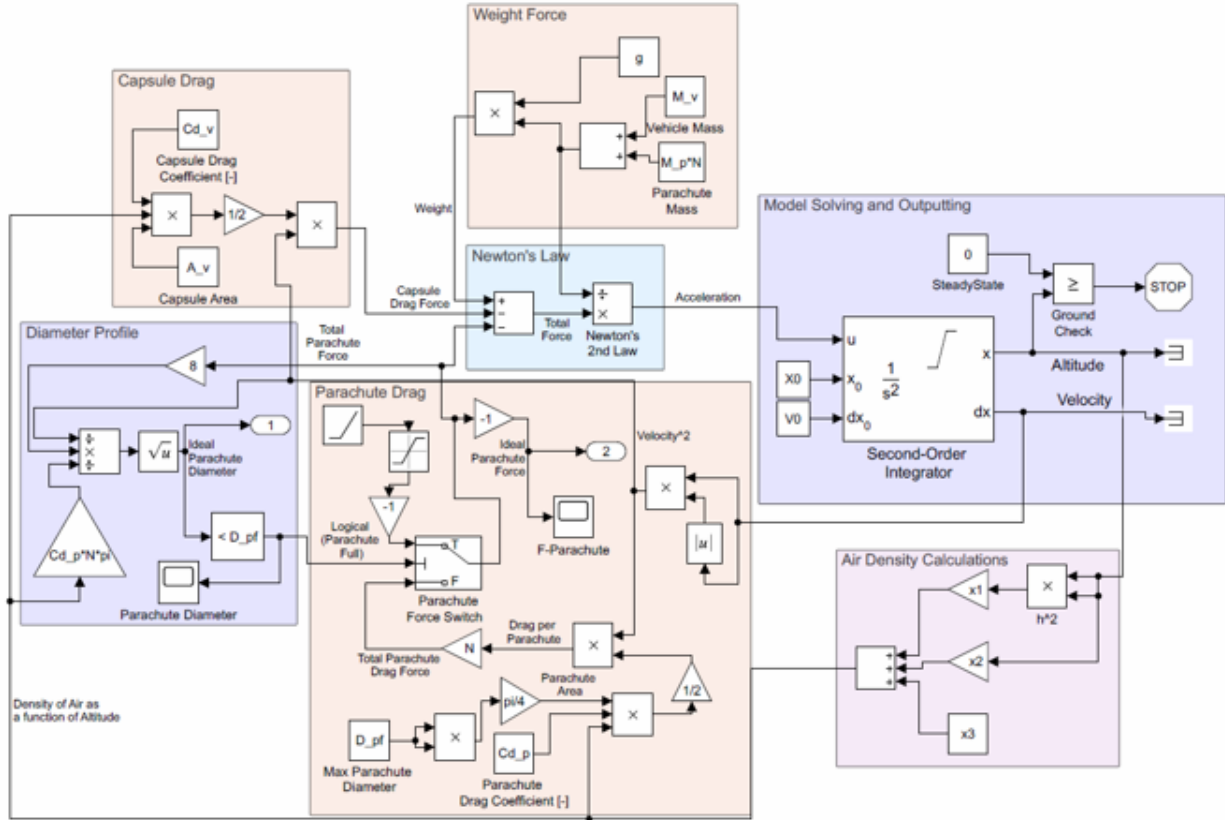


Figure 4.9: Parachute Inverse Dynamics Simulink Model

Through our simulation, we can vary the air density calculation as a function of altitude to account for the increasing air density as the system falls toward the ground. Additionally, this uses a constant value for the drag force of the parachute, as this is the ultimate goal of our device. With time, the velocity continuously updates, which therefore allows us to solve for the ideal diameter profile given the following equation (equation 10):

$$D(t) = \sqrt{\frac{8Z}{\rho\pi NC_{D,p}}} \frac{1}{v_y(t)} \quad (10)$$

Where $D(t)$ is the diameter over time, Z is our constant parachute load, ρ is the instantaneous air density, N is the number of parachutes in the cluster (3 in our case), $C_{D,p}$ is the drag coefficient of the parachute, and $v_y(t)$ is the system velocity in the vertical direction over time.

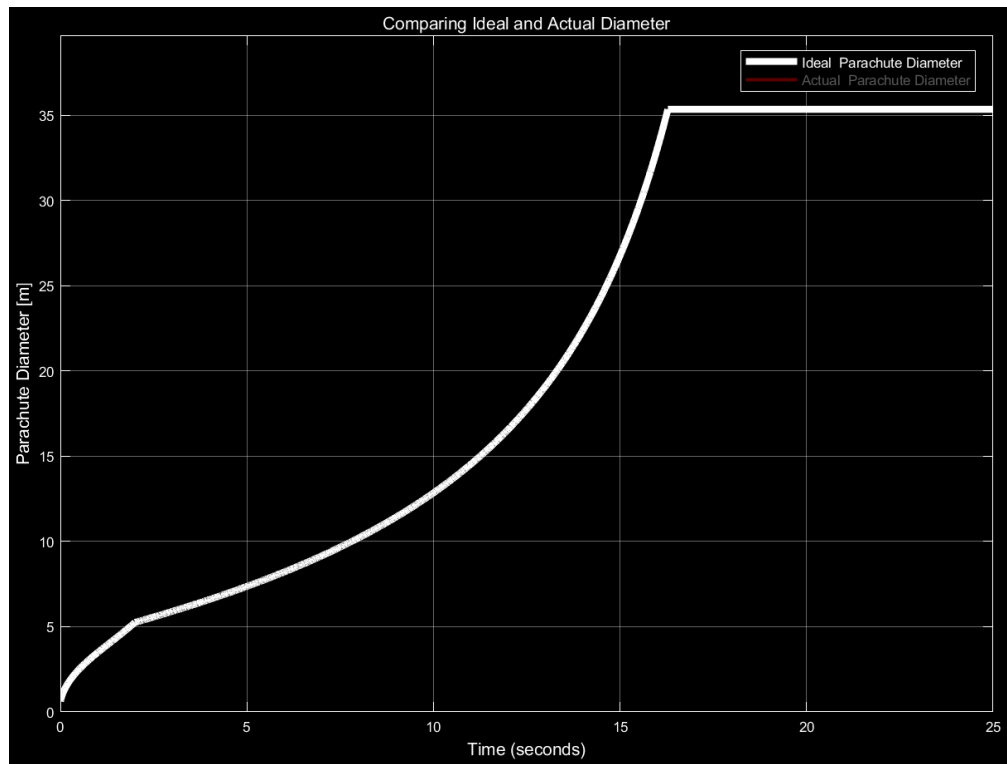


Figure 4.10: Ideal Diameter vs Time Profile from Inverse Kinematics Simulation

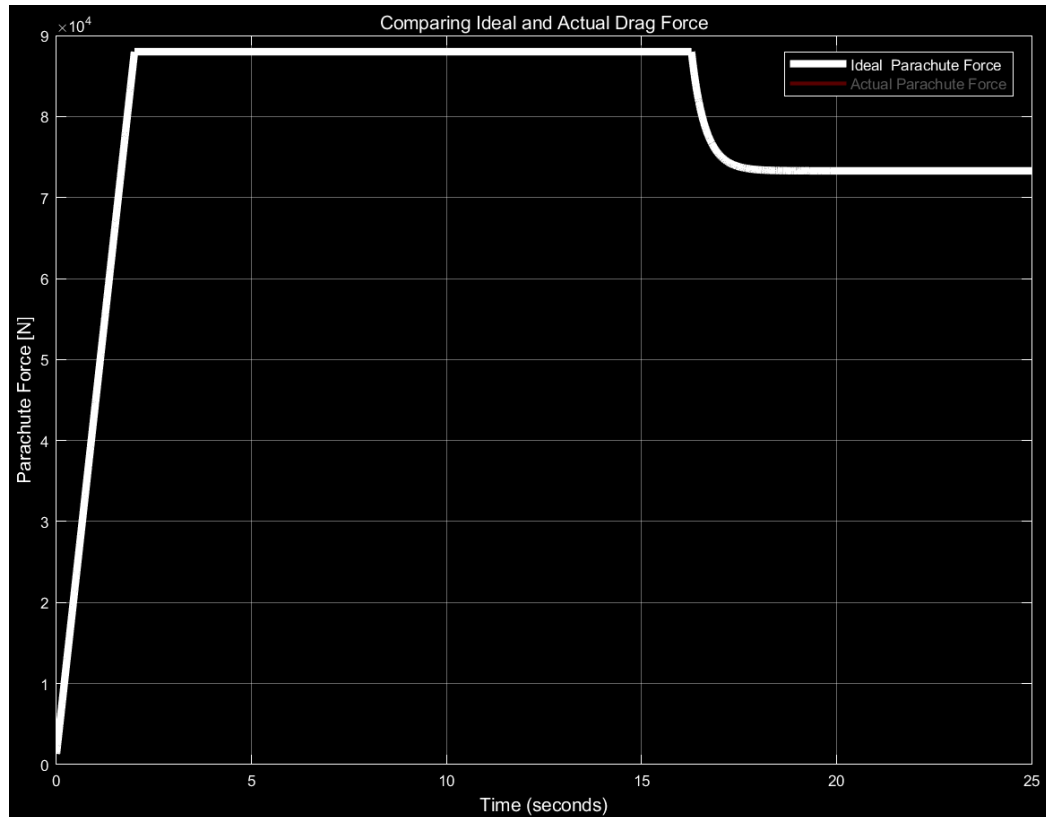


Figure 4.11: Ideal Force vs Time Profile from Inverse Kinematics Simulation

Daedalus Dynamics Simulink

The ideal parachute diameter obtained in the previous simulation is then set as an input into the next subsystem: the Daedalus mechanism dynamics Simulink model. This model accounts for and simulates all the forces that contribute to the moment balance in our system. The large components of these are the passive system (capstan and bearing) and our active system (Electronic Brake).

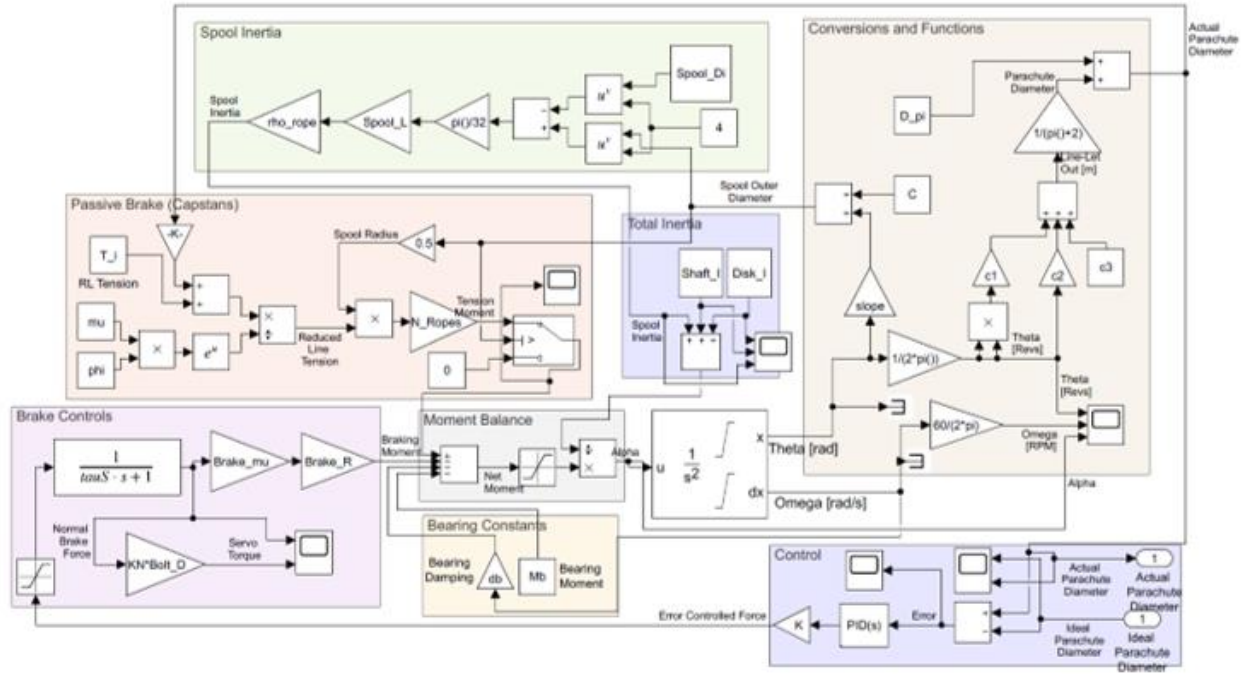


Figure 4.12: Daedalus Mechanism Simulink Model

This model also has several interesting caveats. The moment balance gives us our angular acceleration (α), which we can thereafter integrate to obtain the angular velocity (ω) and the total rotational angle (θ). This rotation, however, corresponds to our rotating spool, so we converted this value into the total amount of line let out at any time. We approximated this relationship through calculations done in excel and used the polynomial fit values in the Simulink model to account for this conversion.

Knowing how much line is let out, we could update our current spool diameter, which feeds back into the system. A feedback system like this motivated our need to build a robust Simulink model as shown, rather than merely relying on our ability to write the ODEs.

This changing spool diameter is required for two of the major calculations. As we let out rope, the inertia of the system decreases, which is accounted for in the Spool Inertia subsystem. Additionally, the radius at which the tension from the line is applied to the system is constantly decreasing. This value must be updated accurately, because, even if the tension in the line remained constant, the applied moment decreases as the spool diameter decreases with time.

The next important section is the Controls section. Here we implement a simple PID controller where we are using our calculated ideal diameter (described in previous section) as our constantly updating set-point. At every time interval, the computer compares this value to its actual value. A corresponding command for the servo brake is then selected and outputted (in the brake controls section).

This command goes through a transfer function that was put in place to better account for the latency between the electronic command and the physical movement of the servo. The value for the corresponding Servo was calculated for our Servo from its maximum spec speed. Additionally, some extra buffer was included to account for on board calculation times.

The command was also saturated at the physical torque limits of our Servo. This limited how much brake force could be applied, but in reality, a stronger torque servo could be used if more extreme cases required.

We tried to complete the model with as many true values as we could find through research, and otherwise tried to determine experimentally. For example, the constant bearing frictional moment and the coefficients of friction of both the rope-Capstan and the brake pad-brake disc interfaces were determined from actual testing data.

In summary, the model takes the ideal diameter as an input and calculates the real diameter that it is able to achieve at each time. The model is driven by the governing moment balance equation:

$$\Sigma M = I_T \alpha = M_{capstan} - M_{bearing} - M_{brake} \quad (33)$$

Or written out fully:

$$\Sigma M = I_T \alpha = \frac{T_{RL}}{e^{\mu\phi}} \frac{D_{so}}{2} - \frac{T_s}{KD_{th}} \mu_{br} R_{br} - d_{be} \omega - M_{be} \quad (34)$$

Forward Parachute Dynamics

The last subsystem is the Forward Parachute Dynamics. This model takes in the real diameter achieved from our mechanism dynamics and runs it through the parachute physics to find the resultant force profile.

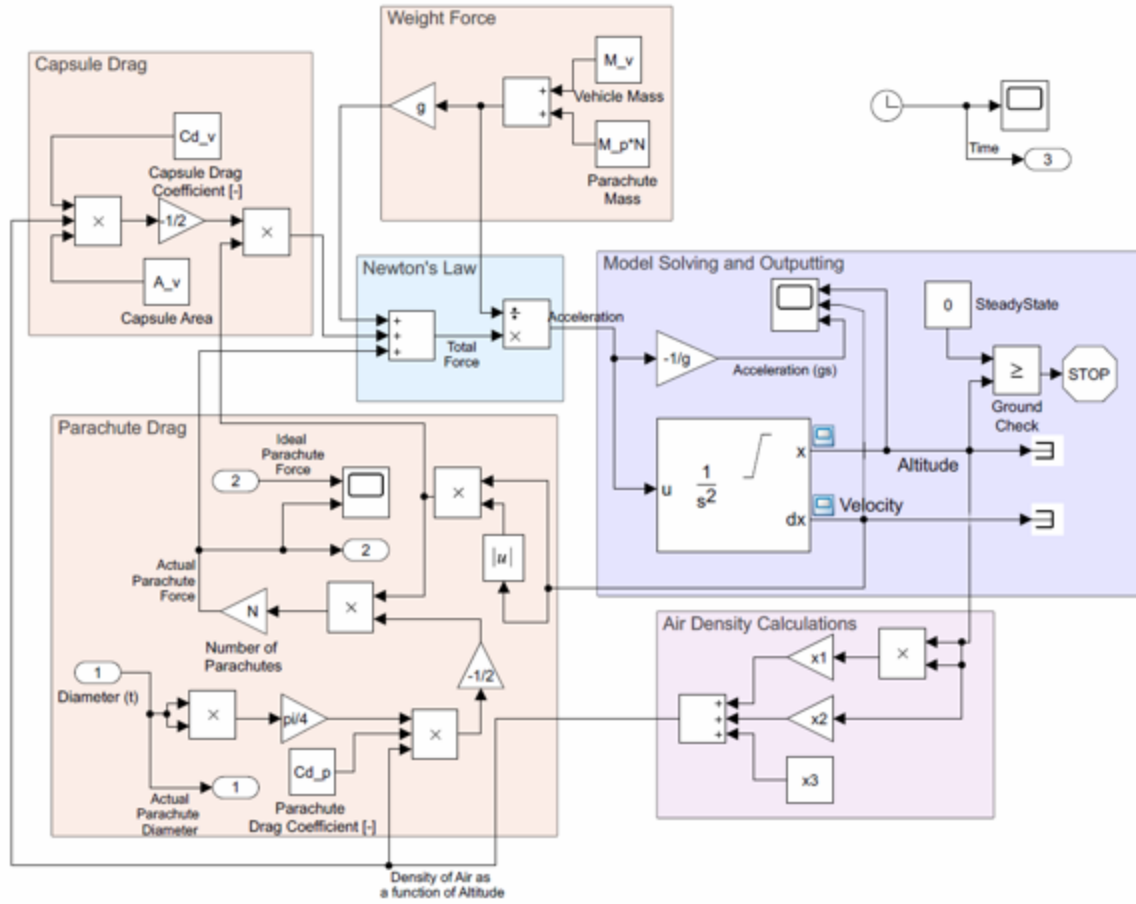


Figure 4.13: Parachute Dynamics Simulink Model

It is therefore very similar to the inverse parachute model, the primary difference being that instead of solving for a parachute diameter, this model takes in the diameter and uses it to calculate the resultant force and physics.

The model is governed by the primary physics equation of the parachute system, denoted in equation 1.

Conclusion and Simulation vs Daedalus Difference

While our simulation does its best to approximate the physics at play, it is merely a tool to use for understanding the types of challenges we had to face and overcome during our design process. Additionally, it serves as a verification method in place of a real-world test.

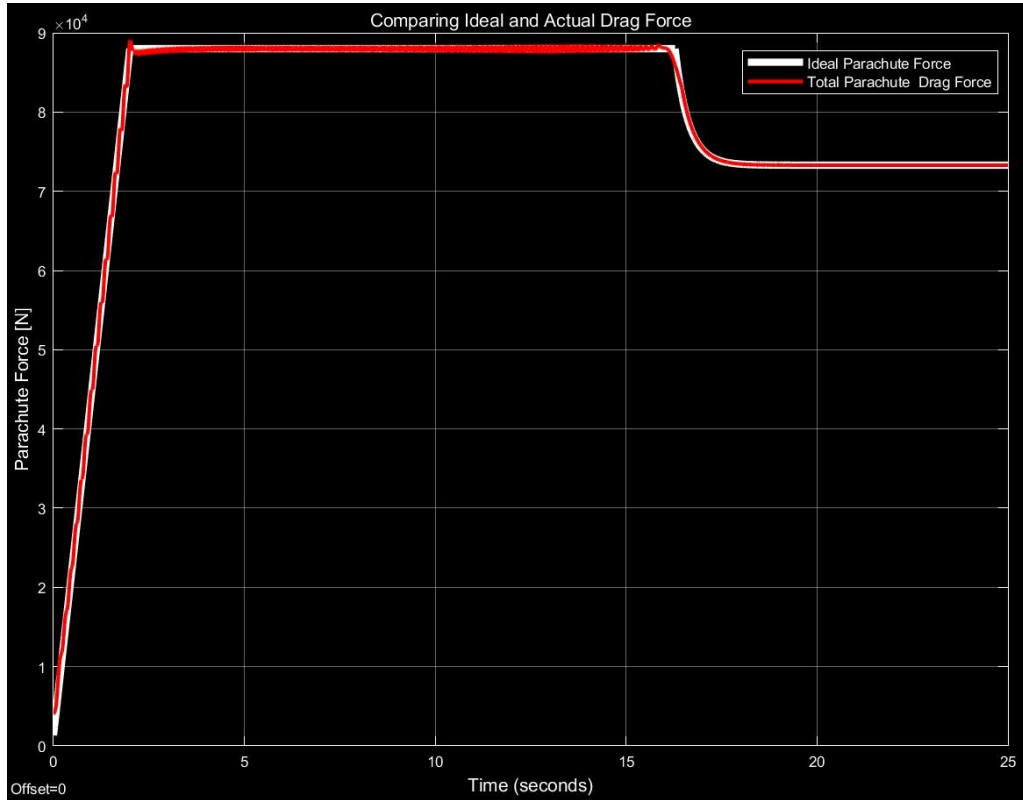


Figure 4.14: Comparison of Ideal and Actual Force vs Time Profile from Simulations

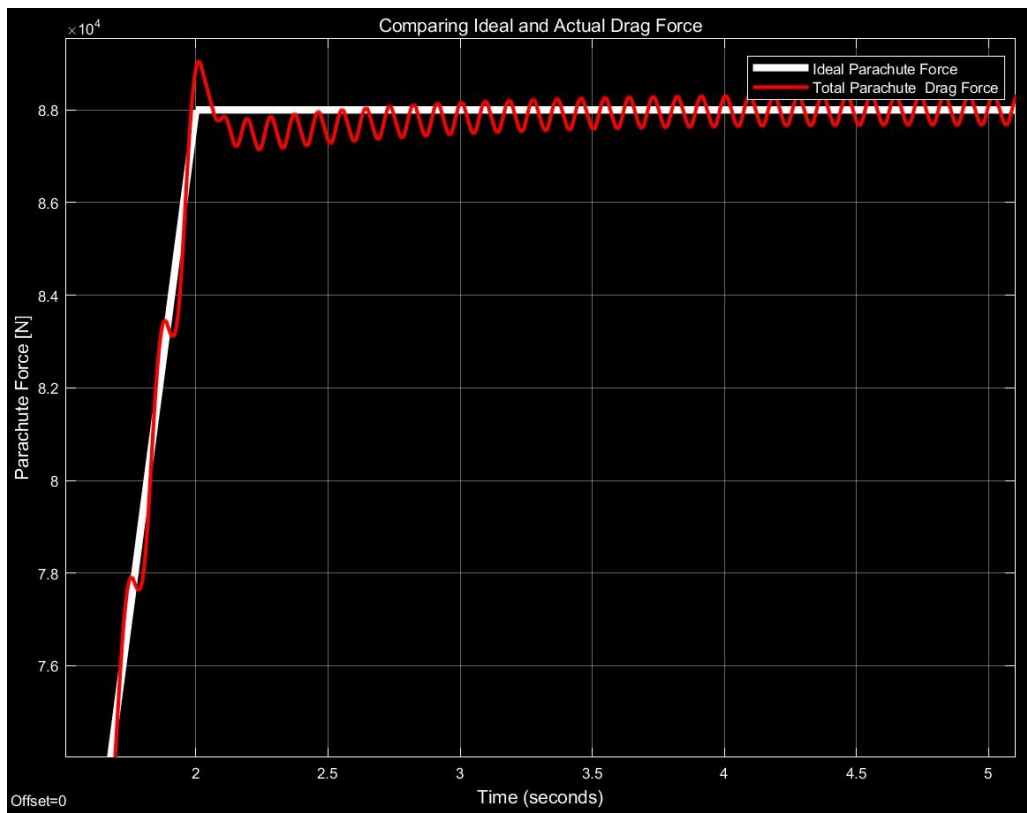


Figure 4.15: Close up of previous plot showing oscillating discrepancies between the ideal and actual disreefing force profiles

While we have built what we believe is a robust model, we are under no illusions that the real physics during operation may deviate from the theory. Predicting parachute dynamics in itself is something that no one has been able to do correctly every single time. This has been reiterated to us time and again in our interactions with NASA engineers and other research groups who themselves are trying to create models that represent parachute dynamics as realistically as possible. Since parachute simulation is so difficult, parachute testing is almost always done empirically.

This is particularly evident in that there is no data or exact equations to model the tension in the reefing line. This is an input to our mechanism dynamics model and drives the opening of the parachute. Because no practical continuous disreefing devices have been developed in the past, there is almost no literature available on how this force varies as a function of diameter or time. Our model uses an approximation for the initial reefing line tension, which we can vary through time. However, the nature of this relationship is clearly not understood well enough.

While the example above, in addition to all the other complex physics of our system, are simulated as best as they can be here. In the end, it is not the driving factor into whether or not our device works. These calculations, however, do not defeat our mechanism. Our onboard computer will not be running these complex simulations. It will use the onboard GPS to calculate its velocity and altitude. From these values it can calculate the ideal parachute diameter at any time. From the encoder, the computer can determine the actual diameter at any time and the control system will modulate the active braking system in order to get these values to be as close together as possible during the entire course of operation.

This all happens with the real physics going on in the background (which our device is not concerned with). The PID controller itself can be tuned to result in the best responses with more empirical operation test data collected. With that, we have been successful in creating the first practical implementation of continuous disreefing.

5. DISCUSSION

Summary of Achievements

Team Daedalus successfully created a continuous disreefing device that can reduce loads experienced by the Orion main parachute system by 28% and reduce the time to full inflation to 17 seconds from 45 seconds.

In order to create this device, Team Daedalus conducted the first full scale investigation of parachute dynamics during continuous disreefing, developing a deep understanding of the theoretical and practical limits of a continuous disreefing device as well as the impact such a system could have. This free body analysis utilized a complex Simulink simulation to develop a relationship between parachute diameter, parachute load, and system velocity over time. This analysis generated a diameter profile over time that was used to drive the functional design of the device, as the disreefer must be able to control the release of line to match that profile.

The device is designed to survive 1200 lbf of line tension, accounting for the two times safety factor over the expected maximum line tension of 600 lbf. The device was only verified to nominal loading due to testing limitations (specifically the failure of the 8020 Aluminum testing frame under load), but FEA component analysis verifies that we should be well capable of surviving the expected loading. We further demonstrated that the electronic line control system can detect the present line velocity and parachute diameter to control the velocity of line being released. Team Daedalus thus has confidence that this continuous disreefing device can be used to further investigate the physics of continuously disreefed parachutes, taking a large step towards much needed innovation in the aerospace parachute industry.

Steps for Future Improvement

Component Improvements

Due to our limited time and budget, Team Daedalus had to make a number of compromises on material and components that would need to be improved to create a truly aerospace grade device. In future iterations, many changes, improvements, and redesigns would bring this device to be ready for application in military and aerospace parachute recovery systems. Some select improvements are listed below, though this list is not exhaustive.

Temperature Envelope

Budget restrictions and machining capabilities limited our material selection to aluminum and steel components. However, the vast majority of space grade metal components are made out of titanium. Titanium is roughly ten times more expensive than aluminum (aluminum costs approximately 2.50 /lb while titanium costs around \$25/lb) but provides a significantly better strength-to-weight ratio (aluminum has a specific strength of 115 kNm/kg vs. titanium with a specific strength of 260 kNm/kg). Titanium also has far superior thermal expansion ($23.1 \mu\text{m}/(\text{m}\cdot\text{K})$ for aluminum vs. $8.6 \mu\text{m}/(\text{m}\cdot\text{K})$ for titanium), which is essential in space applications as temperatures can fluctuate significantly throughout spaceflight. In the case of the parachute deployment envelope, there is not very significant temperature fluctuation through the deployment period. However, it is essential that the device not warp significantly due to the extreme cold environment of space prior to being activated during parachute recovery. Thus, titanium components would replace all aluminum components and some of the steel components where possible.

Currently, the Daedalus active braking system is designed to integrate a servo motor with a custom gearbox drivetrain to convert torque into linear actuation of the brake pads onto the brake disc. This custom gearbox was designed and manufactured because hydraulic braking systems would not function reliably within the temperature ranges specified by our stakeholders. However, in a final iteration, this entire active braking system would be integrally designed to utilize a low-powered motor and a more finely tuned gearing ratio to achieve the same characteristic braking force. Our current servo design would withstand the temperature requirements of spaceflight, as the internal gearing is constructed from titanium, but a more compact system could be integrally designed.

Passive System

One of the primary concerns voiced by our stakeholders when we shifted to designing an active system was the potential unreliability of an electronic system. Each electrical connection and component added brings more potential points of failure. Thus, it is essential that the passive braking system be designed to deliver a safe, though sub-optimal, parachute recovery. Given that we are concerned with controlling line velocity for a given tension, we knew that friction alone would not suffice for this passive system, as any small difference in force would blow up into a massive velocity very quickly. Thus, we knew viscous damping must be incorporated to ensure that a passive force proportional to the line velocity would be applied.

In our design, we utilized needle-roller bearings on our spool as they are designed to survive extremely high RPMs and large axial loads while inherently creating a fair amount of viscous friction, compared to traditional roller bearings. However, in our testing of the spool itself, we found that this viscous friction was nearly negligible compared to the forces expected in our system. We were unable to purchase viscous dampers that could survive anything near the loads we anticipated, but in future iterations, strong viscous dampers would be integrated on the spool to provide this passive assurance. An additional benefit of adding such viscous dampers would be a reduced load on the active system, allowing for its strength (and thus mass) to be reduced accordingly. This would stand to have a large impact on the overall robustness of our device and could potentially greatly reduce the very limiting design requirements of the active brake.

System Volume

In this iteration of the design, Daedalus has roughly one cubic foot of impact. The current parachute system for Orion is 7 cubic feet, meaning that the addition of three Daedalus disreefers would constitute adding 42% to the overall volume. While our stakeholders have stated that the reliability and load reduction benefits would outweigh this volume increase, they were still concerned about such a significant change. Thus, a primary redesign effort in future iterations would go to reducing the volume impact of Daedalus within the parachute system.

One potential solution suggested by our stakeholders is to place Daedalus on the capsule, feeding the reefing lines up to a central ring from which they would feed to the skirt of the parachute. However, this would require more than doubling the amount of rope that is contained in each Daedalus device, thus increasing the volume of the device, though that volume would no longer be carried in the parachute packaging.

Alternatively, the number of feed ropes could potentially be reduced from four to three, which would reduce the amount of line contained by 58 feet, constituting roughly a 10% reduction in length of line. This could reduce the size of the spool, though the change would not be very significant and would result in less symmetrical loading on the top plate of the device. Further

efforts could include reducing the footprint of the active brake and the electronic systems, which could allow the volume to be reduced.

Drop Testing

In our wrap up discussions with our stakeholders, we were graciously offered the opportunity to have SpaceX conduct a drop test of our device. This would require acquiring both test parachutes and a test mass, but SpaceX conducts frequent scale drop tests using helicopters and would be willing to put our device to the challenge. Should we move forward with this testing, we would use the opportunity both to validate our device and to gain previously unknown data on the loads in a reefing line during continuous disreefing. Since no empirical data exists about continuously disreefed parachutes, and much of the knowledge about reefing lines comes from empirical testing, our device could be used to take a huge step forward in this field.

For the testing, we would integrate line tension sensors in order to track the tension experienced in the suspension lines of the parachute (to determine if flatline parachute loading is achieved) and in the reefing line itself to characterize how this line behaves in tension during continuous disreefing. Our current system is designed to survive 600 lbf of line tension based on data from empirical tests of staged reefing systems, but this test could potentially show that the tension is far lower than this expected result, which could result in a significant reduction in design requirements of the system. Regardless of the result, collecting such data would be invaluable to all parachute engineers investigating the future of continuous disreefing.

6. BUDGET AND RESOURCES

Our budget consisted of \$2,400 given to us by the Mechanical Engineering and Applied Mechanics department at the University of Pennsylvania. The general breakdown of the distribution of these funds is displayed in Table 6.1 below and in further detail in Table 6.2.

Table 6.1 - Overall Budget

Prototyping	\$209.18
General Purpose Aluminum Stock	\$26.12
Kevlar Cord	\$65.00
Gear Box	\$560.70
Spool	\$60.45
Electronics--Active System	\$221.07
Enclosure	\$109.26
Outsourced Manufacturing	\$628.13
Testing Rigs	\$463.03
Miscellaneous Manufacturing	\$7.63
TOTAL	\$2350.57

Table 6.2 - Itemized Breakdown

CATEGORY	PRICE	QUANTITY	EXPENSE
<i>Prototyping</i>			
50" Nylon Parachute 16 Line	\$38.59	2	\$77.18
NFPA Long 6 Bar Rappel Rack	\$132.00	1	\$132.00
<i>General Purpose Aluminum Stock</i>			
6061 AL, ½" Thick x 3" Wide 2 ft Long	\$26.12	1	\$26.12
<i>Kevlar Cord</i>			

3/16" 12 Strand KevTec 12 -- 100 ft	\$65.00	1	\$65.00
Gear Box			
Metal Miter Gear - 20 Degree Pressure Angle, 16 Pitch, 16 Teeth	\$23.94	3	\$71.82
Metal Gear - 14-1/2 Degree Pressure Angle, Set Screw & Keyway, 20	\$49.58	4	\$198.32
Metal Gear - 14-1/2 Degree Pressure Angle, 32 Pitch, 40 Teeth	\$34.04	1	\$34.04
Metal Gear - 14-1/2 Degree Pressure Angle, 32 Pitch, 16 Teeth	\$16.58	1	\$16.58
High-Strength Steel Threaded Rod, 1/4"-20 Thread Size, 1 Foot Long	\$6.88	1	\$6.88
High-Friction Brake and Clutch Lining, 7-1/2" Long x 7-1/2" Wide x 1/2" Thick	\$45.26	1	\$45.26
Linear Motion Shaft for Harsh Environments, Ceramic-Coated 6061	\$13.43	1	\$13.43
External Retaining Ring, 15-7 PH Stainless Steel, for 3/8" OD	\$8.36	1	\$8.36
316 Stainless Steel Round Shim, 0.01" Thick, 3/8" ID	\$3.98	2	\$3.98
Metal Gear - 14-1/2 Degree Pressure Angle, Press-Fit Mount, 20	\$22.40	2	\$44.80
High-Friction Brake and Clutch Lining, 7-1/2" Long x 7-1/2" Wide x 1/4" Thick	\$34.68	1	\$34.68
Lightweight Keyed Rotary Shaft, 2024 Aluminum, 3/8" Diameter, 12" Long	\$18.38	1	\$18.38
1095 Spring Steel Machine Key Stock, 3/32" x 3/32", 12" Long	\$1.72	1	\$1.72
Ultra-Low-Friction Oil-Embedded Sleeve Bearing with PTFE, for 3/8" Shaft	\$0.70	8	\$5.60
Metal Miter Gear - 20 Degree Pressure Angle, 16 Pitch, 16 Teeth	\$47.90	1	\$47.90
Compression Spring, Zinc-Plated, Closed Ends, 0.25" Long, 0.24" OD	\$4.97	1	\$4.97

<i>Spool</i>			
6061 Aluminum, 8" Diameter, 1/2" Long	\$36.68	1	\$36.68
6061 Aluminum, 3/4" Diameter, 12" Long	\$4.65	1	\$4.65
Steel Needle-Roller Bearing, Open, for 3/4" Shaft Diameter, 1" OD, 1/2" Wide	\$5.95	2	\$11.90
External Retaining Ring, 15-7 PH Stainless Steel, for 3/4" OD	\$7.22	1	\$7.22
<i>Electronics--Active System</i>			
ABS Strip, 11" Wide, 3/64" Thick, 5 ft Length, Opaque Black	\$29.60	1	\$29.60
Mega Torque HV Coreless Titanium Gear Servo; RB-Hit-91	\$161.99	1	\$161.99
Encoders En Rop 11mm,3Ch 5000CPR, Strg Lds	\$29.48	1	\$29.48
<i>Enclosure</i>			
6061 Aluminum, 9" Diameter, 1/2"	\$42.56	2	\$85.12
6061 Aluminum Sheet, 1/8" Thick, 6" x 6"	\$9.60	1	\$9.60
316 Stainless Steel Flat Head Screw, 82 Countersink, 1/4"-20 Thread, 1/2" Long	\$3.79	3	\$11.37
6061 Aluminum, 3/4" Diameter 1/2 ft	\$3.17	1	\$3.17
<i>Outsourced Manufacturing</i>			
Gearbox Housing -- Protolabs	\$468.13	1	\$468.13
Top Shell -- Frank B. Claytons	\$160.00	1	\$160.00
<i>Testing Rigs</i>			

T-Slotted Framing, End-Feed Fastener, for 1" High Single Rail	\$2.30	4	\$9.20
Pulley for Wire Rope-for Lifting, Mounted, for 3/16" Diameter, 2" OD	\$7.38	8	\$59.04
T-Slotted Framing, Diagonal Brace for 1" High Single Rail, 6" Long	\$15.67	8	\$125.36
T-Slotted Framing, Single Rail, Silver, 1" High x 1" Wide, Solid, 3ft	\$11.53	4	\$46.12
T-Slotted Framing, Single Rail, Silver, 1" High x 1" Wide, Solid, 1 ft	\$6.49	8	\$51.92
T-Slotted Framing, Corner Brace for 1" High Single Rail, 1" Long	\$5.51	16	\$88.16
6061 Aluminum, 3/16" Thick x 2" Wide, 2 ft	\$6.58	1	\$6.58
T-Slotted Framing, Dual End-Feed Fastener, for 1" High Single Rail	\$4.29	2	\$8.58
T-Slotted Framing, Single Rail, Silver, 1" High x 1" Wide, Solid, 3ft	\$10.57	6	\$63.42
6061 Aluminum, 3/16" Thick x 3" Wide, 3 ft	\$4.65	1	\$4.65
<i>Miscellaneous Manufacturing</i>			
General Purpose Left-Hand Tap for Through-Hole Threading 1/4"-20 Thread	\$6.38	1	\$6.38
Left-Hand to Right-Hand Male Thread Adapter, 1/4"-20 Thread	\$1.25	1	\$1.25
TOTAL			\$2350.57

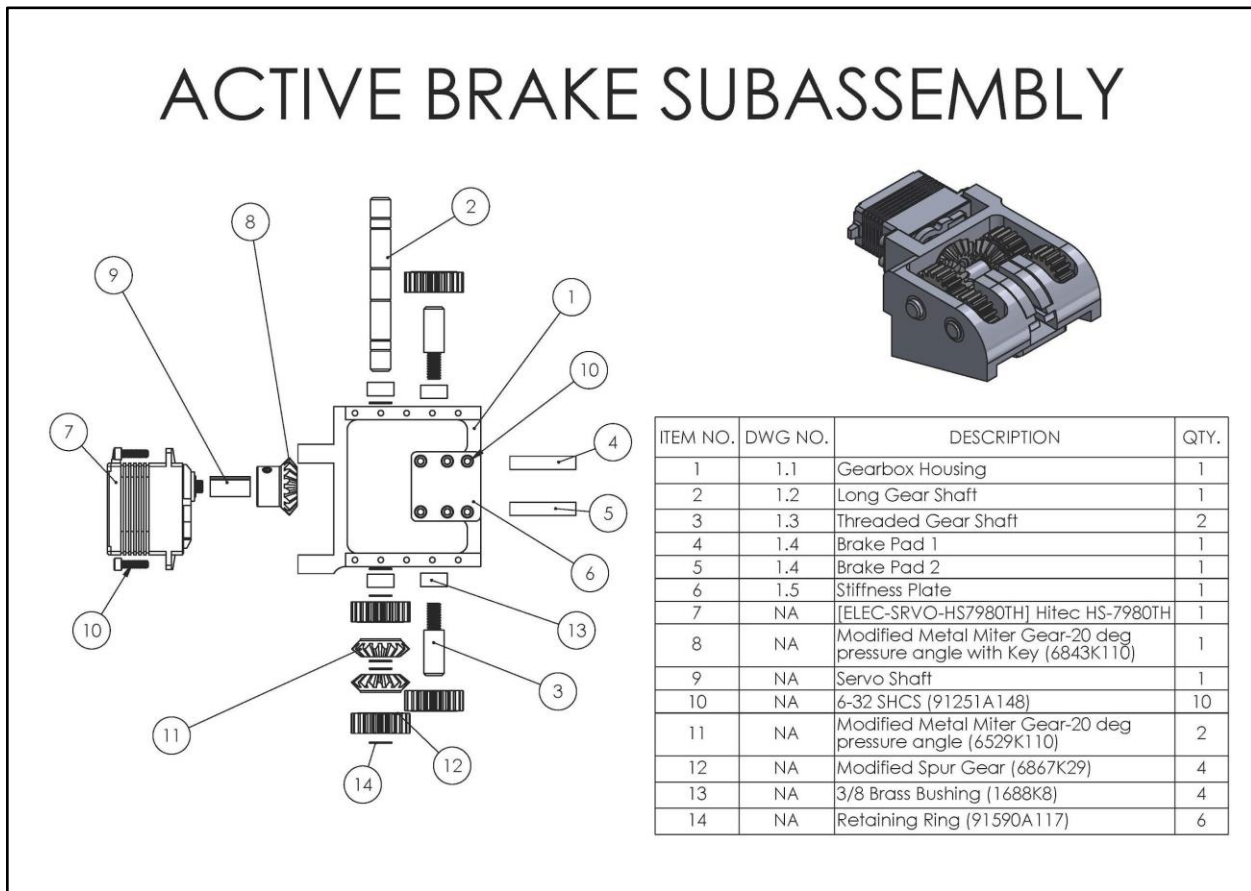
REFERENCES

- [1] T. W. Knacke, Parachute Recovery Systems: Design Manual, Santa Barbara, CA: Para Publishing, 1992.
- [2] E. Rafacz, 'Gemini Spacecraft Systems', 2015. [online]. Available: <http://geminiguide.com/Systems/landing.html>. [Accessed: 6- May- 2018].
- [3] 'How Parachutes are made', [2016]. [Online]. Available: <http://www.madehow.com/Volume-5/Parachute.html>. [Accessed: 6- May- 2018].
- [4] FPSPA, 'Parachute Equipment,' [2004]. [Online]. Available: <http://rumell.net/fpspa4/fpspa/class2.htm> [Accessed: 6- May- 2018].
- [5] *Unit and Direct Support Maintenance Manual For Parachute, Cargo Type: 35-foot diameter Ribbon Extraction Parachute*, TM-10-1670-294-23P, Department of the Army, The Pentagon, Arlington, VA. Accessed on: May, 06, 2018. [Online]. Available: http://parachutemanuals.tpub.com/TM-10-1670-294-23P/css/TM-10-1670-294-23P_138.htm
- [6] T. W. Knacke, "Reefing of Parachutes, Drag Area Ratios vs Reefing Ratios," Aeronautical Systems Division, Wright-Patterson Air Force Base, OH: July, 1976.
- [7] O. Shade, "Parachute with Control Means," U.S. Patent 2 754 074, December 29, 1953.
- [8] E. Puskas, "High Drag Slider Reefing System for Parachutes," U.S. Patent 5 005 785, December 31, 1985.
- [9] B. Case and P. Kadlec, "Parachute Reefing System," U.S. Patent 4 863 119, September 9, 1988.
- [10] S. L. Snyder, "Pilot Chute Controlled Inflation System for Parachutes," U.S. Patent 3 540 684, February 11, 1969.
- [11] J. S. Sutton, "Air Reefing System," U.S. Patent 3 945 592, April 26, 1974.
- [12] C. V. Eckstrom et. al., "Effects of 1980 Technology on Weight of a Recovery System for a One Million Pound Booster," NASA/Langley Research Center, Hampton, VA: April, 1975.
- [13] *Structural Design and Test Factors of Safety For Spaceflight Hardware: Measurement System Identification: Metric/SI (English)*, NASA NASA-STD-5001A, 2008.
- [14] *Structural Design Requirements and Factors of Safety for Spaceflight Hardware For Human Spaceflight*, NASA, JSC 65828, 2011.
- [15] *Soldered Electrical Connections*, NASA, NASA-STD-8739.3, 1997.
- [16] *NASA Software Engineering Requirements*, NASA, NPR 7150.2B, 2014.

APPENDIX

Engineering Drawings

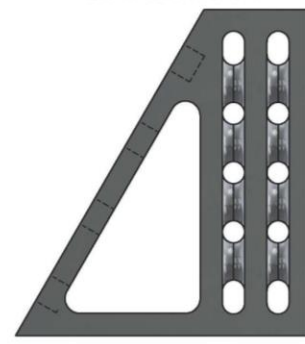
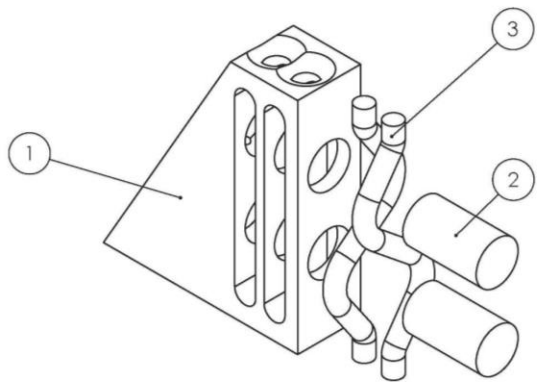
Subassembly Drawings



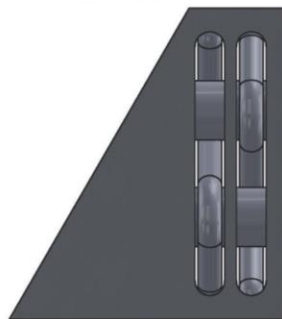
DWG 1.0: Active Brake Assembly Exploded View and BOM

CAPSTAN SUBASSEMBLY

CAPSTAN V1



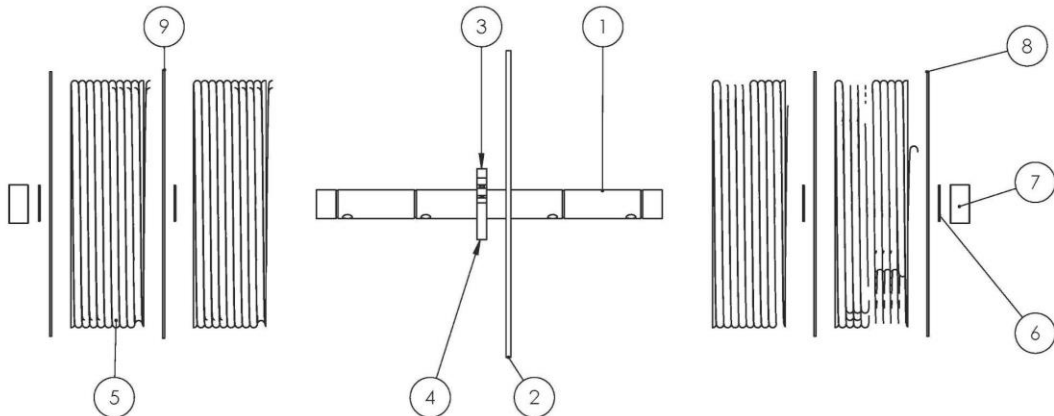
CAPSTAN V2



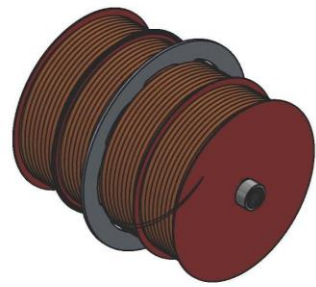
ITEM NO.	DWG NO.	DESCRIPTION	QTY.
1	2.2	Capstan Mounting Block	1
2	2.3	Capstan Rod	2
3	NA	Dummy Rope	2

DWG 2.0: Capstan Assembly Exploded View and BOM

SPINDLE SUBASSEMBLY

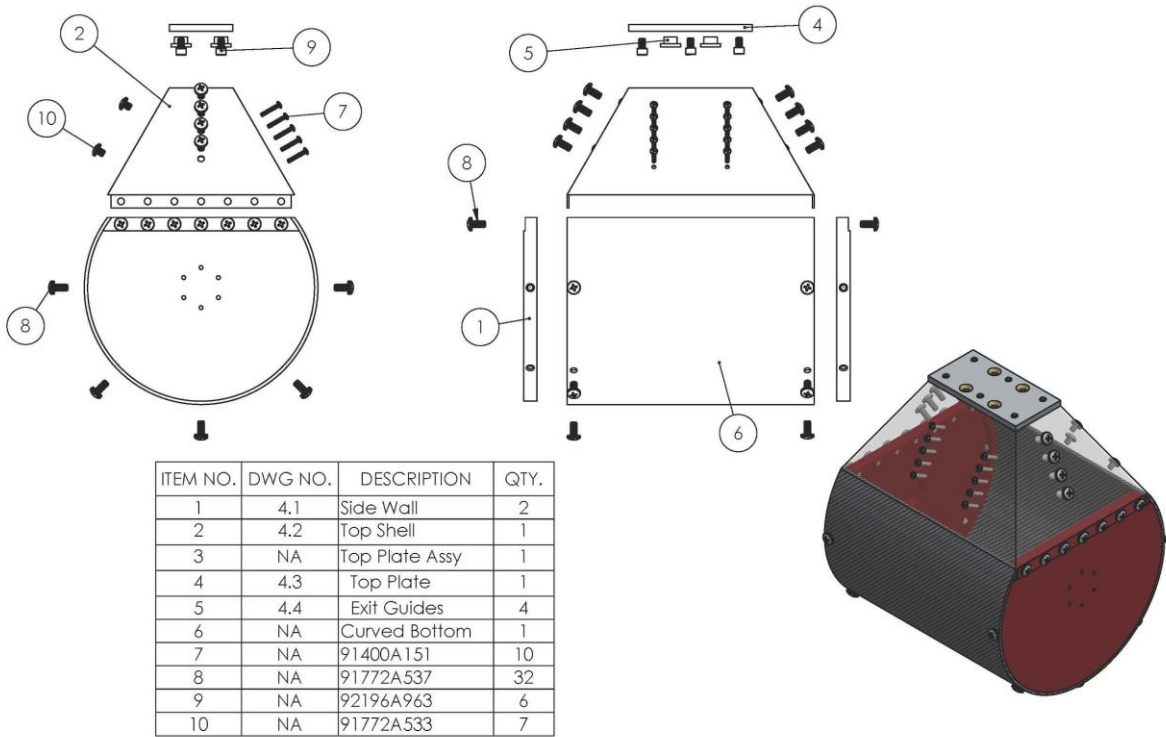


ITEM NO.	DWG NO.	DESCRIPTION	QTY.
1	3.1	Spindle Shaft	1
2	3.2	Brake Disk	1
3	3.3	Disc Mounting A	1
4	3.4	Disc Mounting B	1
5	NA	Rope Spool	4
6	NA	Retaining Ring (91590A128_grv)	4
7	NA	Needle Roller Bearing (5905K26)	2
8	NA	Spacer	3
9	NA	Spacer - Encoder Mod	1



DWG 3.0: Spindle Assembly Exploded View and BOM

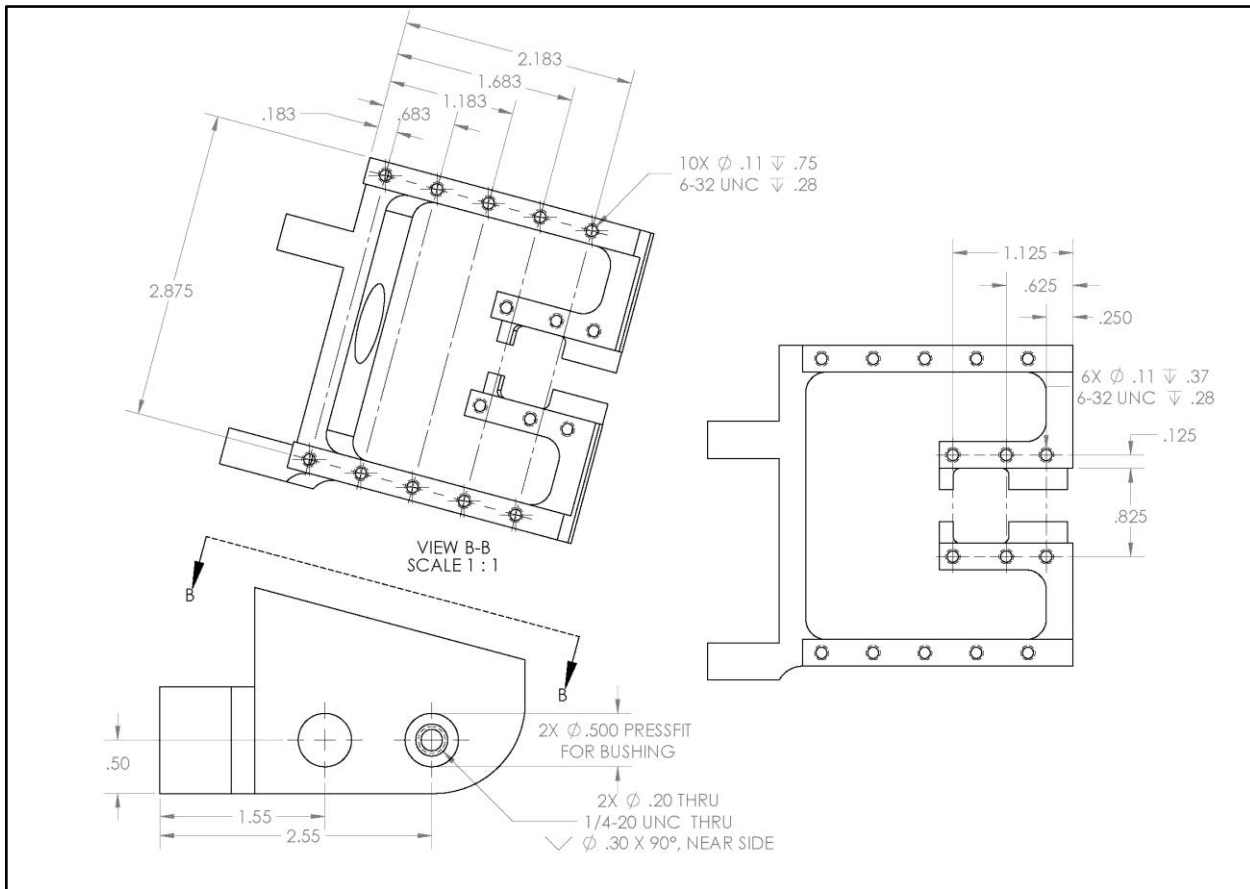
ENCLOSURE SUBASSEMBLY



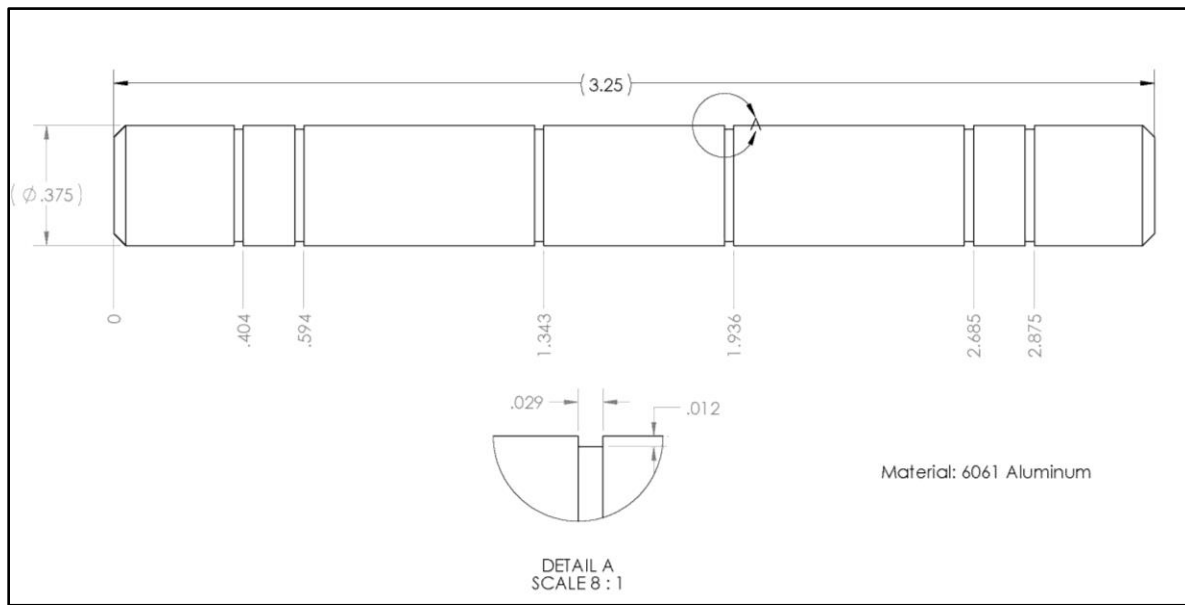
DWG 4.0: Enclosure Assembly Exploded View and BOM

Part Machine Drawings

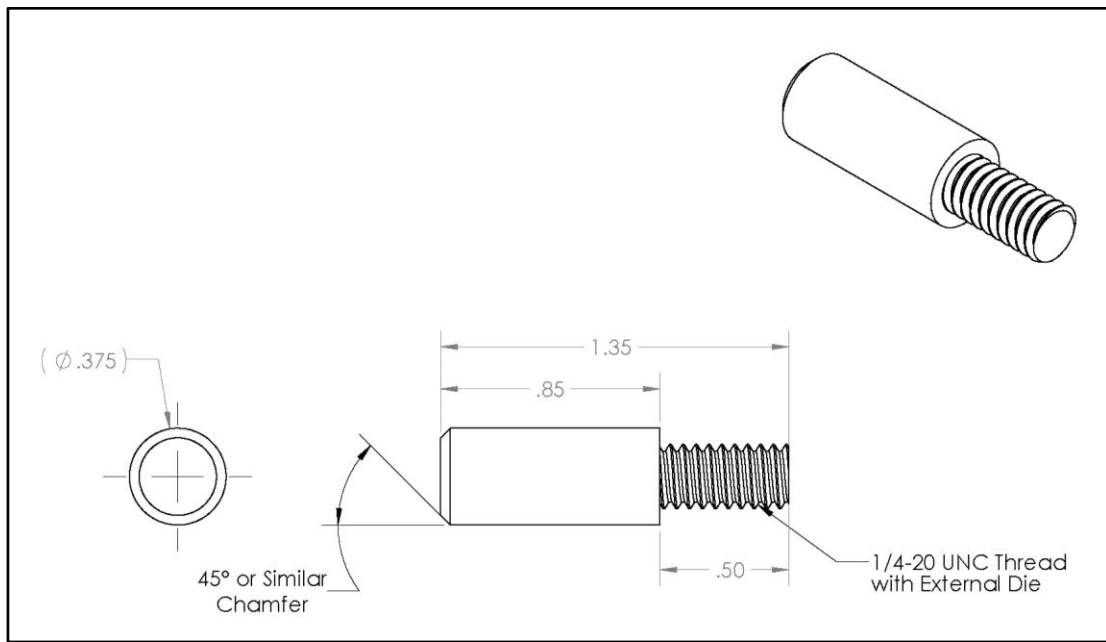
Active Brake Subassembly



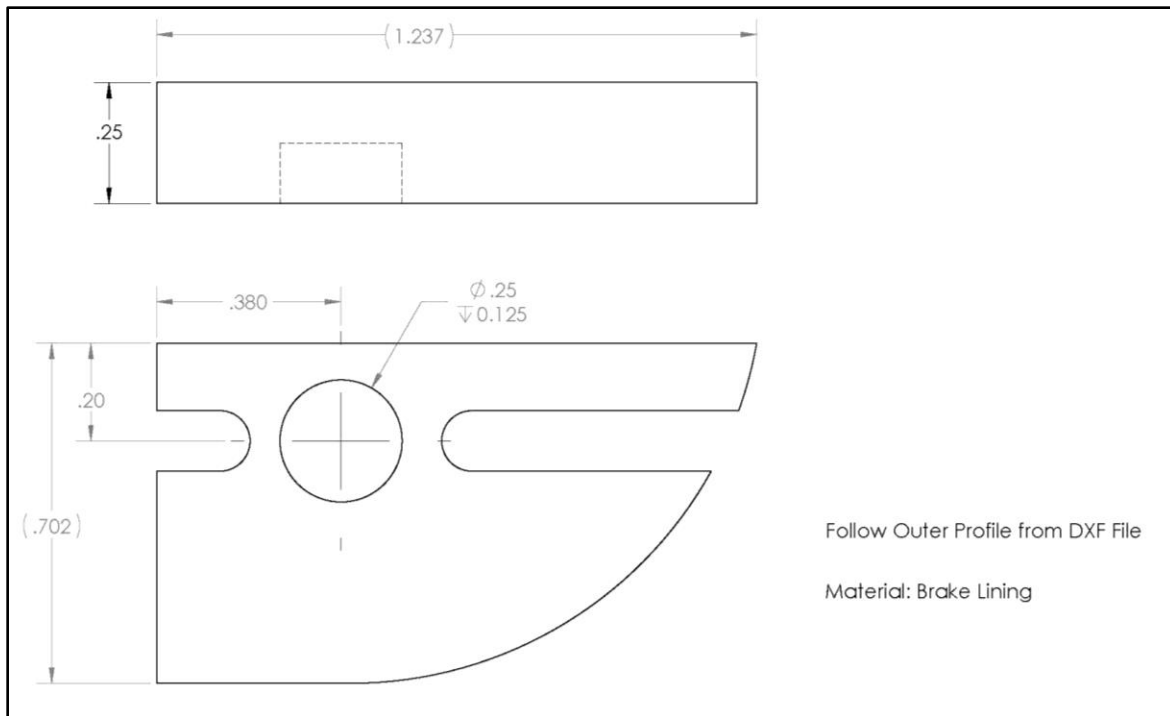
DWG 1.1: Brake Housing Post-Processing Machine Drawing



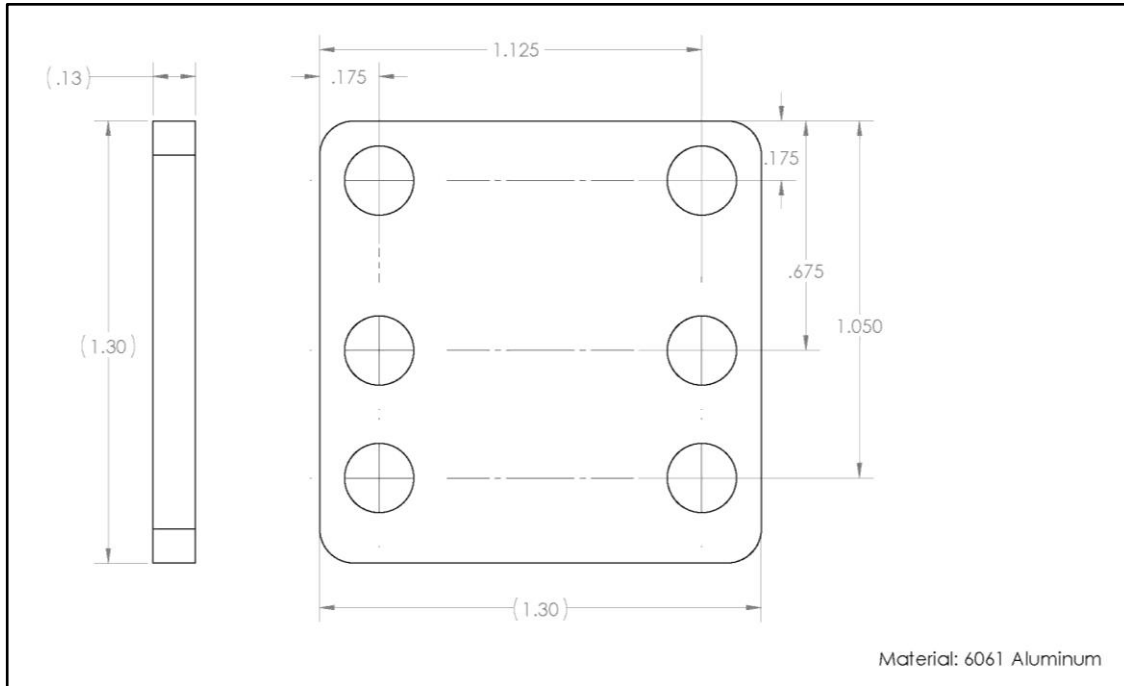
DWG 1.2: Long Gear Shaft Machine Drawing



DWG 1.3: Long Gear Shaft Machine Drawing

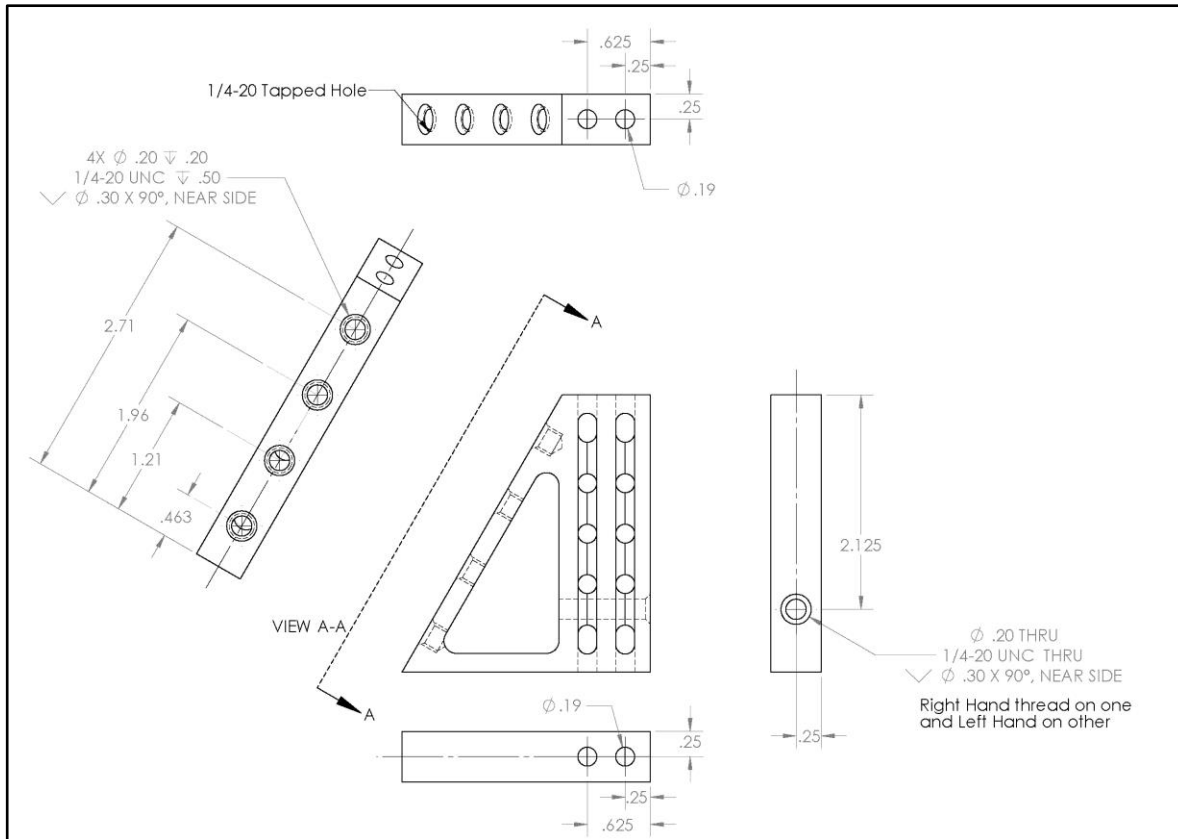


DWG 1.4: Brake Pad Machine Drawing

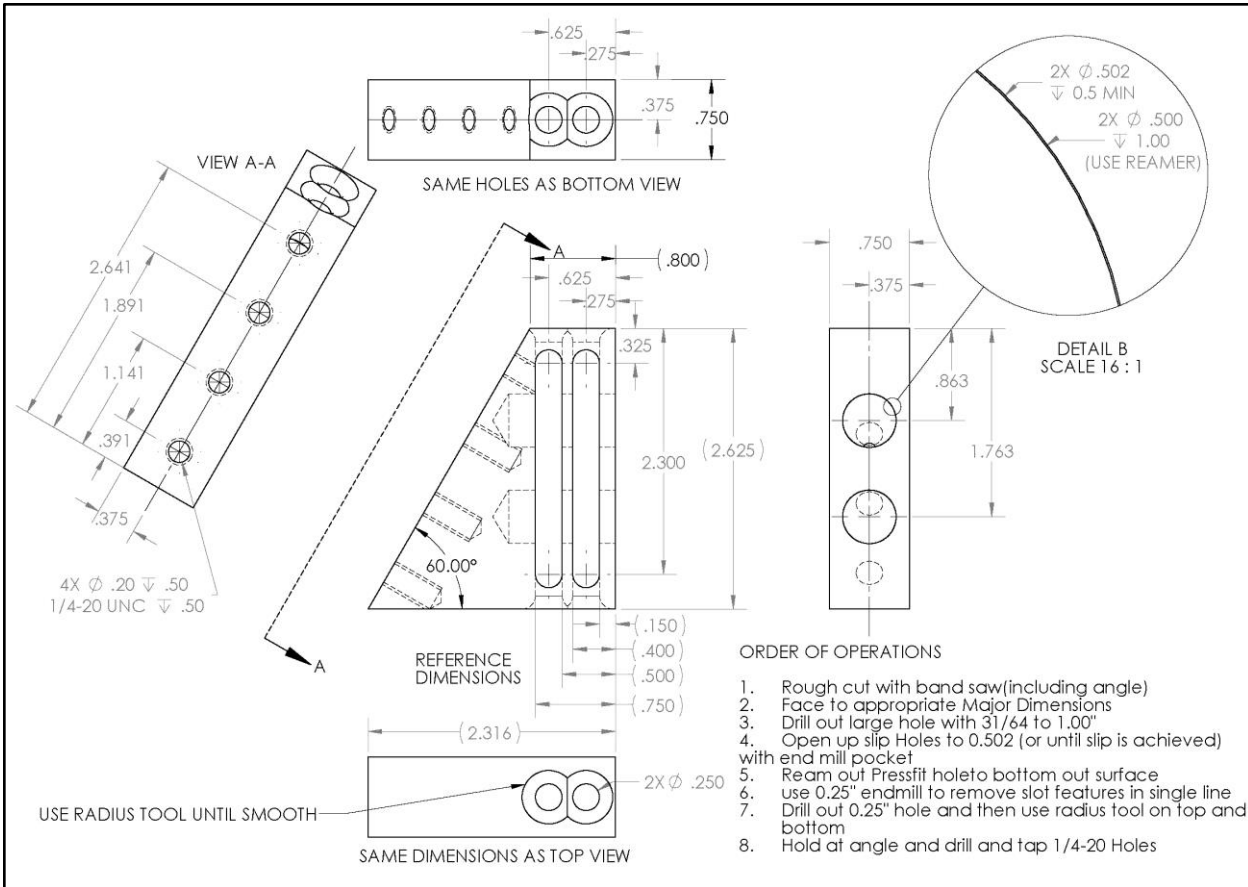


DWG 1.5: Stiffness Plate Machine Drawing

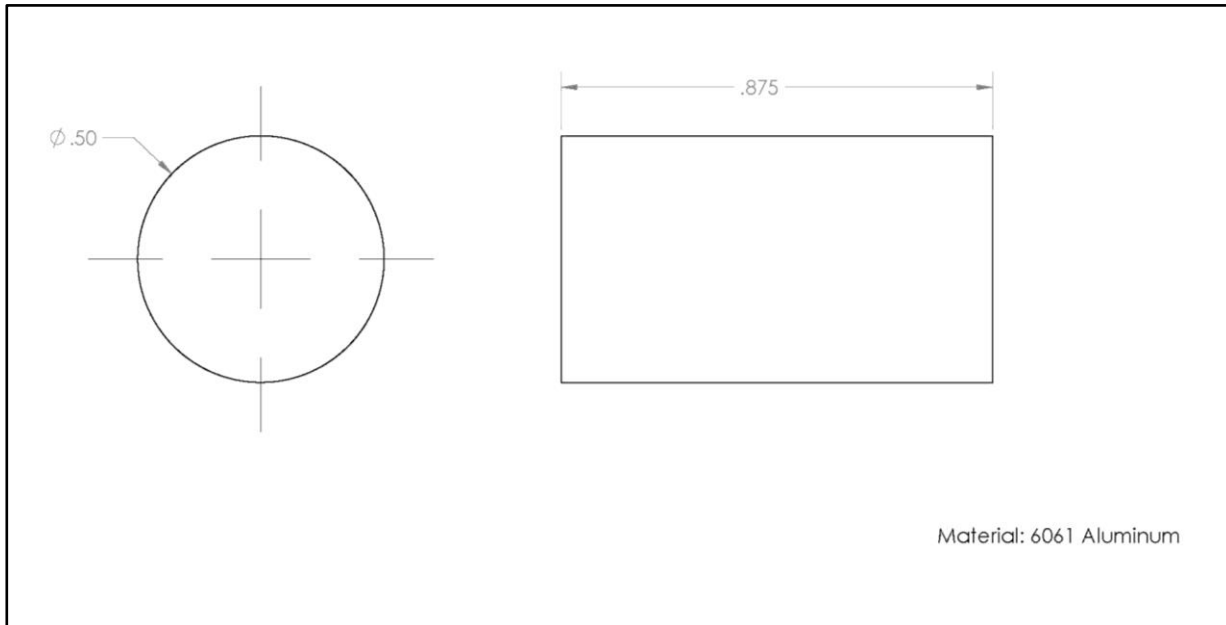
Passive Subassembly



DWG 2.1: Capstan v1 Post Processing Machine Drawing

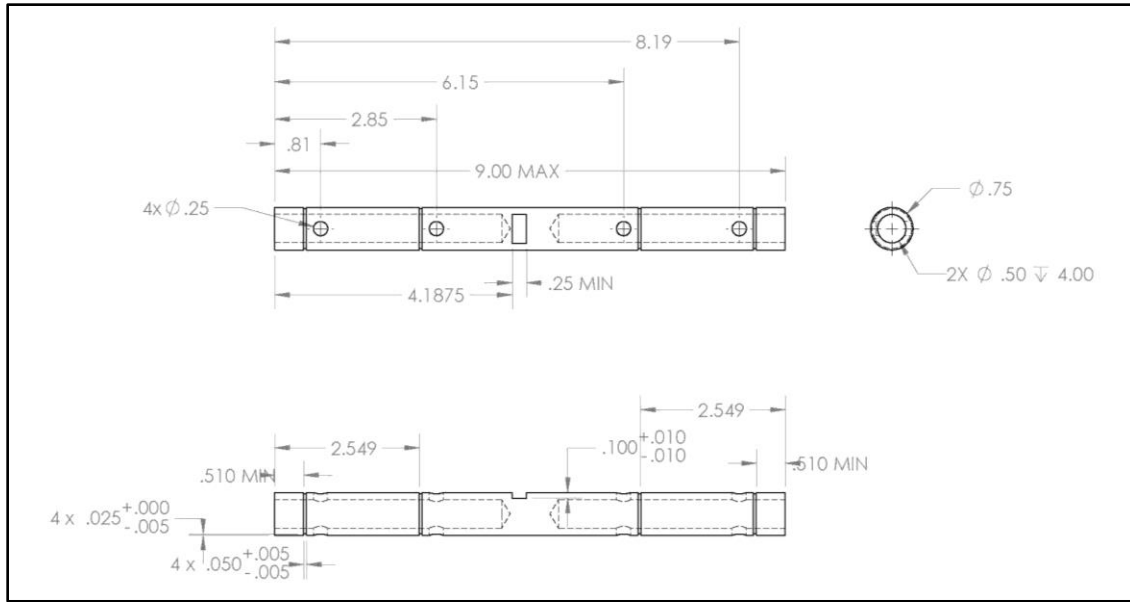


DWG 2.2: Capstan v2 Mounting Block Machine Drawing

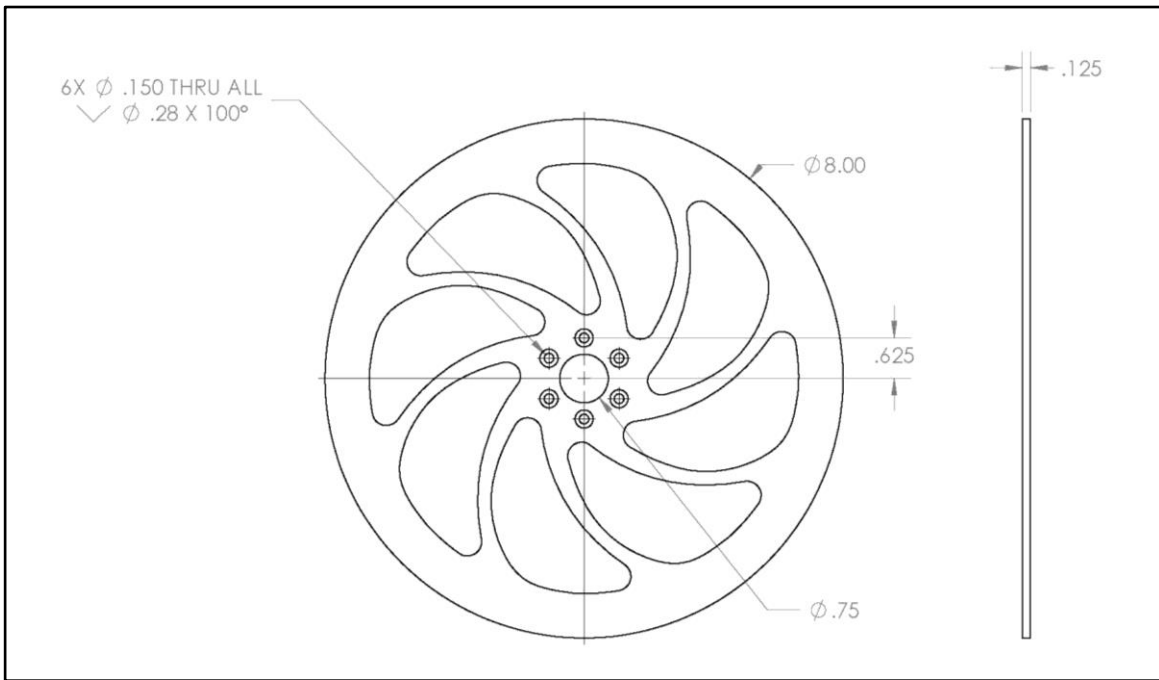


DWG 2.3: Capstan Rod Machine Drawing

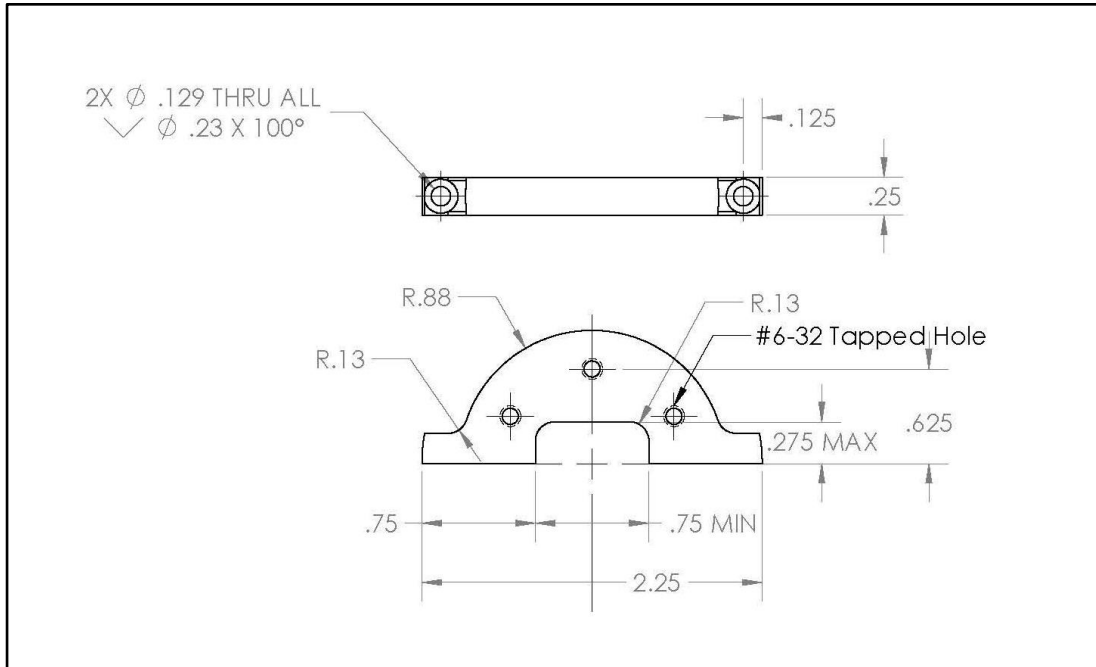
Spindle Subassembly



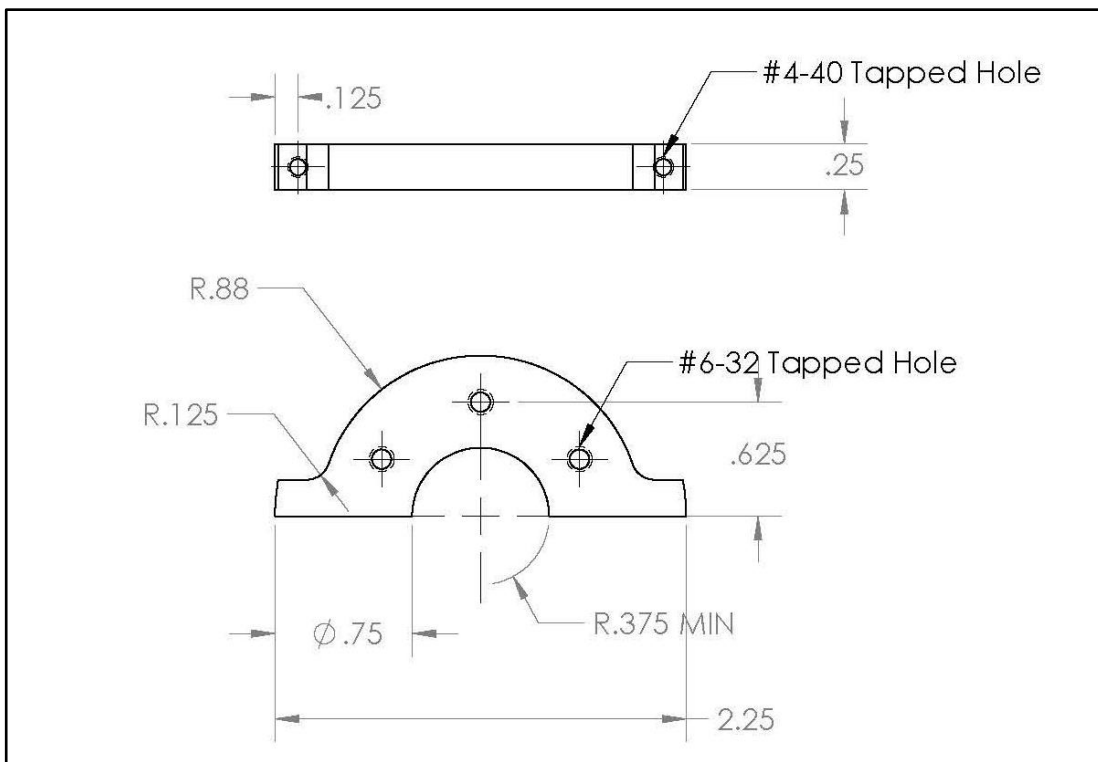
DWG 3.1: Spindle Shaft Machine Drawing



DWG 3.2: Brake Disc Machine Drawing

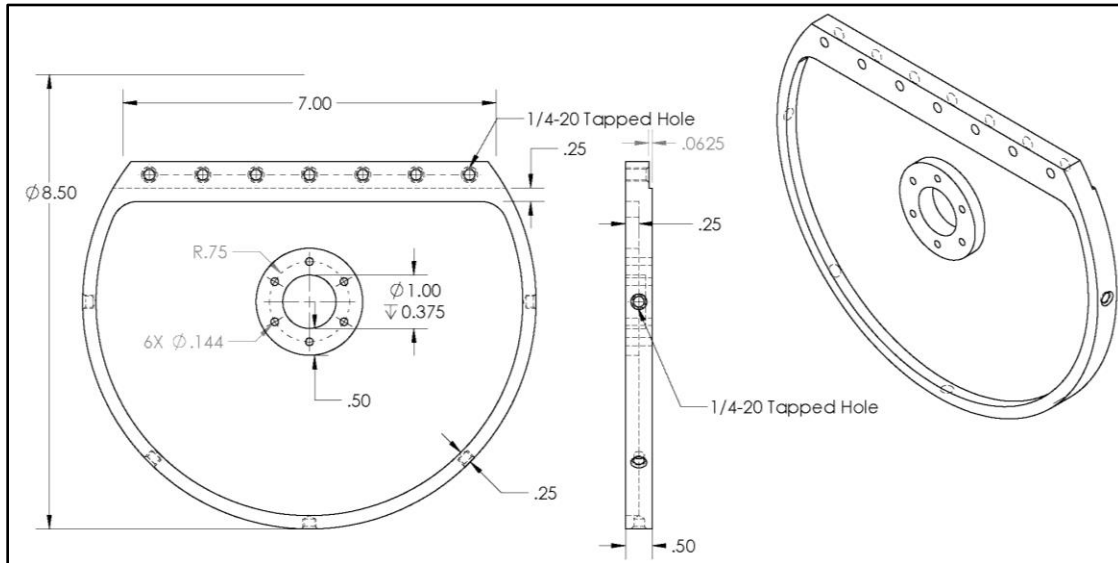


DWG 3.3: Disc Mounting A Machine Drawing

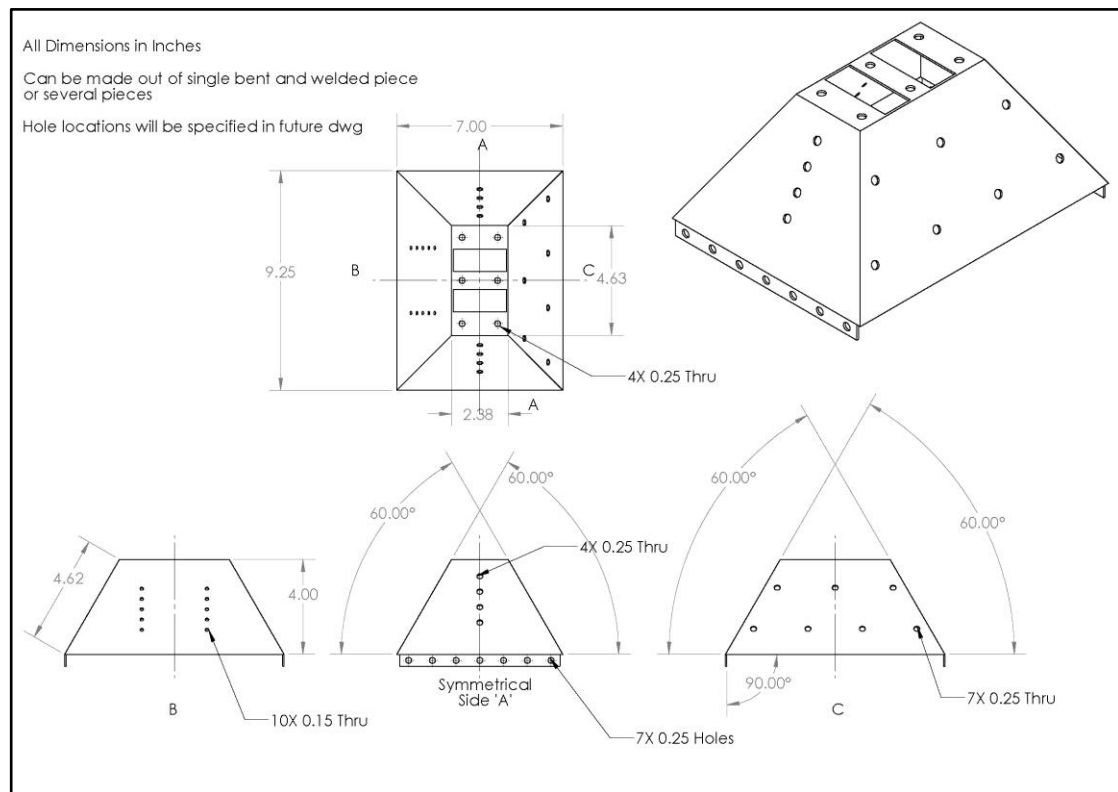


DWG 3.4: Disc Mounting B Machine Drawing

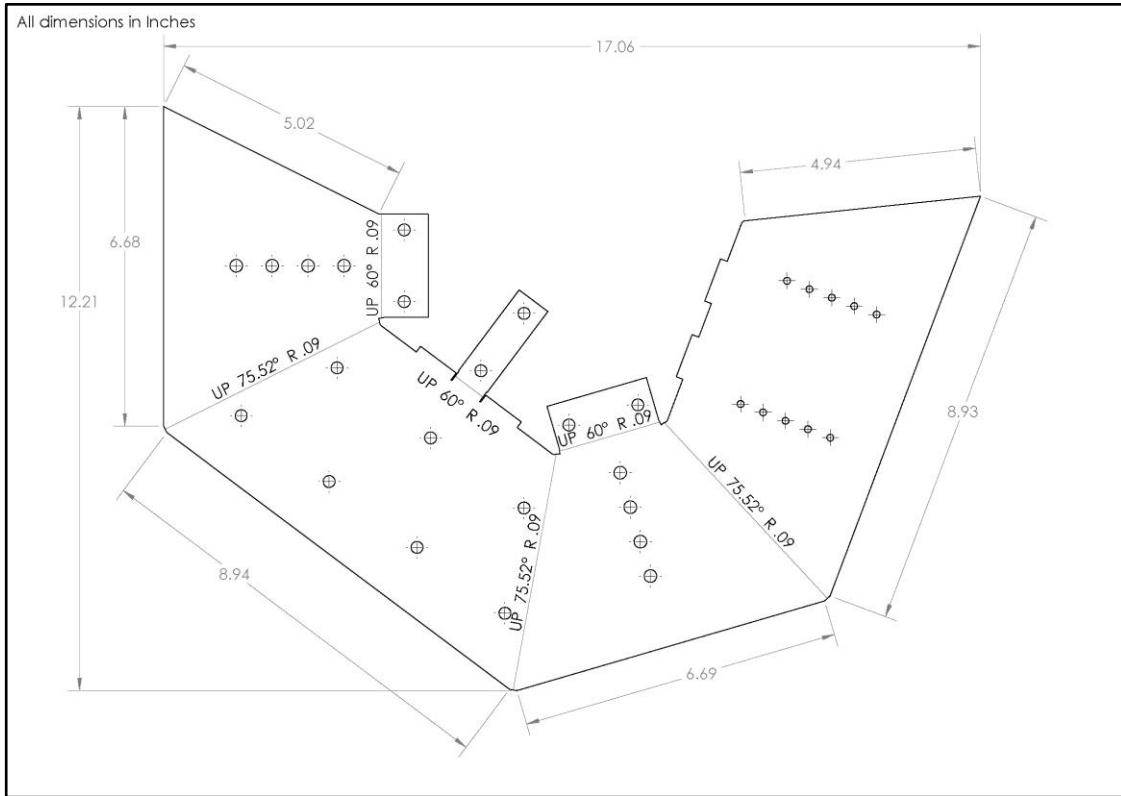
Enclosure Subassembly



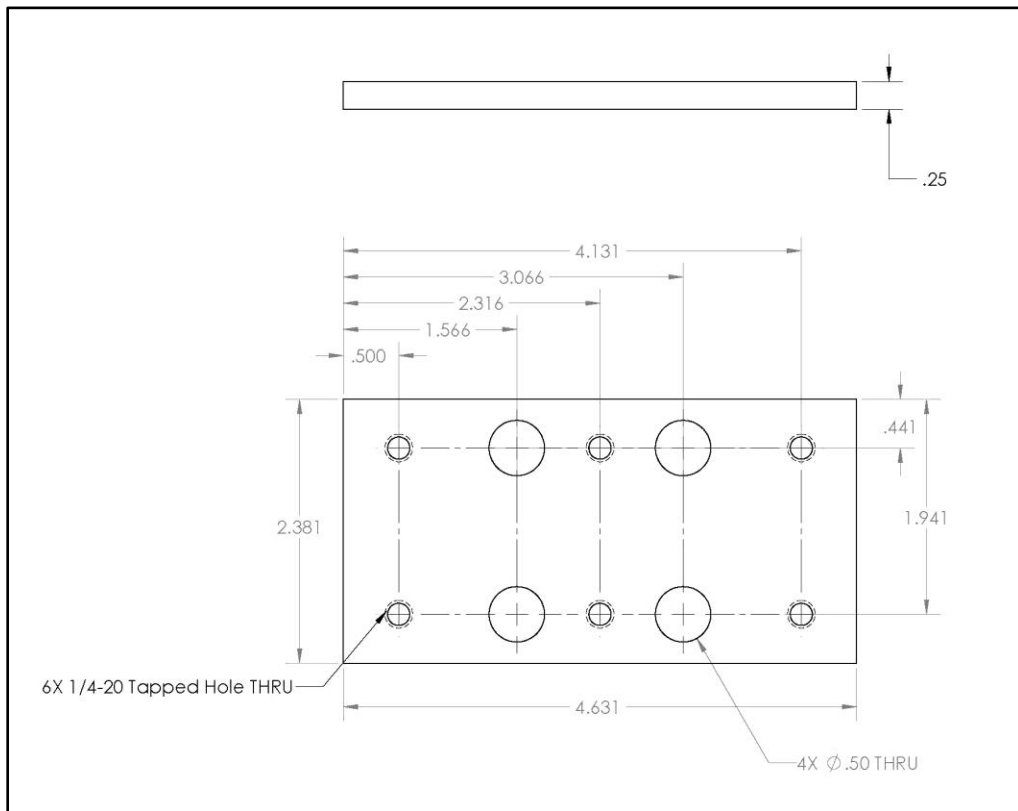
DWG 4.1: Sidewall Machine Drawing



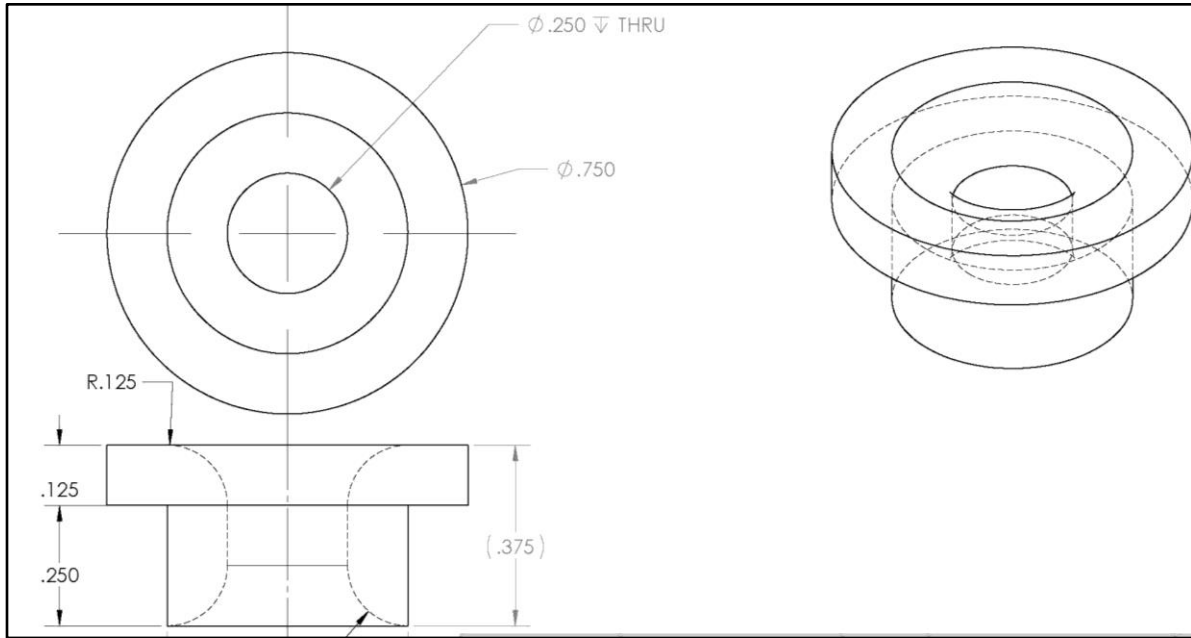
DWG 4.2a: Top Shell Machine Drawing



DWG 4.2b: Top Shell Flattened Pattern Machine Drawing



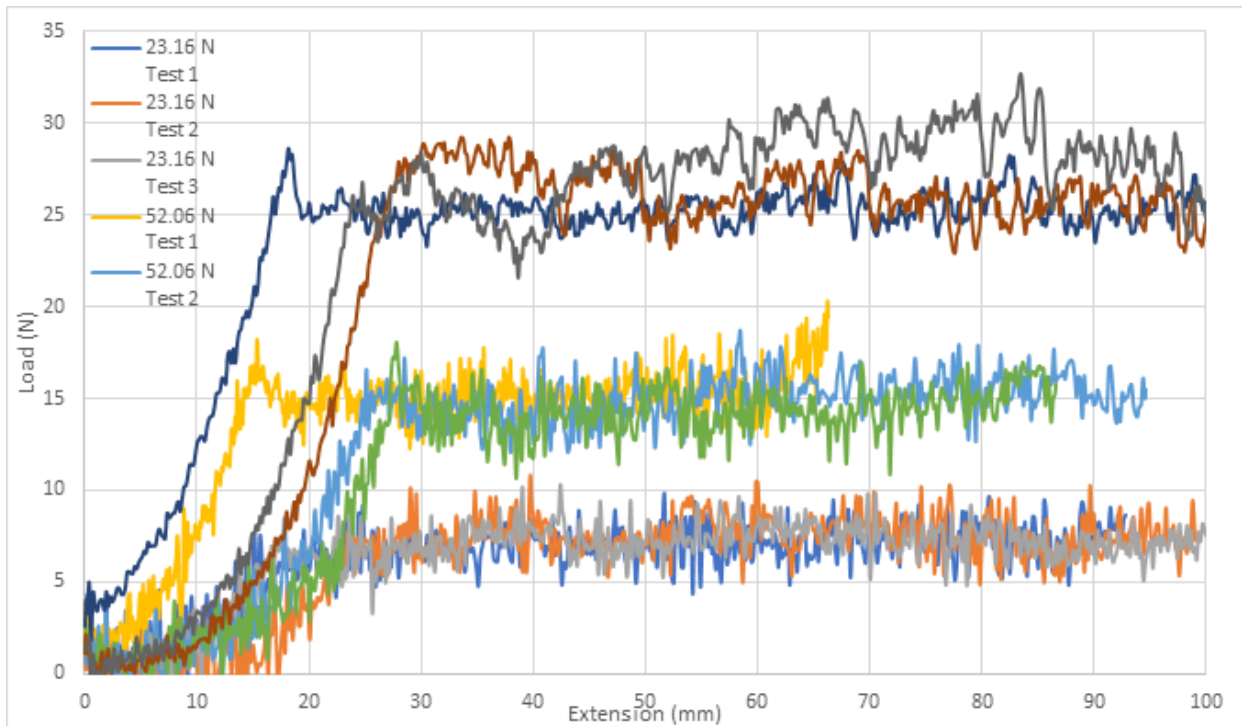
DWG 4.3: Top Plate Machine Drawing



DWG 4.4: Rope Exit Guide Machine Drawing

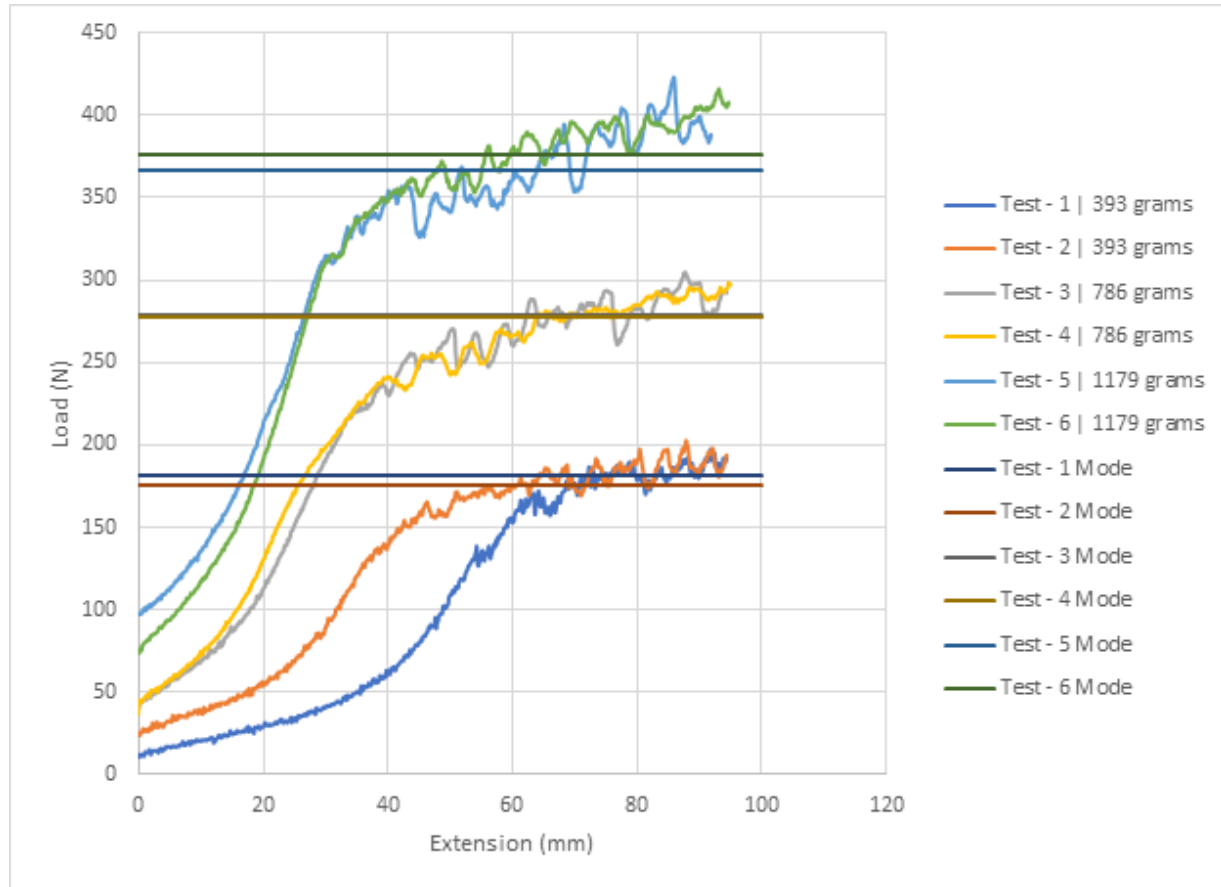
Testing Data

Coefficient of Friction - Brake Pad/Aluminium



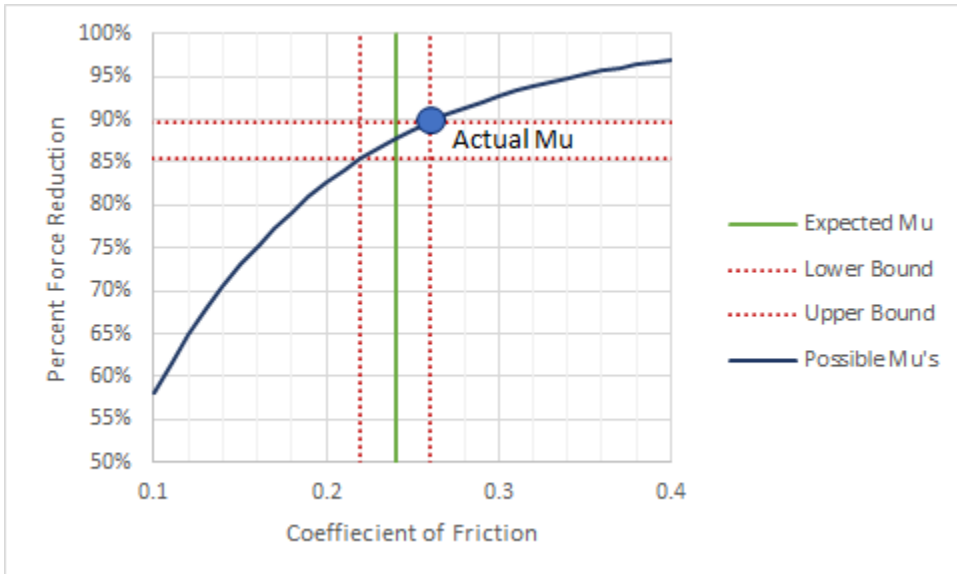
	Averages between Trials			
Normal Force	23.16 N	52.06 N	94.9 N	
Applied Load	7.198 N	14.783 N	26.454 N	Average Coefficient
Coefficient of Friction	0.310	0.284	0.279	0.291

Coefficient of Friction - Kevlar/Aluminium

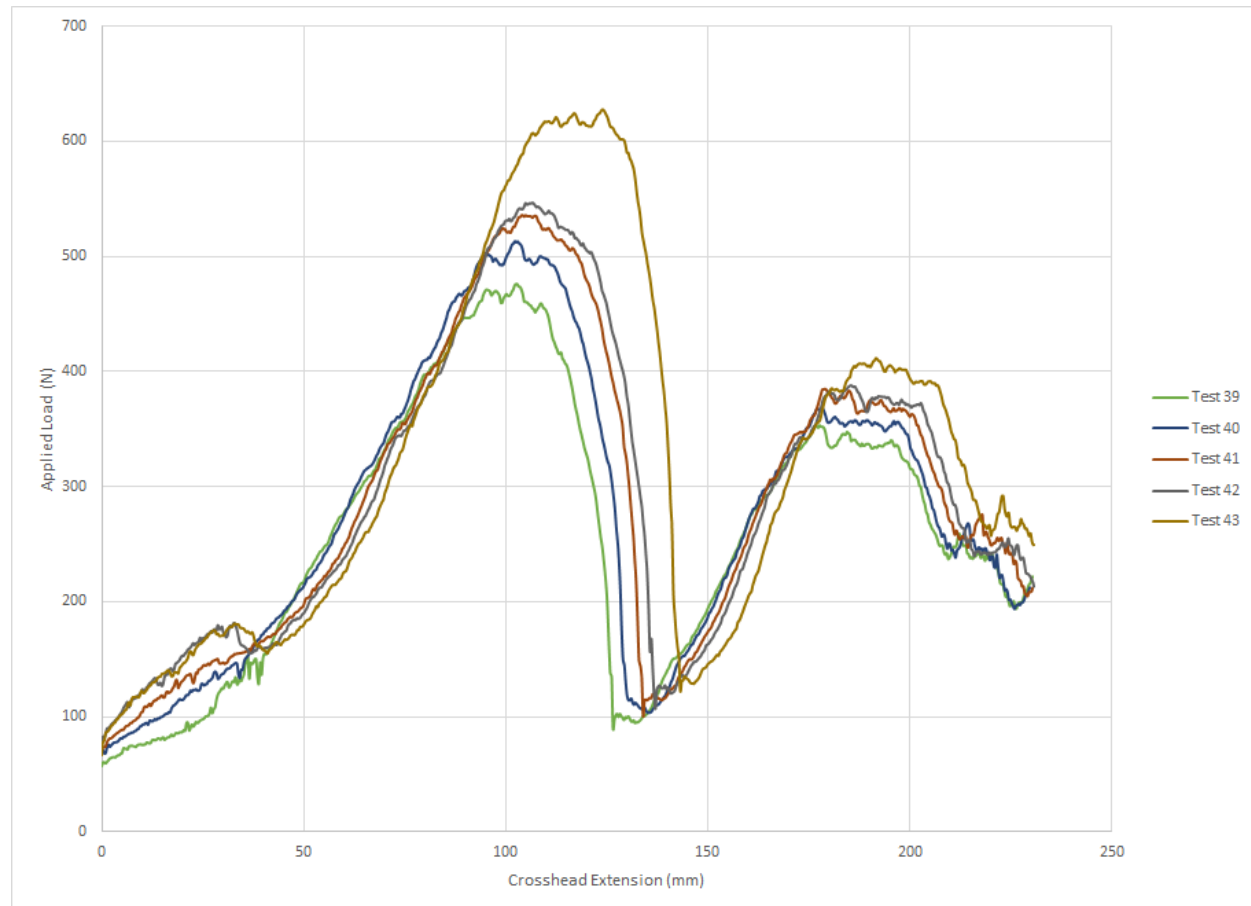


	Test 1	Test 2	Test 3	
<i>Mass per Line</i>	393 grams	786 grams	1179 grams	
<i>Total Mass</i>	1572 grams	3144 grams	4716 grams	
<i>Weight</i>	15.42 N	30.84 N	46.26 N	
<i>Load</i>	178.55 N	278.27 N	370.87 N	Averages
<i>Percent Difference</i>	91.36%	88.92%	87.53%	89.27%
<i>Exponential Term</i>	2.449	2.200	2.081	2.243
<i>Reduction Factor</i>	11.578	9.022	8.016	9.539

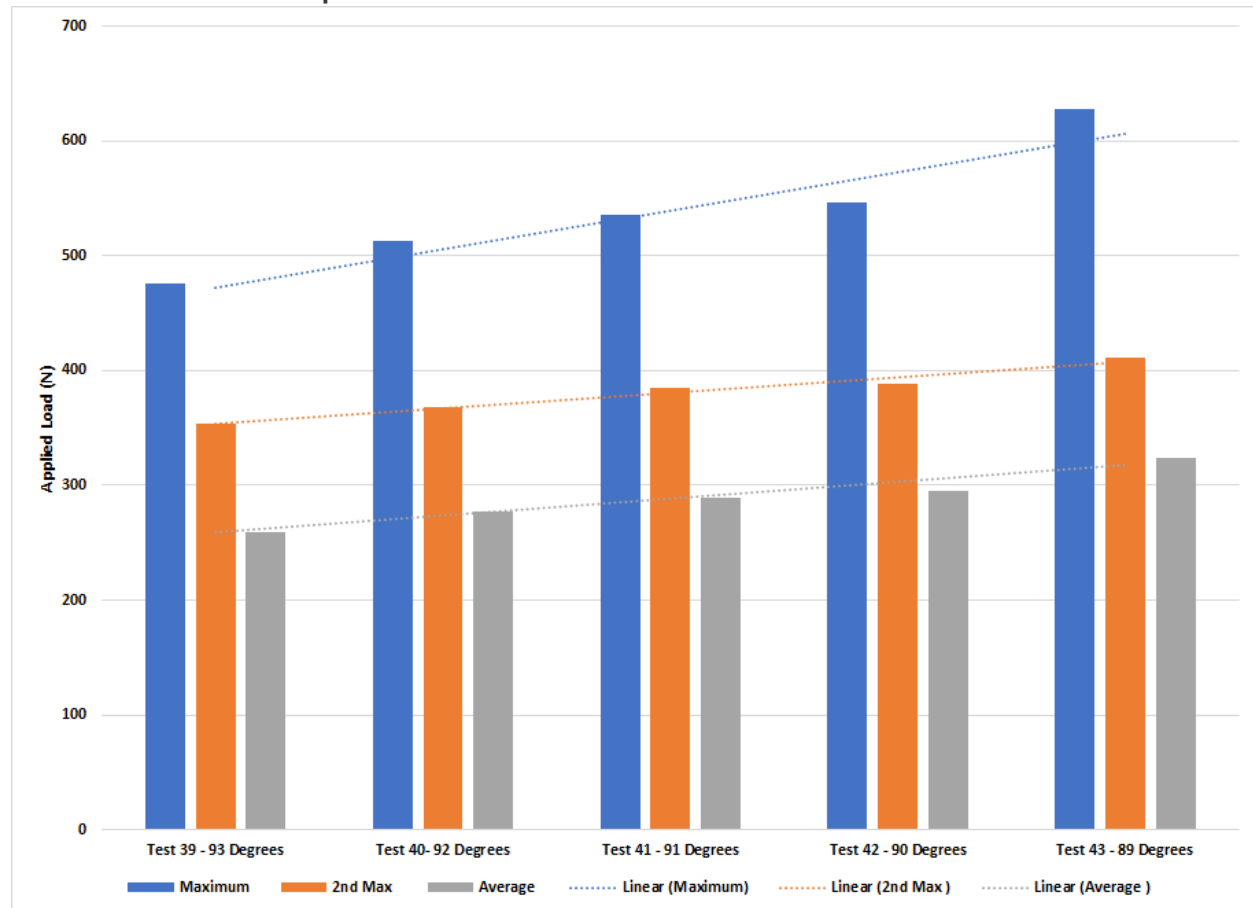
Capstan Characterization



Servo Characterization



Servo Characterization plotted



Arduino Code

EncoderServoConnection

```
/*
  Daedalus Control Code

*/

#include <Servo.h>
#include <PID_v1.h>

// Decide which test to run
bool v_test = true;          // [-]
bool m_test = false;         // [-]

bool log_data = true;        // Turn flag to true to export data
///////////////////////////////



const int encoderPin = 11;      // Encoder Pin 13

int encoderPinLast = LOW;     // Storing state of last Encoder position
int n = LOW;                  // Saving last state
int counter = 0;

Servo S;
const int servoPin = 9;
const int servoEngaged = 85; // first engagement angle (needs to be determined empirically)
const int servoOpen = 95;
double servoOutput = constrain(servoOutput, 70, 120);

const int tickRes = 1;

// CONSTANTS

const int ticks = 50;          // [-] ticks on encoder per revolution
const double radius = 0.050;    // [m] Spool Radius
const double pi = 3.1415;

const double v_fast = 0.5;     // [m/s] Set Fast Speed
const double v_slow = 0.2;      // [m/s] Set Slow Speed

const double v_goal = 0.05;     // [m/s] Nominal Speed

// VARIABLES

int encoderPos = 0;           // Encoder Position (ticks)
int ticksN = 0;

double rev = 0.0;              // [-] Number of full spool revolutions
double theta = 0.0;             // [rad] Spool Angle
double thetalast = 0.0;         // [rad] Last Spool Angle
double omega = 0.0;             // [rad/s] Spool Angular Speed
double omegalast = 0.0;         // [rad/s] Last Spool Angular Speed
double alpha = 0.0;             // [rad/s^2] Spool angular Acceleration

double x = 0.0;                // [m] Length of line let out
double xlast = 0.0;             // [m] Last Length of line
double v = 0.0;                 // [m/s] Velocity of line let out
double vlast = 0.0;             // [m/s] Last Velocity of line let out
```

```

double a = 0.0;           // [m/s^2] Angular Velocity
double v_err = 0.0;        // [m/s] Command Velocity error
double v_errlast = 0.0;    // Last Velocity error
double v_err_dot = 0.0;    // Derivative of error
double v_err_int = 0.0;    // Integral of error

long t = 0;                // [ms] Current time
long tlast = 0;             // [ms] Last time
long tdelta = 0;            // [ms] Delta time
long tcheck = 0;
long abstime = 0;           // [ms] Absolute Time

//Specify initial tuning parameters
double Kp = 2, Ki = 0, Kd = 0;

// Generally, you should use "unsigned long" for variables that hold time
// The value will quickly become too large for an int to store
unsigned long previousMillis = 0;          // will store last time LED was updated

// constants won't change:
const long interval = 10;                  // interval at which to blink (milliseconds)

void setup() {
  Serial.begin(57600);

  Serial.println("initializing...");
  pinMode(encoderPin, INPUT);    // Setting Encoder Input Pin

  pinMode(servoPin, OUTPUT);    // Setting Servo pin to output
  S.attach(servoPin);          // Attaching the Servo to the Pin

  Serial.println("running...");

}

void loop() {

  if (counter == 0) {
    double servoOutput = 80;          // Servo PID Command variable
    S.write(servoOutput);            // Resetting the servo to 180 degrees (open)
    Serial.println("servo_closed ... ");
    counter = 1;
    Serial.println("DELAYING");
    delay(10000);
    Serial.println("DELAY OVER");
  }
  // Updating encoder position
  n = digitalRead(encoderPin);
  if ((encoderPinLast == LOW) && (n == HIGH)) {
    encoderPos++;
    ticksN++;
  }

  if (ticksN == tickRes) {

    Update_State(); // Update state of all variables
    Print_State(); // Serial Print current state

    servoOutput = (int) (Kp * v_err + Kd * v_err_dot + Ki * v_err_int); // PID Controller
    S.write(servoEngaged + servoOutput);
  }
}

```

```

    }

//Testing Function

if (t <= 17 && x >= 0.001) {
    if (v >= .3) {
        servoOutput --;

        S.write(servoOutput);
        Serial.print("BRAKING, S = ");
        Serial.println(servoOutput);
        delay(100);
    }
    else {
        servoOutput++;
        S.write(servoOutput);
        Serial.print("OPENING, S = ");
        Serial.println(servoOutput);
    }
}
if (t>17){
    if (v>=.1){
        servoOutput --;

        S.write(servoOutput);
        Serial.print("BRAKING, S = ");
        Serial.println(servoOutput);
        delay(100);
    }
    else {
        servoOutput++;
        S.write(servoOutput);
        Serial.print("OPENING, S = ");
        Serial.println(servoOutput);
    }
}

}
ticksN = 0;
}

if (millis() - t > 500 && servoOutput < 100) {
    Serial.print("STOPPED, S = ");
    servoOutput++;
    S.write(servoOutput);
    Serial.println(servoOutput);
    delay(200);
}

encoderPinLast = n;
}

```

UpdateState

```

void Update_State() {

    t = millis(); // Get current Time in ms
    tdelta = t - tlast; // Find delta T since last

    rev = (double) encoderPos / ticks; // Updating Rev count
    theta = 2 * pi * rev; // Updating theta based off Rev count
    omega = (theta - thetalast) / (0.001 * tdelta); // Updating Omega
    alpha = (omega - omegalast) / (0.001 * tdelta); // Updating Alpha
}

```

```

x = theta * radius;           // Updating line let out
v = (x - xlast) / (0.001 * tdelta); // Updating line velocity
a = (v - vlast) / (0.001 * tdelta); // Updating line Acceleration

v_err = v - v_goal;          // Updating the velocity error
v_err_dot = (v_err - v_errlast)/(0.001*tdelta); // Derivative of error
v_err_int = v_err_int + v_err; // integral of velocity error

//Setting to previous for comparisons

tlast = t;

thetalast = theta;
omegalast = omega;

xlast = x;
vlast = v;

v_errlast = v_err;

}

PrintState

void Print_State() {

    if (log_data) {

        Serial.print("#$|LOGTEST|[");

        Serial.print(String(t));
        Serial.print(", ");
        Serial.print(String(v, 3));
        Serial.println("]#");

    }
    else {

        Serial.print("X: ");
        Serial.print(x);
        Serial.print(", V: ");
        Serial.print(v);
        Serial.print(", T:");
        Serial.println(t);

    }
}

```